Project No. 09-780

Thermal Properties of LiCl-KCl Molten Salt for Nuclear Waste Separation

Fuel Cycle R&D

Dr. Kumar Sridharan
University of Wisconsin, Madison

In collaboration with:
Idaho National Laboratory

Michael Simpson, Technical POC
James Bresee, Federal POC

NEUP Nuclear Energy University Programs
U.S. Department of Energy

Thermal Properties of LiCl-KCl Molten Salt for Nuclear Waste Separation

Project Investigators: Dr. Kumar Sridharan, Dr. Todd Allen, Dr. Mark Anderson (University of Wisconsin) and Dr. Mike Simpson (Idaho National Laboratory)

Post-Doctoral Research Associates: Dr. Luke Olson
Graduate Students: Mr. Mehran Mohammadian and Mr. Sean Martin
Undergraduate Students: Mr. Jacob Sager and Mr. Aidan Boyle

University of Wisconsin-Madison

NEUP Final Report

Project Contact: Dr. Kumar Sridharan
kumar@engr.wisc.edu

Date: November 30th, 2012

Table of Contents

1. Introductory Narrative

Molten LiCl-KCl eutectic salt is used in pyrochemical processing as a medium for separating of radioactive nuclides in spent nuclear fuel (SNF). The process was developed for processing spent metallic fuel from the sodium-cooled fast reactors like the EBR-II, and its application is being expanded to process spent oxide fuels that have been converted to metal via an oxide reduction process. In the pyrochemical process, the spent fuel is anodically dissolved in the molten LiCl-KCl salt, and pure uranium metal is recovered at a steel cathode. The recent development of the liquid cadmium cathode (LCC) technology at the Idaho and Argonne National Laboratories allows for the separation of uranium, plutonium, and minor actinides (MA) which are collected in a liquid cadmium cathode. The minor actinides which have very long half-lives are recovered with plutonium and can be transmuted in fresh fuels, rather than be sent to repository sites. The process is also applied to recover minor actinides from high level waste generated in PUREX reprocessing facilities. Therefore, pyrochemical processing using molten LiCl-KCl salt is critically important to the United States' Advanced Fuel Cycle Initiative (AFCI), the Global Nuclear Energy Partnership (GNEP), and non-proliferation.

The proposed research addresses both practical and fundamental scientific issues that are of direct relevance to the some of the operational challenges of the molten LiCl-KCl salt pyrochemical process, while providing avenues for improvements in the process. Since the primary challenges stem from the continually changing composition of the molten salt bath during the process, studies will be performed by systematically varying the concentrations of rare earth surrogate elements, lanthanum, cerium, neodymium, and dysprosium that will be added to the molten LiCl-KCl salt. A limited number of focused experiments will be performed by the dissolution of depleted uranium. All experiments will be performed at 500˚C, which is the commonly used temperature for pyrochemical processing.

The density of the molten salts will be measured using an instrument specifically designed for this purpose and the melting points will be determined with a differential scanning calorimeter. Knowledge of these properties is essential for salt mass accounting and taking the necessary steps to prevent melt freezing. Cyclic voltammetry studies will be used to determine the redox potentials of the rare earth cations, as well as their diffusion coefficients and activities in the molten LiCl-KCl salt. Anodic stripping voltammetry will be performed to determine the concentration of the rare earth elements and their solubility, and for developing the scientific basis for an on-line diagnostic system for *in situ* monitoring of the concentration of the cation species (rare earths in this case). Solubility and activity of the cation species are critically important for the prediction of useful life time of the salt and its disposal.

The proposed project will consist of the following tasks:

(i) Measurements of densities and melting points of the LiCl-KCl salt as a function of concentration of rare earth surrogate elements, La, Ce, Nd, and Pr.

(ii) Cyclic voltammetry for the determination of redox potentials, reaction mechanisms, diffusion coefficients, and activities of rare earth elements in molten LiCl-KCl salt.

(iii) Anodic stripping voltammetry to determine the concentration and solubility of rare earth elements in molten LiCl-KCl salt and for the development of an on-line diagnostic system for *in situ* monitoring of rare earth element concentrations.

(iv) Electrochemistry of molten LiCl-KCl salt with dissolved depleted uranium.

This 3-year research project is being performed at the University of Wisconsin, in collaboration with Idaho National Laboratory (INL), with students, scientific staff, and faculty members participating in the program. INL is playing an advisory role in the project.

2. Motivation

With electricity demand rising and the need for nuclear power increasing, more feasible methods of disposing and reusing the approximately 60,000 metric tons of nuclear waste must be considered [1]. Pyroprocessing, or pyrometallurgical processing, is a high-temperature electrochemical process used at INL to reprocess spent fast reactor fuel [2, 3]. The process starts when chopped fuel in a basket is dissolved in a molten 500^{o}C LiCl-KCl eutectic salt and is then anodically dissolved into the salt leaving behind only noble metal fission products and cladding hulls [2, 3]. With the rest of the fuel ionically dissolved in the salt, a reductive potential is applied between a solid steel cathode (SSC) and the anodic fuel basket to cause a desired element, in this case, uranium, to electrochemically plate onto the surface of the solid steel cathode [2, 3]. The electrodeposit of uranium metal can then be pressed and sintered into new fuel or reconverted to UF_6 for enrichment to new fuel [2].

Use of this pyrochemical process initiated considerable interest as a future commercial reprocessing technique, but it still has many challenges. Since the process at present is best suited for metallic fuels and the vast majority of the spent fuel in the United States is an oxide, the process requires either an extra electrochemical step for oxide reduction or a front-end voloxidation process to be compatible with the United States' 104 oxide-fueled light water reactors [2]. Other research lies in selecting and modeling an appropriate waste form for both the metallic fuel, disposal of the fission product-laden salt, and reprocessing off-gas treatment [2, 4-5].

Although the process as used at INL has historically extracted pure U metal, it is possible, with use of a liquid cadmium cathode (LCC), to electrochemically plate both U and Pu at the same time thus reducing proliferation concerns [3]. Actinides may be separately extracted to reduce the overall long-term decay heat and radioactivity of the spent fuel [3]. These actinides could conceivably be used in a burner reactor with a fast flux to extract further energy or provide process heat for chemical or industrial processes.

The remainder of spent fuel left in the electrorefiner after all the above steps is composed of fission products and lanthanides. Lanthanides are a particularly important group of elements because they behave chemically and electrochemically similar to uranium, plutonium, and the other actinides so they may be co-deposited with the previously mentioned elements and act as a neutron poison in the reprocessed fuel which is undesirable [3]. In addition, as more fuel is reprocessed, the concentration of these lanthanides (and fission products) increases and causes the thermodynamic properties of the salt to change.

The present research attempts to answer these fundamental research questions on how the thermodynamic properties, such as melting point, lanthanide solubility, and density, which are important from operational, safety, and proliferation perspectives change with the addition of rare earth elements. In addition, the electrochemical behavior of four lanthanides (Ln= La, Ce, Nd, and Dy) are being investigated with the intent of providing a scientific basis for the development of an *in situ* electrochemical probe using either anodic stripping voltammetry (ASV) or cyclic voltammetry (CV) as the basis to determine the concentration of these elements specifically within INL's electrorefiner system. Other effects of lanthanide concentration on diffusion coefficient and activity coefficient are currently being studied to enhance the fundamental knowledge of how lanthanides behave specifically in LiCl-KCl eutectic at 500^{o}C.

3. Experimental Setup

The materials and equipment used for this research are described in detail in the following section. An electrochemical cell constructed at UW-Madison was used for the electrochemical studies investigating rare earth chlorides in LiCl-KCl and uranium chloride experiments were conducted at the facilities located in the Center for Advanced Energy Studies at Idaho National Laboratory. A molten salt density measurement apparatus was also built in-house at the University of Wisconsin-Madison and a differential scanning calorimeter was utilized to perform the melting point analysis.

3.1 Molten Salt Electrochemistry

3.1.1 LiCl-KCl Eutectic Salt

As stated in the previous section, pyroprocessing uses a molten LiCl-KCl eutectic salt as a solvent. The LiCl-KCl used for this research was obtained from Idaho National Laboratory and it has purity greater than 99%. The eutectic composition of the salt, 44.3 mol% KCl – 55.7 mol% LiCl, was used due to its relatively low melting point of approximately 353°C (See Figure 1). A summary of various other salt properties are shown in Table I. The salt is a hard white solid. The salt was received in large monolith form from Idaho National Laboratory. The salt was then crushed into smaller chunks for convenience and placed in Kerr mason jars. The mason jars were then placed in large desiccators which were evacuated and backfilled to a half atmosphere with industrial grade argon (see Figure 2). Storage of the salt in desiccators with an inert atmosphere is necessary due to the fact that LiCl-KCl is very hygroscopic and will readily form hydrates upon contact with water in the atmosphere. The salt was transferred from the desiccators to a glove box for electrochemistry experiments as needed.

Table I. Physical properties of LiCl-KCl eutectic salt [6].

Parameter	Value or Equation
$T_{melt,LiCl}$	610˚C
$T_{melt,KCl}$	770˚C
$T_{melt,LiCl\text{-}KCl}$	355˚C
Density, $\rho_{LiCl\text{-}KCl}$	$\rho(T) = 2.0286 - (5.2676\text{x}10^{-4})T$
Density, $\rho_{LiCl\text{-}KCl,\ 500^{\circ}C}$	$1.62\ \frac{g}{cm^3}$

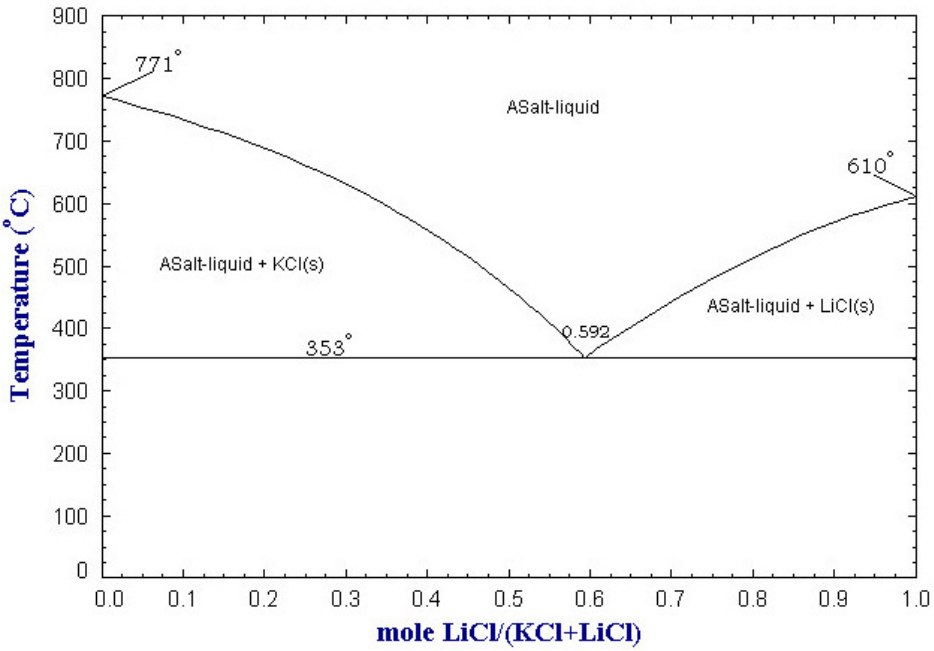

Figure 1. LiCl-KCl phase diagram [7].

Figure 2. LiCl-KCl eutectic salt received from Idaho National Laboratory which was crushed and stored in mason jars (left) and stored inside desiccators (right) to prevent contact with air.

3.1.2 Lanthanide Chlorides

This research has focused on the electrochemical behavior of lanthanide (or rare-earth) elements in LiCl-KCl eutectic. The lanthanide elements were selected because they are present in spent fuel as fission products and accumulate in the salt as electrorefining process progresses. The lanthanides can also serve as surrogates for the actinides which are also very important elements in the salt. The lanthanides act similarly to the actinides yet lack the radiation risks which significantly complicate experimental procedures. There are several factors that should be considered when determining whether an element can serve as a suitable surrogate for an actinide [8]:

- Chemical and physical properties
  - Valence
  - Electronic configuration
  - Ionic radii
  - Coordination
  - Redox potential
  - Density
  - Particle size distribution
- Radioactivity considerations
  - Self-irradiation
  - Radioactive decay products
  - Criticality prevention

Lanthanides are generally good surrogates for actinides given that both groups are Lewis acids, have large ionic radii, and possess flexible coordination geometries that prefer high coordination numbers. The most common lanthanide surrogates for uranium and plutonium are Ce, Eu, Nd, Gd, La, and Sm [8]. Dysprosium is often used as a surrogate for americium. Table II lists various properties of relevant actinides and lanthanides which can be used to predict certain behavior of the elements in the electrorefiner salt and determine which elements can serve as surrogates for others.

Table II. Various properties of actinides and lanthanides [8], [9], [10], [11].

Element	Valence State	Electronic Configuration	Ionic Radius (pm)	Chloride Density (g/cm^3)	Chloride Melting Point (°C)
U	(III)	$[Rn]5f^1$	102.5	5.5	842
U	(IV)	$[Rn]\ 5f^2$	89	4.87	590
Pu	(III)	$[Rn]\ 5f^5$	100	5.71	768
La	(III)	$[Xe]4f^0$	103.2	3.84	860
Ce	(III)	$[Xe]4f^1$	101	3.97	817
Nd	(II)	$[Xe]4f^2$	120	-	841
Nd	(III)	$[Xe]4f^3$	98.3	4.13	759
Dy	(II)	$[Xe]4f^8$	107	-	721
Dy	(III)	$[Xe]4f^9$	91.2	3.67	647

3.1.3 Glove box and Atmosphere Controls

The LiCl-KCl salt and lanthanide chlorides are hygroscopic and need to be stored in an inert environment in order to prevent the formation of hydrates due to interaction with water in the air. In addition, when the salt is in liquid form, the formation of alkali-oxides or rare-earth oxides is possible in the presence of significant oxygen. As a consequence of this fact, all electrochemistry work was performed in a glove box (Vacuum/Atmospheres Company, Model DLX-001-S-P) maintained with an inert argon atmosphere. A PC-1 pressure control system ensured that the pressure inside the glove box was slightly above atmospheric pressure, guaranteeing that any leaks in the glove box would result in argon leaking out of the glove box, rather than air leaking in. A Dri-Train gas purification system

(Vacuum/Atmospheres Company model HE-493) was used to remove O_2 and H_2O from the glove box atmosphere. A Series 3000 Alpha-Omega Trace Oxygen Sensor was used to monitor the oxygen concentration in the glove box (see Figure 4). The H_2O levels were measured with a SHAW moisture meter (model SDA with Red Spot Sensor). The majority of the time, this experimental setup was capable of keeping O_2 and H_2O levels below 1ppm and 2 ppm respectively. The electrochemistry glovebox is shown in Figure 3.

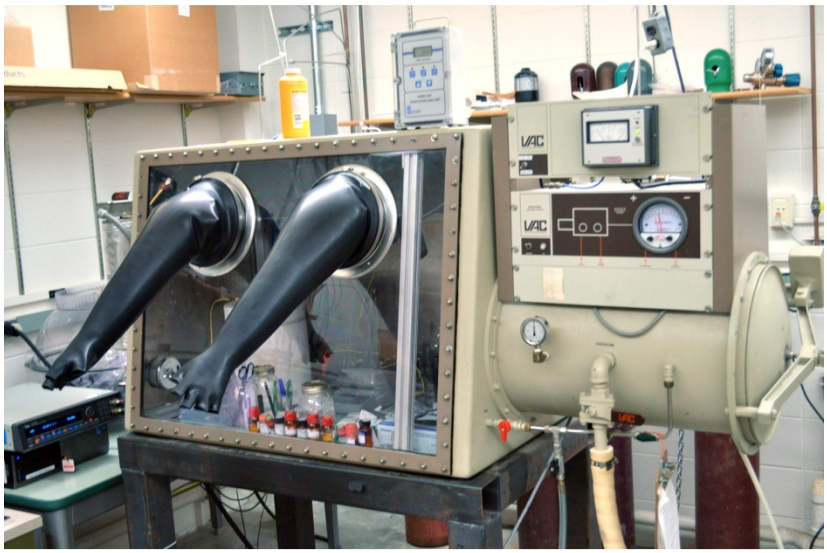

Figure 3. Glovebox used for electrochemistry research.

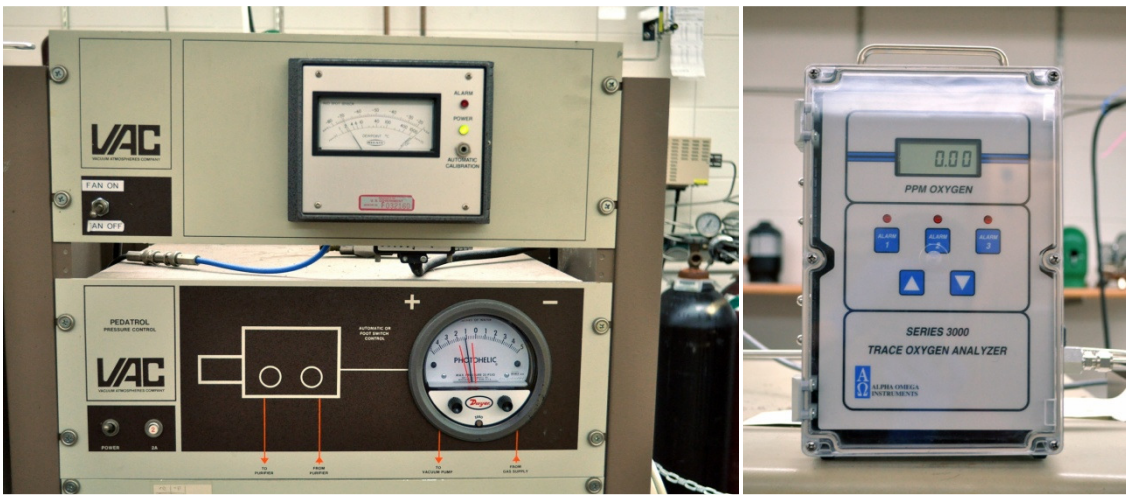

Figure 4. PC-1 pressure control system and SHAW moisture meter (left). Series 3000 Alpha-Omega Trace Oxygen Sensor (right).

3.1.4 Electrochemical Cell

The electrochemical cell used for this research is shown in Figure 5 and Figure 6. The salt is contained within crucibles which sit at the bottom of a cylindrical heater. A quartz structure rests on top of the heater and is used to position electrodes and thermocouples in the molten salt. All of these components are explained in detail in the following section.

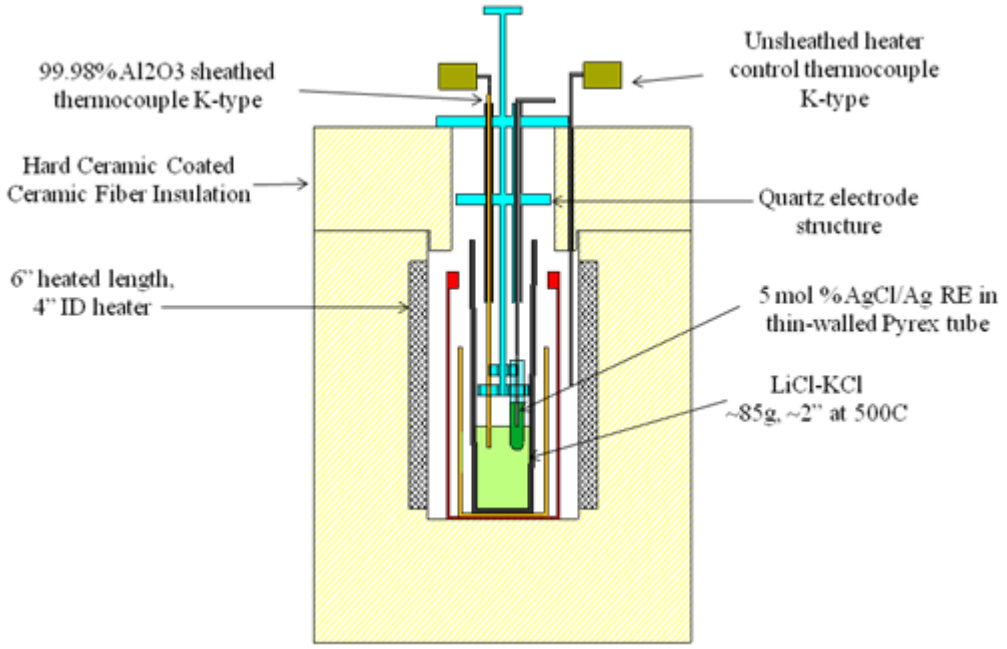

Figure 5. Electrochemical cell design used for electrochemistry experiments. This view shows the thermocouple and reference electrode.

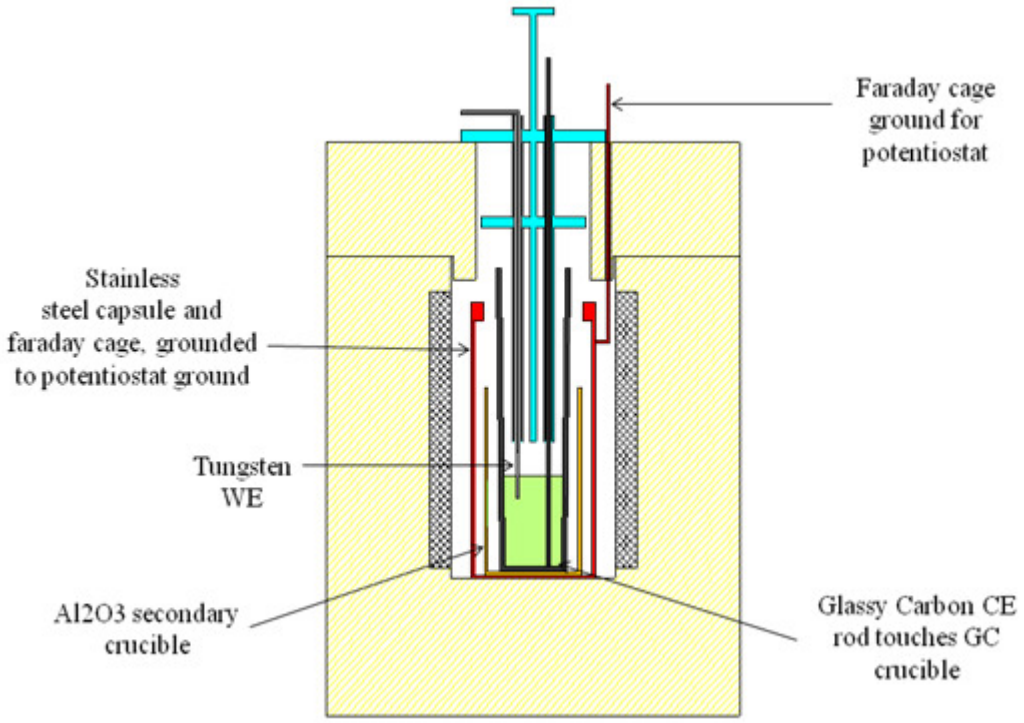

Figure 6. Alternative view of the electrochemical cell showing the working and counter electrodes.

The LiCl-KCl electrolyte was contained within a glassy carbon crucible. Glassy carbon was chosen for its high temperature resistance, low electrical resistance, high corrosion resistance, low thermal resistance, and closed porosity. In addition, the glassy carbon is not wetted by the molten salt, making the removal of the salt ingot from the crucible very easy. The crucibles were purchased from HTW Hochtemperatur-Werkstoffe GmbH in Germany. The SIGRADUR GAT19 model was used for its size and slight taper allowing easy removal of salt ingots. The crucibles have a purity greater than 99.95% glassy carbon. Alumina was originally used in place of the glassy carbon for the primary crucibles; however, frequent cracking of the alumina crucibles prompted the switch. Cracking is still an issue with glassy carbon; however, it is much less frequent and generally occurs after many heating and cooling cycles. The glassy carbon crucible containing the salt was also placed inside alumina and stainless steel crucibles which were then placed into a cylindrical heater. These crucibles simply serve as additional barriers preventing the molten salt from contacting the heater insulation if the glassy carbon crucible happens to fracture during testing. All there cylinders are shown in Figure 7.

Table III. Description of crucibles used in electrochemical cell.

Crucible	Material Detail	Purpose in electrochemical cell
Glassy Carbon	SIGRADUR GAT19	Holds LiCl-KCl eutectic melt for electrochemical measurements
Alumina	99.8% Alumina	Provides a thermal barrier between glassy carbon and stainless steel
Stainless Steel	Grade 316	Welded wire creates a Faraday cage to reduce electronic noise

Figure 7. Glassy carbon (left), alumina (center), and stainless steel (right) crucibles used in the electrochemical cell.

The electrochemical cell used for this work utilized three electrodes: a working electrode, a counter electrode, and a reference electrode. The purpose of each electrode is described below. The

electrodes are of great important to the operation of the electrochemical cell and great consideration was given to the selection of their materials. Table IV lists the electrode materials used for this research.

Working electrode (WE) -- The working electrode is the electrode of interest where the electrochemical measurements are made.

Counter electrode (CE) -- The counter electrode serves to complete the circuit of the electrochemical cell.

Reference electrode (RE) -- The reference electrode is used to accurately measure the potential of the working electrode. This is possible because the reference electrode has a stable electrode potential which serves as a constant reference to measure the working electrode's potential against.

Table IV. Electrode materials and description.

Electrode	Material/Description
Working Electrode (WE)	2.0mm 99.95% Tungsten rod
Reference Electrode (RE)	1.0mm Silver wire in 5 mol% Ag^{+}|Ag solution
Counter Electrode (CE)	3.0mm glassy carbon rod in contact with the glassy carbon crucible

3.1.4.1 Working Electrode

The working electrode (WE) used for this research was a tungsten rod 30 cm in length and 2 mm in diameter. The rods were purchased from Alpha-Aesar and have a purity of 99.95%. Tungsten functions well as an electrode because it is a good conductor and is chemically inert. Tungsten does not react with the molten LiCl-KCl at 500°C. This is important because interaction between the working electrode and rare-earth elements can produce intermetallics which affect the electrochemistry results. In the early stages of this research, platinum was used as a working electrode. However, it was discovered that platinum formed intermetallics with lanthanum additions to the salt that disrupted the electrochemical measurements. Tungsten has often been reported in literature and was found to be a good replacement since it did not produce any intermetallics. Observing Figure 8, it can clearly been seen that tungsten forms far fewer phases with lanthanum than platinum does at 500 °C. Tungsten also does not form any significant intermetallics with the other elements in this study: Ce, Nd, Dy, and U. Figure 9 shows a tungsten-uranium binary phase diagram which displays no significant phase change at 500°C.

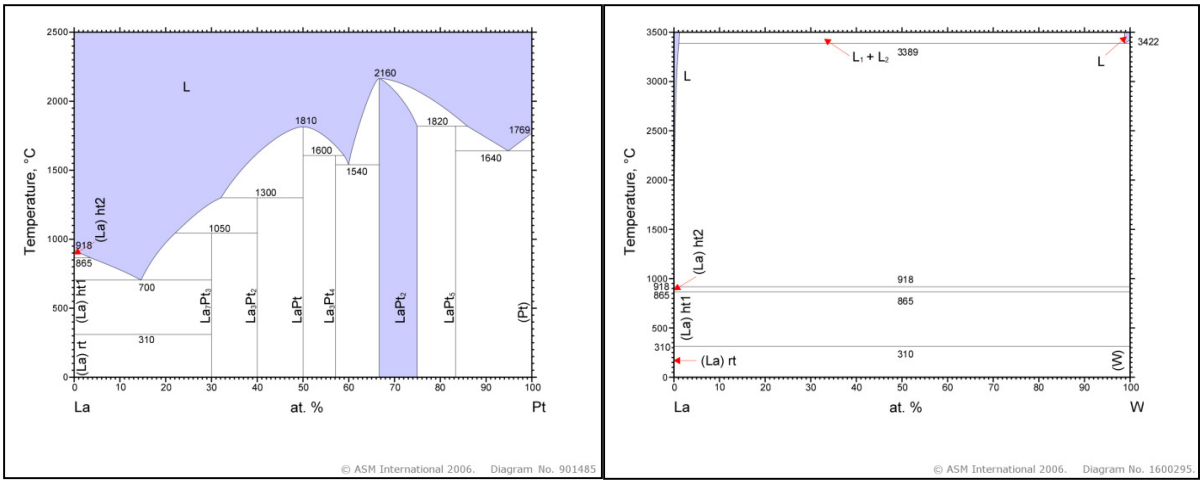

Figure 8 (left) Pt-La phase diagram [12], (right) W-La phase diagram [13]. Note the many intermetallics that form was a function of La concentration on a platinum substrate.

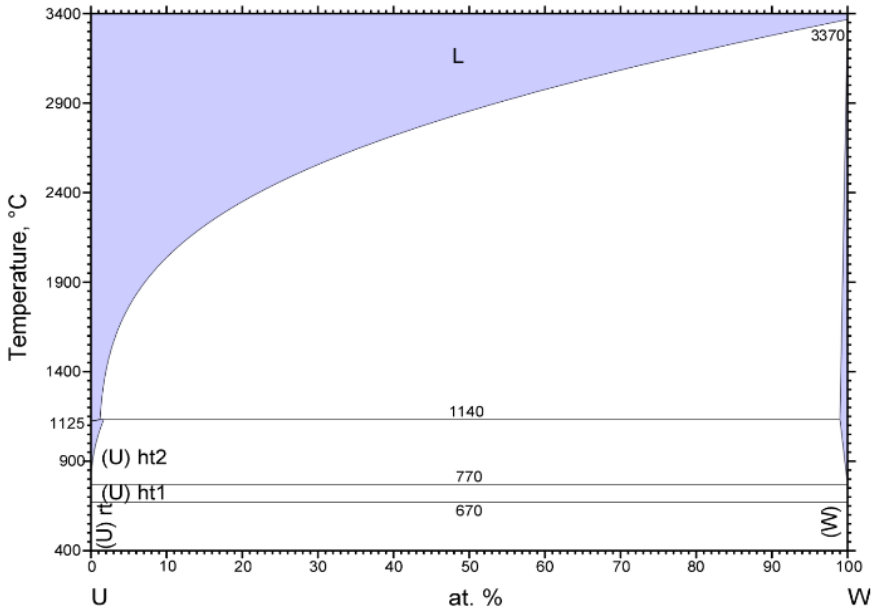

Figure 9. Tungsten-uranium binary phase diagram [14].

3.1.4.2 Counter Electrode

The counter electrode (CE) chosen for this research was a glassy carbon (>99.95%) rod 3 mm in diameter purchased from HTW Hochtemperatur-Werkstoffe GmbH. Once again, glassy carbon was selected for its good electronic conductivity, high temperature resistance, and not-wetting characteristics. The main purpose of the counter electrode is to complete the circuit of the electrochemical cell, allowing current to flow. Therefore, it is necessary to ensure that the counter electrode area in contact with the salt is much larger than the WE area, so that the reaction of interest on the working electrode is not limited by

the area of the CE. In order to accomplish this, the glassy carbon rod is rested on the bottom of the glassy carbon crucible, effectively making the entire crucible in contact with the salt the counter electrode.

3.1.4.3 Reference Electrode

A literature review revealed Ag|AgCl to be a common reference electrode for LiCl-KCl molten salt electrochemistry. AgCl concentrations varied from 1 to 10 mol%. 5 mol% was chosen for this research. A schematic of the reference electrode is shown in Figure 10 and photograph of the setup is shown in Figure 11. A 1.0 mm diameter silver wire (99.9%, Acros Organics) is immersed in a reference solution contained within a 10 mm outer diameter Pyrex test tube. The reference solution is approximately 1.0 grams of LiCl-KCl containing 5 mol% AgCl. The Pyrex test tube is connected to the bottom of the center quartz rod on the electrode structure. This allows the test tube to be partially submerged in the molten salt during testing. The test tube keeps the reference solution physically separated from the bulk salt. However, the thin walls of the test tube (1 mm), allow for ionic conduction between the electrolytes but not electronic conduction. This configuration allows the potential of the working electrode to accurately be measured against the stable reference solution.

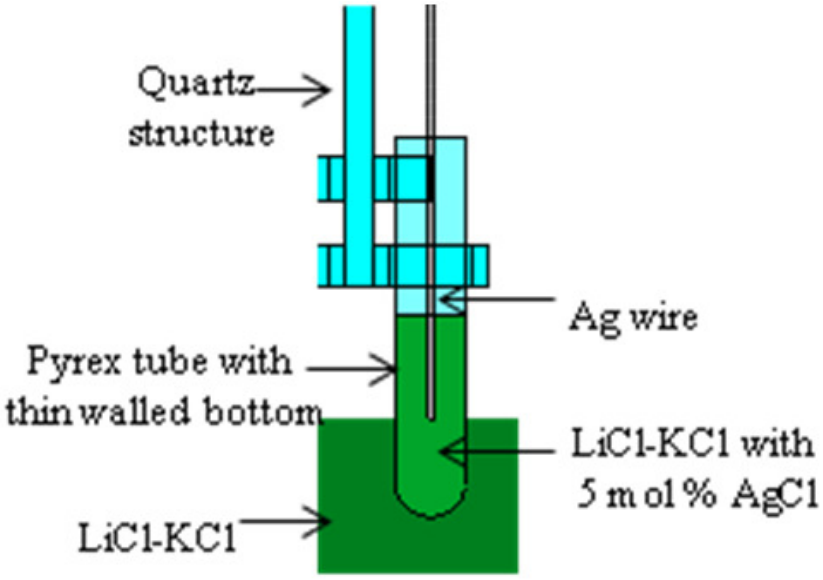

Figure 10. Schematic of the reference electrode submerged in the LiCl-KCl eutectic salt. The Pyrex® tube allows ionic conduction between the reference and working solution but prohibits electronic conductivity

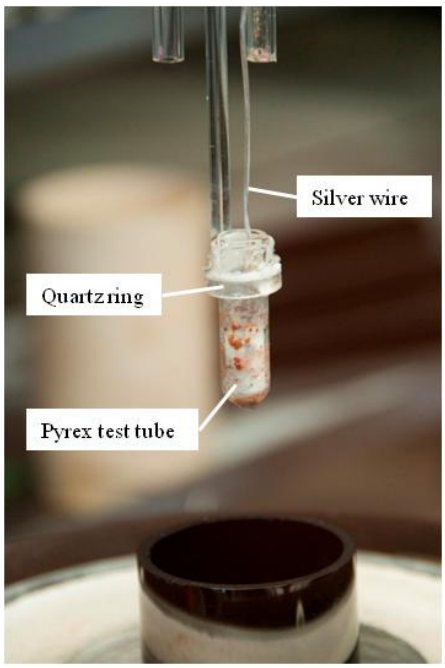

Figure 11. Ag|AgCl reference electrode.

Since many different reference electrodes are utilized for electrochemical research, it is necessary to be able to convert between different concentrations and types of reference electrodes in order to compare results in a meaningful way. Another common scale used in literature is the $Cl^-|Cl_2$ scale. Results of this work will be presented against both the Ag|AgCl and $Cl^-|Cl_2$ scales. Conversion from the 5 mol% Ag|AgCl scale to the $Cl^-|Cl_2$ scale can be performed in the following manner, as demonstrated by Shirai [15].

The apparent standard potential of the Ag|AgCl redox couple can be defined by the following temperature dependent relationship:

$$E^{0'}_{Ag^+|Ag} = -1.076 + 0.0001672T$$

Evaluated at T=773K (500°C):

$$E^{0'}_{Ag^+|Ag} = -0.946754$$

The apparent standard potential must also be corrected to account for the shift in potential due to the concentration of AgCl. This is performed as follows, using the Nernst equation.

$$E^{0}_{Ag^+|Ag} = E^{0'}_{Ag^+|Ag} + \frac{RT}{nF}\ln\left(X_{AgCl}\right)$$

where R is the ideal gas constant, T is the temperature in degrees Kelvin, n is the number of electrons transferred (n=1 here), F is Faraday's constant, and X_{AgCl} is the mol fraction of AgCl in the LiCl-KCl eutectic. For our system at T=773K and a reference solution with X_{AgCl}=0.05:

$$E^{0}_{Ag^+|Ag} = -1.1462957$$

This number can then be used to convert from a 5 mol% Ag|AgCl scale to the $Cl^-|Cl_2$ scale.

3.1.4.4 Electrode Assembly

The electrode assembly is a custom-built quartz structure used to position all of the electrodes and a thermocouple in the salt with the desired immersion depths. Figure 12 shows all of the electrodes and the thermocouple in the electrode assembly. During testing, the large quartz disk on the top of the structure rests on the top edge of the heater. The quartz tubing and disks were purchased from Technical Glass Products, Inc. A high-temperature adhesive (Rocksett Cement by Flexbar Corp.) was used to glue the assembly together. The adhesive was found to maintain its integrity at 500°C and electrochemical results revealed that no contamination of the salt occurred.

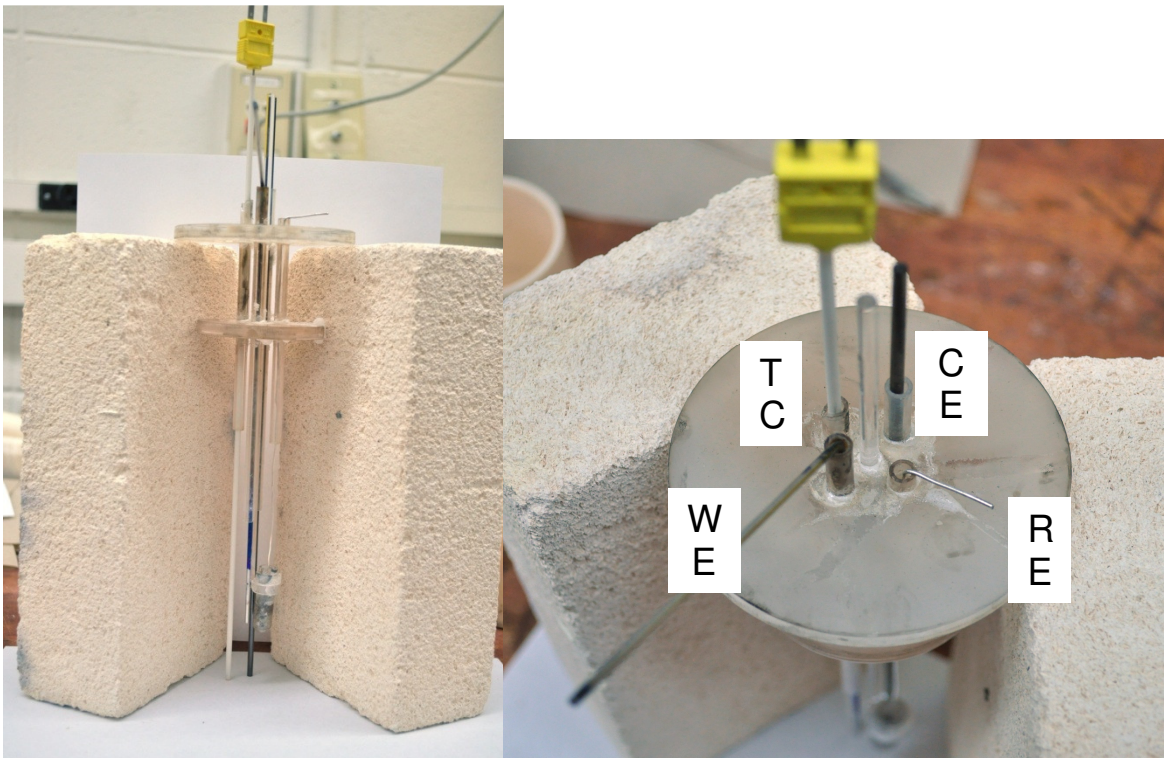

Figure 12. Electrode structure side view (left) and top view (right). (TC = thermocouple, CE = counter electrode, WE = working electrode, RE = reference electrode).

3.1.5 Heater and Temperature Control Equipment

A cylindrical resistance heater coated with ceramic fiber insulation was used to heat the electrochemical cell. The heater was purchased from DS Fibertech Corporation. A k-type thermocouple (Alpha-Omega) in an alumina sheath is held in the salt by the electrode assembly. An additional thermocouple is located at the wall of the heater outside of the stainless steel crucible. The heater is controlled by a data acquisition program, LabView, installed on a PC outside of the glovebox. Both thermocouples and the heater power cables are fed through a port on the glove box and sealed with an epoxy. LabView uses the heater-wall thermocouple to heat the electrochemical cell to the desired temperature and maintain a steady-state temperature. The LabView program was written by an employee in the UW-Madison Engineering -Physics Department. The thermocouple positioned in the salt allows for close monitoring of the salt temperature. During testing, the temperature can accurately be controlled within ±0.2°C.

3.1.6 Data Acquisition System

A Solartron 1287A Electrochemical Interface (Potentiostat) was used to perform the electrochemical measurements. Coaxial cables were used to connect the potentiostat to the electrodes inside the glove box. The cables are fed through a port in the glove box and sealed with an epoxy. A National Instruments GPIB controller (NI GPIB-USB-HS) was used to connect the potentiostat to a USB port on a PC. CorrWare and CorrView electrochemical software (Scribner Associates) was used to collect and analyze data via the potentiostat. Various technical specifications of the potentiostat are listed in Table V. Figure 13 shows a photograph of the potentiostat with electrode leads attached.

Table V. Solartron 1287A technical specifications.

Working electrode	
current measurement resistor range	0.1Ω-1MΩ
full scale current range	2A to 200nA
limit of error	0.1%±0.05% or range
Counter Electrode	
output voltage	>±30V
current	2A
slew rate, potentiostatic control	>10V/μs
Reference electrode	
input impedance	>10GΩ
capacitance	50pF
current	<1nA
limit of error	0.1%±100μV

Figure 13. Solartron SI 1287 potentiostat.

3.1.7 Laboratory Supplies and Equipment

A significant amount of miscellaneous laboratory supplies and equipment were used for the general operations of this research. Cleaning the working electrode was a task which was performed very frequently. This was accomplished using a Dremel Multipro Model 395, 1 μm METADI® II diamond polishing compound (Buehler®), and METADI® fluid expander for diamond abrasives (Buehler®). After polishing the electrode, it was soaked in 6.0 N HCl for 5 minutes to remove any residual salt residue. A Branson 5510 ultrasonic cleaner was used to further clean the working electrode, as well as other electrodes and crucibles, with deionized water or acetone. Nitrile gloves (Fischer Scientific) and KimWipes (Kimtech) were used when cleaning and handling the crucibles and electrodes. Industrial grade argon (99.998%) obtained from AirGas was used to maintain inert atmospheres in the electrochemistry and density experiments. A 95% N, 5 % H compressed gas mixture, also procured from AirGas, was used for regenerating the Dri-train on the electrochemistry glovebox. An Acculab Vicon precision balance was used to weigh salts inside the glovebox.

3.1.8 Depleted Uranium Electrochemical Studies

A short electrochemical study investigating $dUCl_3$ additions to LiCl-KCl was conducted at the Center for Advanced Energy Studies (CAES) at Idaho National Laboratory (INL). Experiments were performed in the radiochemistry laboratory under supervision of Professor Phongikaroon. For the most part, the same experimental setup used at UW-Madison was used for these experiments. Crucibles, electrodes, electrode assemblies, LiCl-KCl salt, and potentiostat were shipped to CAES for the experiments. LiCl-KCl-$dUCl_3$ (50 wt% U) was supplied by INL. Experiments were performed in a radioactive material glovebox (MBRAUN Labmaster 20G) located in the radiochemistry laboratory. The glove box is pictured in Figure 14. An important difference between the glove box at INL and the one at UW-Madison is that the INL glove box contained radioactive material so it was kept at a pressure below atmospheric pressure (compared to the positive pressure of the UW-Madison glovebox). Normally, glove boxes are kept at positive pressure to prevent the ingress of air in the event of a leak. However, when dealing with radioactive material, a positive pressure would spread radioactive material throughout the laboratory if a leak were to occur. So, as a result, a negative pressure was used to ensure that all radioactive material would be confined to the glove box. Built in O_2 and H_2O sensors monitored the glovebox box atmosphere and kept water and oxygen levels below 1 ppm at all times (See Figure 15).

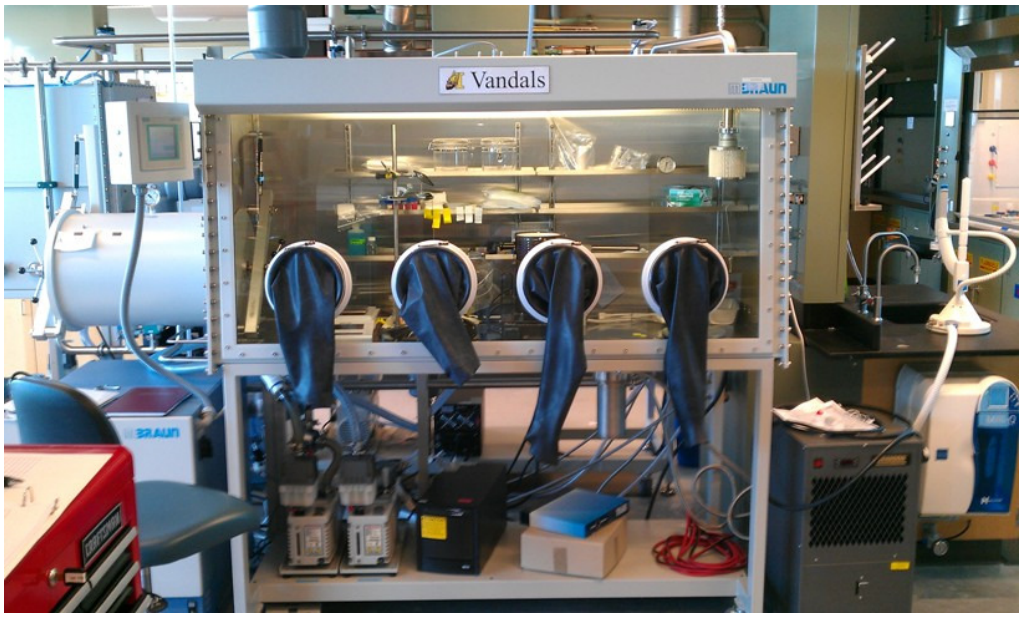

Figure 14. Radioactive material glove box used for depleted uranium electrochemistry work at INL.

Figure 15. Digital control panel on MBRAUN glove box showing O_2 and H_2O levels.

The glove box was equipped with a heater well shown in Figure 16. The crucibles containing the salt were lowered in the well from inside the glove box. The heater was placed around the well on the outside of the glovebox. Allowing the heater to remain outside the glovebox dramatically simplified the troubleshooting required for any issues with the heater since there is no need to remove the heater from the glovebox which requires a tedious survey process to test for radioactive contamination. The upper portion of the heater well was fitted with a water cooling jacket to remove excess heat. Preliminary tests with this heater setup found that the time required to heat the salt to 500°C was extremely long. The ¼" inch thick stainless steel heater well, three crucibles, and air gaps provide significant thermal resistance. In order to reduce the heating time, it was decided that a smaller heater located inside the glovebox would be used. The heater well still has the possibility to be used for future experiments with a few

modifications. Utilizing a conductive material to fill existing air gaps may be sufficient to reduce heating times to reasonable values. Due to time constraints, a KerrLab Auto Electro Melt Maxi furnace (Model 31811) was used for this study (See Figure 17). The heater was located and operated inside the glove box. Due to the smaller diameter of the heater, only the glassy carbon and alumina crucibles were able to fit inside. A graphite crucible inside the heater replaced the stainless steel crucible as a third layer of defense. A stand located next to the heater was used to hold the quartz electrode structure and position it at the correct depth in the salt. Figure 18 shows the quartz structure containing the electrodes lowered into the glassy carbon crucible before and after the electrode leads were attached.

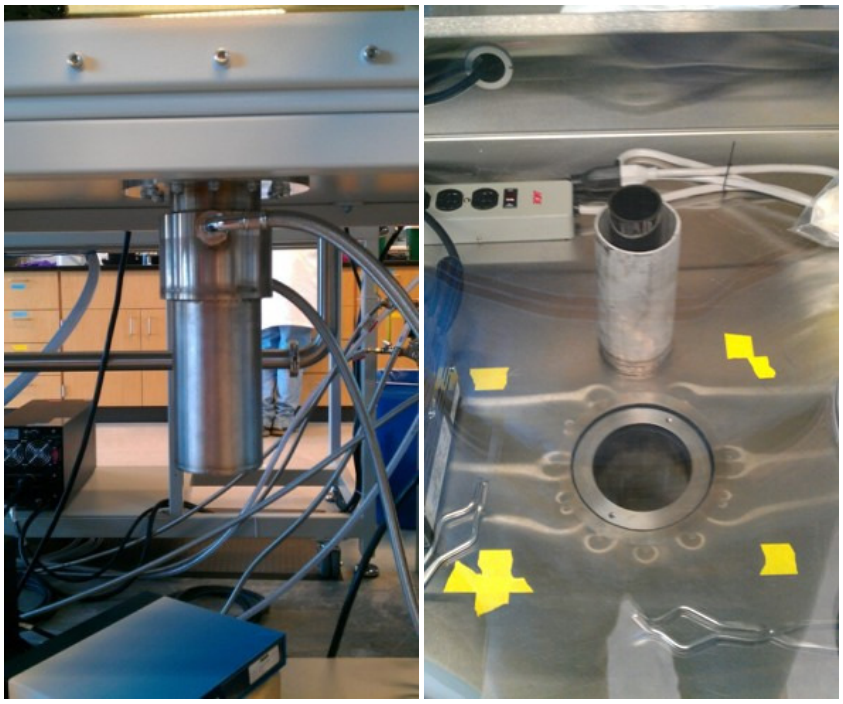

Figure 16. Heater well viewed from outside (left) and inside (right) of the glove box.

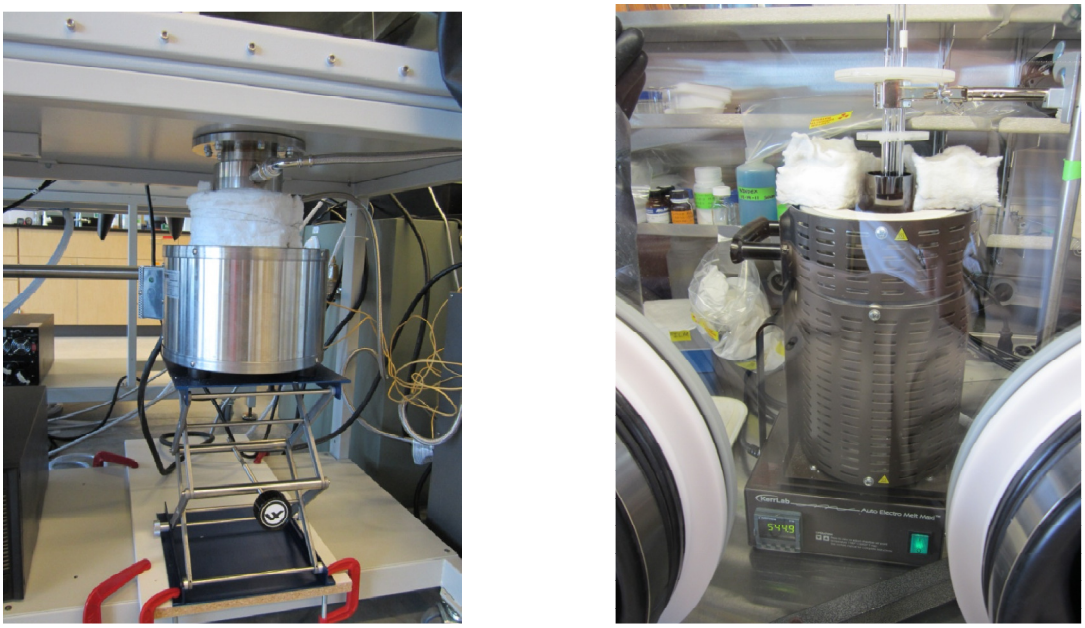

Figure 17. Thermcraft heater raised into position around the heater well (left). KerrLab Auto Electro Melt Maxi furnace positioned inside the glovebox (right).

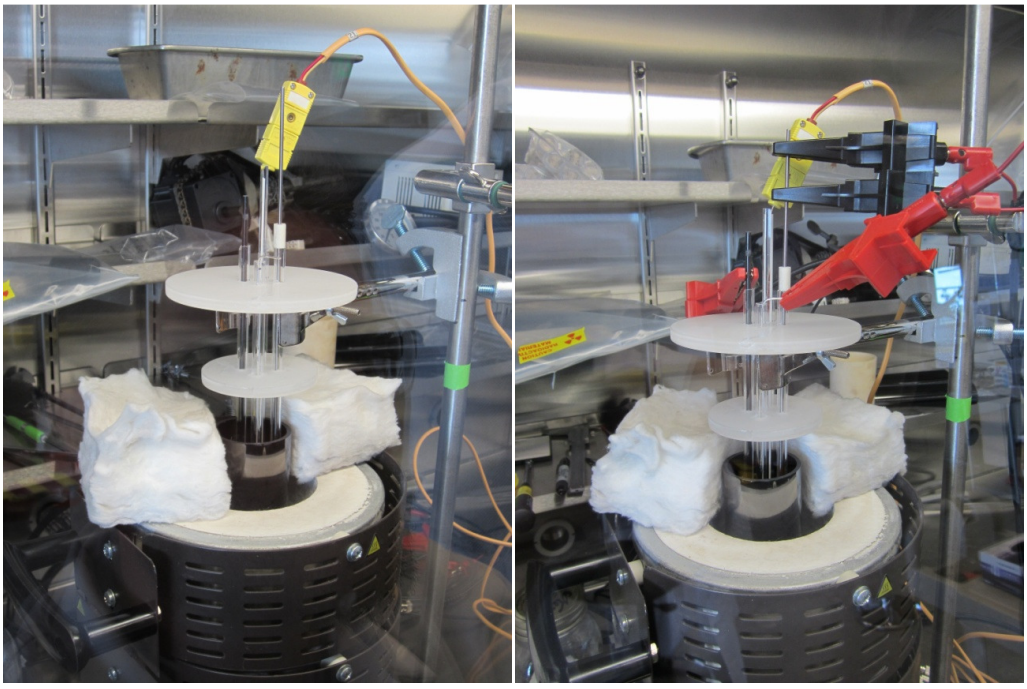

Figure 18. Quartz electrode structure lowered into glassy carbon crucible inside of heater. The left view is before the electrode leads were attached.

3.1.8.1 Radiation Safety and Control

Working with depleted uranium and other radioactive materials in the radiochemistry laboratory requires specific training and handling procedures in order to ensure the safety of all laboratory personnel. Several training courses are required before entry into the lab is permitted. The CAES Facility Orientation and Core Lab Training prepare a user for general laboratory operations. The Idaho State University Radiation Introduction Training and CAES Radiological Primer and Lab Orientation prepare a user to safely work with radioactive material. The radiochemistry laboratory training and walkthrough orient the user to the specific equipment and procedures of the radiochemistry lab. A hands-on glovebox training session allowed the user to practice properly transferring materials into the glovebox and safely handling them once inside.

Once all training was completed, entry to the laboratory was permitted. A dosimeter must be worn at all times in the laboratory in order to keep track of the dose received by each person. A yearly limit of 5 rem is enforced and a there is a notification required at 25 mrem/quarter. Additionally, a radiation survey of the hands and feet was performed prior to exiting the lab. This ensures that all radioactive materials are confined to the laboratory. Personal protective equipment was utilized to protect sensitive body parts from contact with hazardous materials. Safety goggles were worn at all times in the lab and a lab coat was worn when running experiments. When working inside the radioactive material glovebox, nitrile gloves were worn and they were taped to the laboratory coat to prevent radioactive material from contacting the arms. Every time a hand is removed from the glovebox, it was immediately surveyed with meters capable of detecting alpha, beta, and gamma radiation. This practice helps to detect any leaks in the gloves immediately and to prevent the accidental spread of radioactive material around the laboratory. Additionally, every time material is transferred out of the glovebox through the antechamber, a health physicist is present to perform a survey of the antechamber to ensure there is no significant contamination occurring.

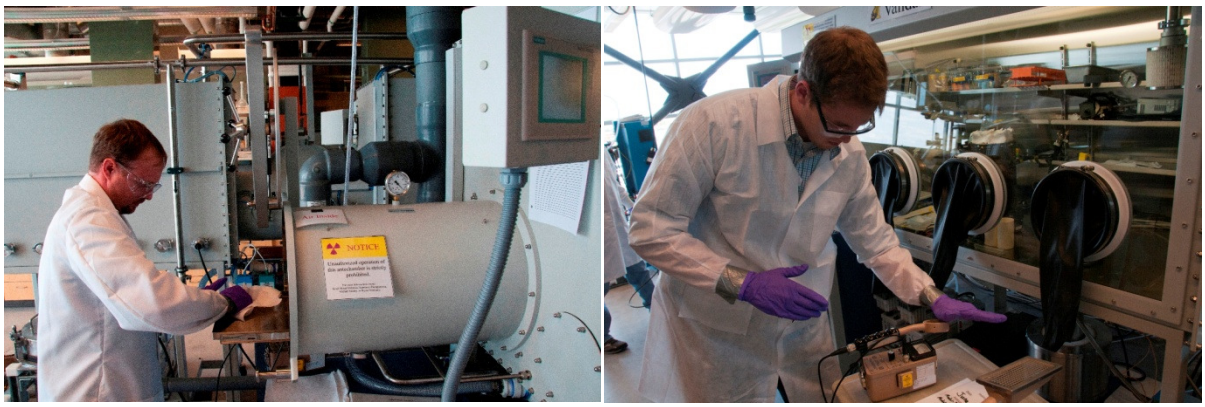

Figure 19. Cleaning and performing survey of antechamber (left). Surveying hands after working in glovebox (right).

3.2 Molten Salt Density

The molten salt density measurement apparatus was custom built at UW-Madison. The experimental setup is shown in Figure 20. The molten salt density is determined by measuring the mass of a nickel bob in air and immersed in the molten salt. The nickel bob, shown in Figure 21 is attached to the bottom of an Acculab Atilon (Model ATL-224-I) balance via a thin (0.02 mm) NiCr wire. Nickel was

chosen as a bob material due to its corrosion resistance in molten salts. The analytical balance had a readability, repeatability, and linearity of 0.1 mg, 0.1 mg, and 0.2 mg respectively.

The bob is suspended inside a sealable chamber above a glassy carbon crucible containing the molten salt. The glassy carbon crucible sits inside a larger alumina crucible which sits inside a cylindrical ceramic resistance heater. The balance rests on an adjustable height platform that is electronically controlled. This adjustable platform allows the bob to be lowered into the molten salt. Mirrors on the inside wall of the chamber allow the operator to see into the glassy carbon crucible through a window in the sealed chamber during operation. The chamber can be evacuated with a vacuum pump and backfilled with argon to maintain an inert atmosphere. Figure 22 shows a view inside the density chamber as well as a close-up view of the nickel bob suspended over the heater.

The heater is controlled via a LabView program installed on a PC. Thermocouples are located at the heater water as well as in the salt. The thermocouple located in the salt is placed inside an alumina sheath which is held in the salt by an adjustable clamp resting on the top of the heater. The heater power control and thermocouples are input into LabView using a National Instruments cDAQ-9174 chassis and NI 9211 and 9263 inputs cards. The temperature of the salt can accurately be controlled within ± 1°C.

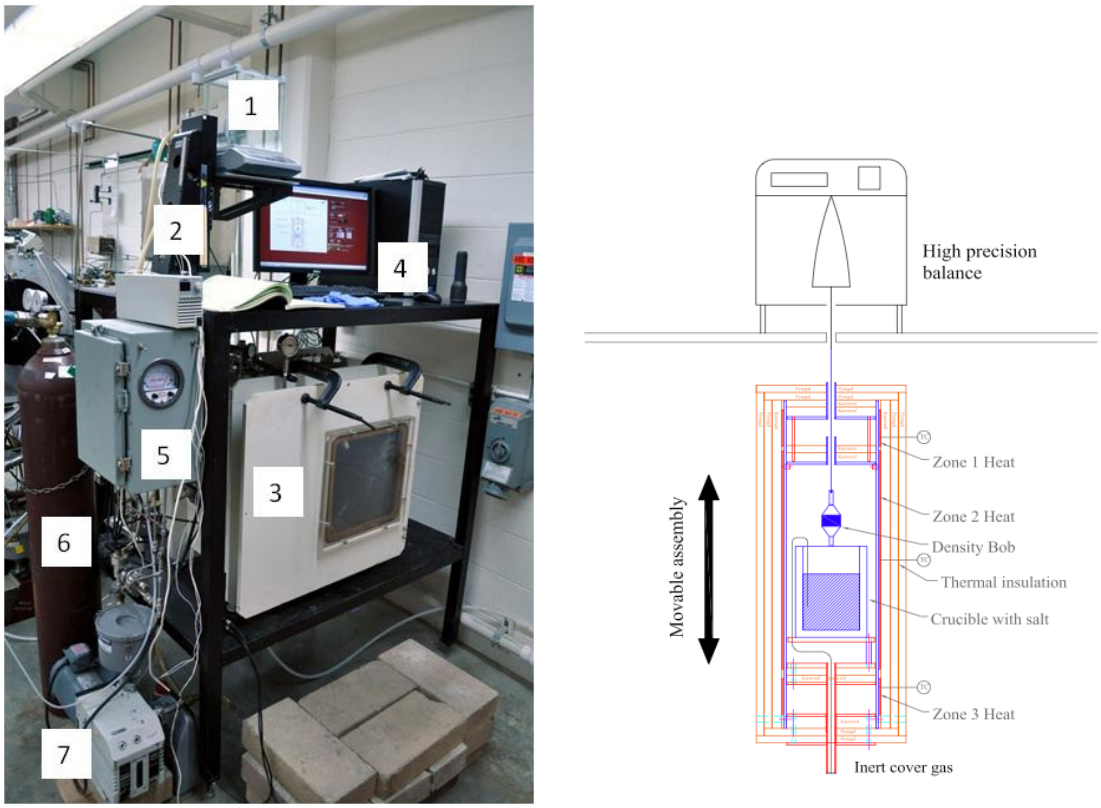

Figure 20. Molten salt density measurement system. A photograph is shown on the left and a general schematic is shown on the right. 1 - high precision balance, 2 - adjustable height platform, 3 - sealable chamber, 4 - PC with LabView, 5 - pressure control system, 6 - compressed argon gas, 7 - vacuum pump.

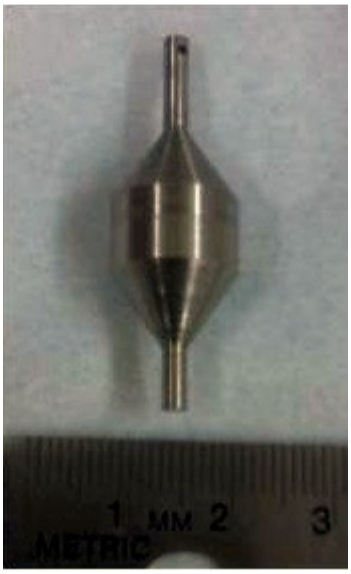

Figure 21. Nickel bob used to measure the density of the molten salt.

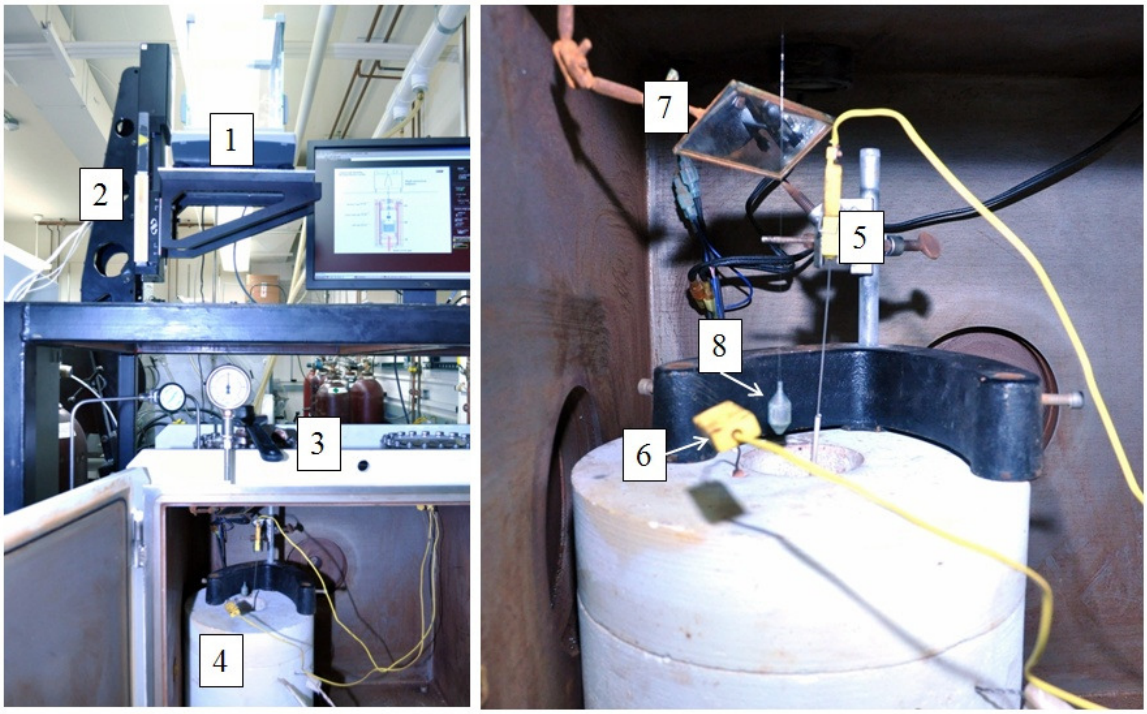

Figure 22. View inside density chamber (left) and a close up view of the bob suspended over the heater inside the chamber. 1 - analytical balance, 2 - adjustable height platform, 3 - sealable chamber, 4 - heater, 5 - salt thermocouple, 6 - heater wall thermocouple, 7 - mirror, 8 - nickel bob.

3.3 Differential Scanning Calorimetry

The melting point of LiCl-KCl salt samples containing various concentrations of rare-earth chlorides were investigated using a differential scanning calorimeter. The samples were prepared in the electrochemistry glove box. 2 grams of LiCl-KCl was placed in a small 16 ml glassy carbon crucible with the desired amount of rare-earth chloride. The crucibles, shown in Figure 25, were purchased from HTW Hochtemperatur-Werkstoffe GmbH in Germany (Model GCG 16). Three of these glassy carbon crucibles were placed in an alumina crucible which was then placed in a stainless steel crucible. The stainless steel crucible was placed inside the cylindrical heater in the glove box. In order to melt the samples and create a homogeneous mixture of the LiCl-KCl and rare earth chlorides, the samples were heated to 500°C and held there for 2 hours. Then the samples were allowed to cool until they were solidified before being heated to 500°C for an additional 2 hours.

Salt melting point measurements were made with a TA Instruments Q100 Modulated Differential Scanning Calorimeter (DSC) which is shown in Figure 23. Figure 24 depicts some of the finer design elements of the DSC. The heat flow sensor is machined from a single piece of constantan (copper-nickel alloy) and is brazed directly to the silver heating block. This allows for faster signal response, and improved sensitivity and resolution. A chromel (nickel-chromium alloy) area thermocouple is welded to the underside of the sample and reference heat flow sensor platforms. A chromel/constantan thermocouple is located between the sample and reference heat flow sensor platforms and serves as an independent temperature measurement for furnace control. The furnace is manufactured from silver due to its high thermal conductivity. This gives the DSC extremely fast temperature response and allows heating rates up to 200°C. Nickel cooling rods connect the furnace to a cooling ring. This design produces faster cooling rates and lower temperatures. Additional technical specifications are listed in Table VI.

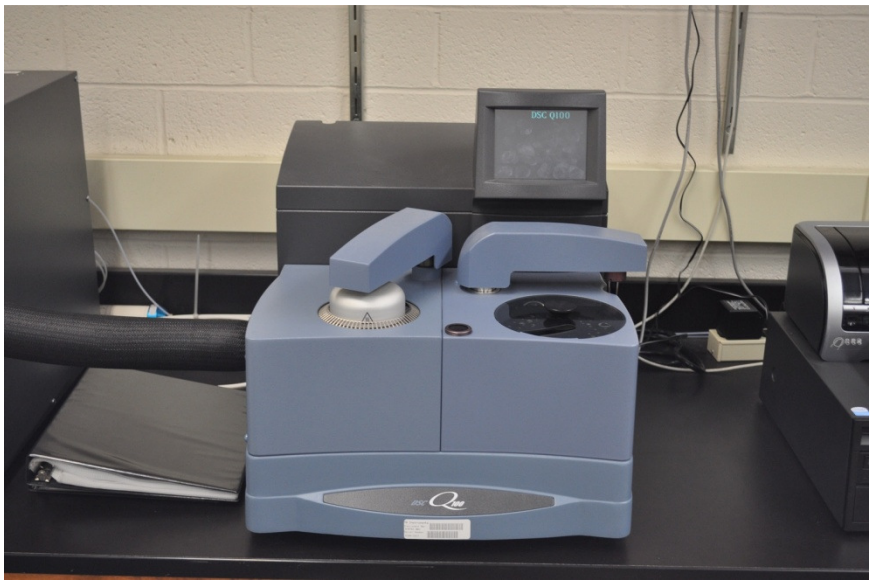

Figure 23. TA Instruments Q100 Modulated Differential Scanning Calorimeter.

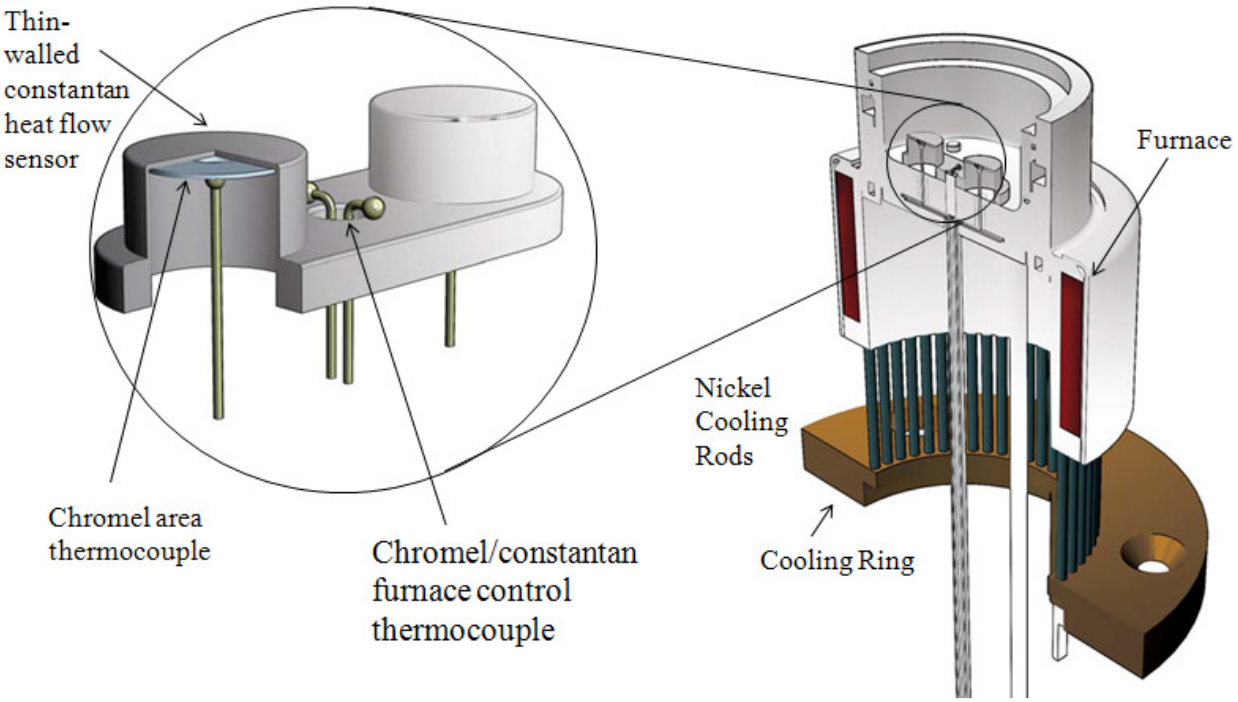

Figure 24. Q100 Modulated DSC Design [16].

Table VI. TA Instruments Q100 Modulated Differential Calorimeter technical specifications [16].

Temperature Range	Ambient to 725 °C
With Cooling Accessories	-180 to 725 °C
Temperature Accuracy	+/- 0.1 °C
Temperature Precision	+/- 0.01 °C
Calorimetric Reproducibility (indium metal)	+/- 0.05 %
Calorimetric Precision (indium metal)	+/- 0.05 %
Dynamic Measurement Range	>+/- 500 mW
Baseline Curvature (Tzero; -50 to 300 °C)	10 µW
Baseline Reproducibility with Tzero	+/- 10 µW
Sensitivity	0.2 µW
Indium Height / Width (mW/°C)*	60

Figure 25. Glassy carbon crucibles used to melt DSC samples.

4. Theory

Electrochemical, density, and differential scanning calorimetry theory relevant to this research are discussed in the following section.

4.1 Molten Salt Electrochemistry

It should be noted that electrochemistry has a broad variety of applications and the electrorefining of spent nuclear fuel in molten salt represents a small portion of the larger field of electrochemical-based technologies. Since electrochemistry is central to this research, this section is written to provide adequate basic knowledge in electrochemistry and its techniques to provide understanding for the remainder of discussion in this thesis.

4.1.1 Reduction/Oxidation Chemistry Basics

Electrochemistry as studied in modern science is concerned mostly with exploitation of the electric charge transfer capabilities of an electrochemical cell across membranes and through ionic solutions [17]. A general electrochemical cell, shown in Figure 26, consists of a two half-cells, which itself consists of an electrode and electrolyte. The overall voltage of the electrochemical cell, also called a galvanic cell, is determined by the standard potential of the electrode materials at the cathodic and anodic sides of the cell.

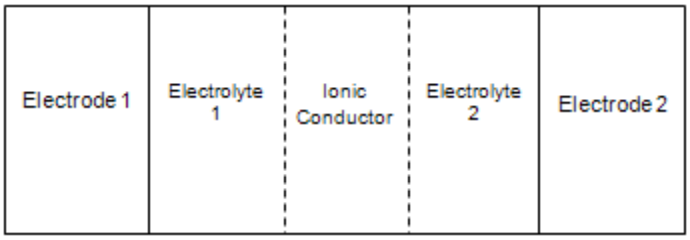

Figure 26. General electrochemical cell. Electrode and electrolyte couples 1 and 2 are half-cells individually and make the full electrochemical cell when combined. Ionic separator is optional depending on if electrolytes 1 and 2 are the same material [17].

The cathode is the electrode at which reduction of an oxidized species occurs (electrons are consumed). The anode is the electrode where oxidation of a reduced species occurs. In a full electrochemical cell, oxidation occurs at the anode at the same time reduction occurs at the cathode. The following equation shows how a species may undergo reduction or oxidation depending on the environmental potential, which is more commonly referred to as a redox reaction.

$$O + ne^{-} \rightleftarrows R$$

where O is the oxidized form of a species, R is the reduced form of the species, and n is the number of electrons transferred in the redox reaction [18].

Electrochemistry as applied to molten salts is based mostly in the controlling of the previously-mentioned oxidation and reduction reactions. Molten salt is an attractive electrolyte and an important part of the electrochemical cell, due to its ability to conduct ionic current easily. Typical electrode materials for molten salt electrochemistry have been discussed in the previous sections.

The potentiostat used to conduct electrochemical experiments in this work is capable of forcing either oxidation or reduction reactions to occur at the working electrode based on the potential applied with respect to a reference electrode. It is typical to use a three-electrode configuration in controlled-potential studies to gather reproducible data independent of sample composition or sample potential which may vary based on composition [18].

The three-electrode electrochemical cell used in this work is shown in Figure 27. The electrodes are a tungsten working electrode, a silver wire dipped in a closed-ended Pyrex® tube filled with a 5 mol% $Ag^{+}|Ag$ solution as a reference electrode, and a glassy carbon rod connected to the glassy carbon cell crucible as a counter electrode. The electrodes are all immersed in the molten salt electrolyte bath and are then connected to the potentiostat.

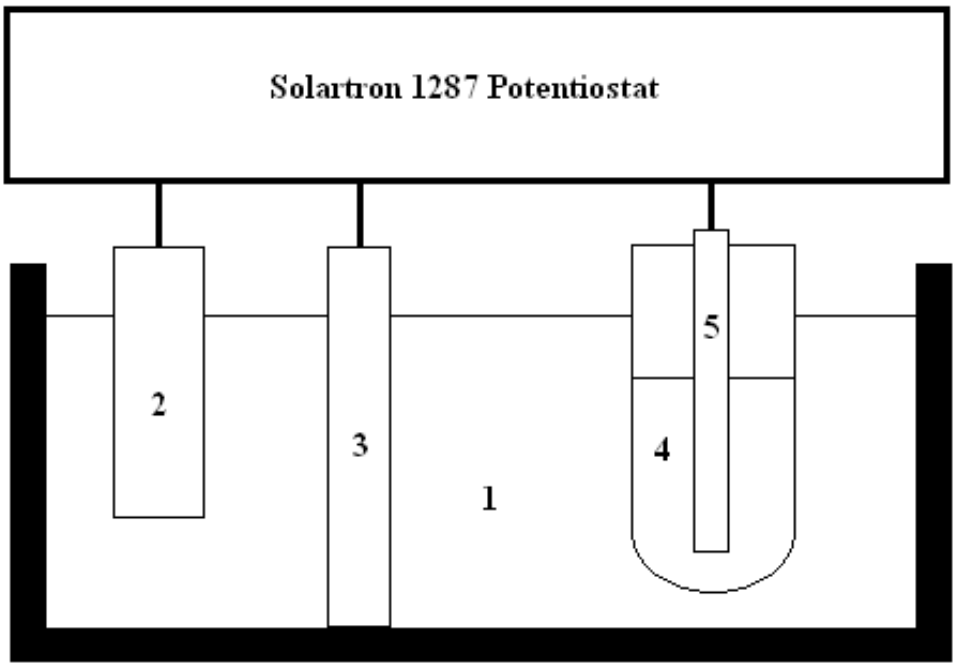

Figure 27. UW's molten salt electrochemical cell with attached potentiostat. 1 – Molten LiCl-KCl eutectic salt (electrolyte), 2 – Tungsten working electrode, 3 – Glassy carbon counter electrode in contact with glassy carbon crucible, 4 – 5 mol% Ag+|Ag reference.

There is no designated cathode or anode in the potentiostat-controlled electrochemical cell. Instead, depending on the potential applied by the potentiostat, the working and counter electrode switch roles as cathode or anode. If reduction is occurring at the working electrode, as in electroplating, the working electrode becomes the cathode and the glassy carbon becomes the anode, and vice versa.

The potentiostat is able to control both potential and current as well as measure both quantities. This makes the potentiostat an important tool in analytical redox chemistry. Figure 28 and Figure 29 show the UW electrochemical cell while illustrating the oxidation and reduction at the working electrode. Depending on the direction of reaction, electrons either flow from the working electrode to the counter electrode (oxidation) or from the counter electrode to the working electrode (reduction).

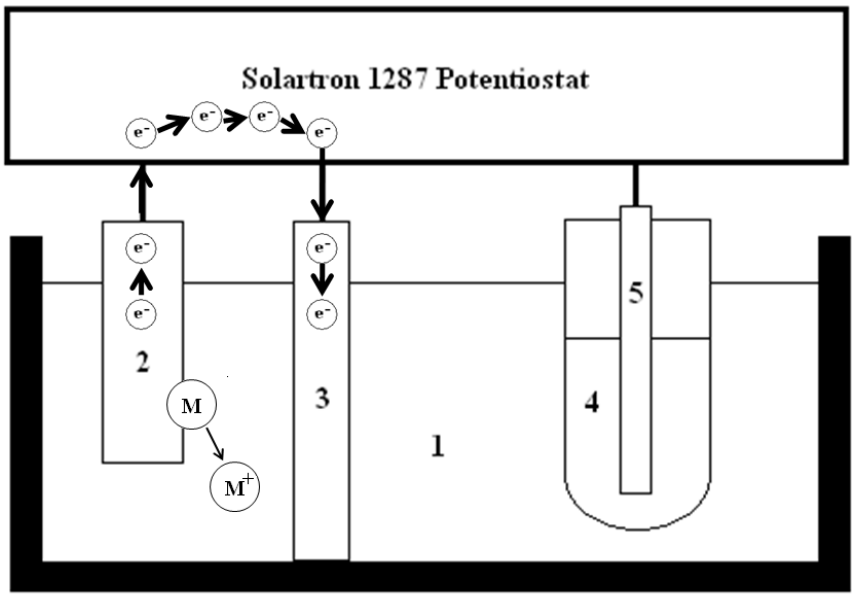

Figure 28. Schematic of oxidation in the UW electrochemical cell. During oxidation, current flows from the working electrode to the counter electrode, deplating, or oxidizing, a specific metal on the working electrode surface depending on the potential.

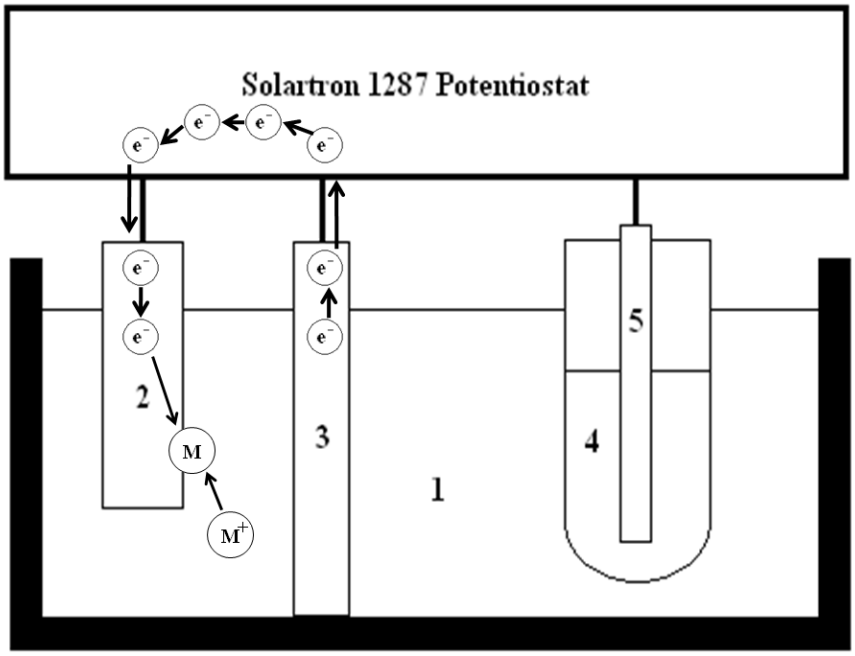

Figure 29. Schematic of reduction in the UW electrochemical cell. During reduction, current flows from the counter electrode to the working electrode, reducing a specific metal from its ionic state in the electrolyte to the its metallic, or reduced, state.

Depending on the number and rate of electrons transferred during reduction or oxidation, an upsurge in current (i.e. a peak in current) occurs at a given potential. The peak height is proportional to the

concentration of analyte in the molten LiCl-KCl eutectic solution. This relationship between molten salt composition and the resulting currents and potentials has been studied vigorously and has given rise to various electrochemical techniques.

The governing equations of electrochemistry are the Nernst equation and the Butler-Volmer equation. The Nernst equation, shown below, predicts the equilibrium behavior of the potential as a function of temperature and analyte concentration both in reduced and oxidized states. An electrochemical system is usually referred to exhibit Nernstian behavior if it is controlled by the laws of thermodynamics (i.e. is in equilibrium) [18].

$$E = E^0 - \frac{RT}{nF} \ln\left(\frac{a_{Red}}{a_{Ox}}\right)$$

where E is the potential at the temperature of interest, E^0 is the standard potential from the EMF series, R is the gas constant, T is the temperature, n is the number of electrons transferred in reduction/oxidation, F is the Faraday constant, a_{red} is the activity of the reductant, and a_{ox} is the activity of the oxidant. For most liquid systems, activity can be changed to concentration.

A system that is not in equilibrium will have current flowing due to reduction or oxidation reactions occurring. Systems in which reactions are controlled by the rate of electron transfer are governed by the Butler-Volmer equation, shown below, which describes current-potential dependency [18].

$$i = i_0 \left\{ \exp\left[\frac{-\alpha n F \eta}{RT}\right] - \exp\left[\frac{(1-\alpha) n F \eta}{RT}\right] \right\}$$

where i is the net cathodic current density, i_0 is the exchange current density, η is the overpotential ($E-E^0$), and α is the symmetry factor.

4.1.2 Electrochemical Techniques

Three primary electrochemical techniques were identified for in this research project: anodic stripping voltammetry (ASV), cyclic voltammetry (CV), and chronopotentiometry (CP). Although there are many intriguing electrochemical techniques, it was decided that the combination of these three techniques would be adequate to achieve the central goals of this project.

In addition, an open circuit potential method was applied to extract the apparent standard potential more accurately than would be possible with the cyclic voltammetry method. Although various researchers have used this technique, its potential was never fully realized by the present author until much later in the experiment. Hence, it deserves a discussion, but was never actually used to analyze any of the electrochemical data since the CV data was consistently available throughout all the electrochemical experiments.

4.1.2.1 Anodic Stripping Voltammetry (ASV)

ASV consists of plating an analyte onto the working electrode by applying a reducing potential. This reducing potential is held for a period of time called the 'plating time'. If smaller concentrations of analyte are present in the molten salt, longer plating times must be used. In general, the longer the plating time, the larger the peak will be. It should be noted that in flowing systems with a high concentration of analyte, convection can cause stripping of the plated surface area of the working electrode thereby leading to a diminished peak. All experiments in the present project were performed using static salts.

Once the analyte is sufficiently plated, the voltage can be ramped to a more anodic (positive) potential. When potential reaches the electromotive force of the analyte, the species oxidizes and a

current spike is observed. The height of this peak and the peak potential is proportional to the concentration of analyte in solution.

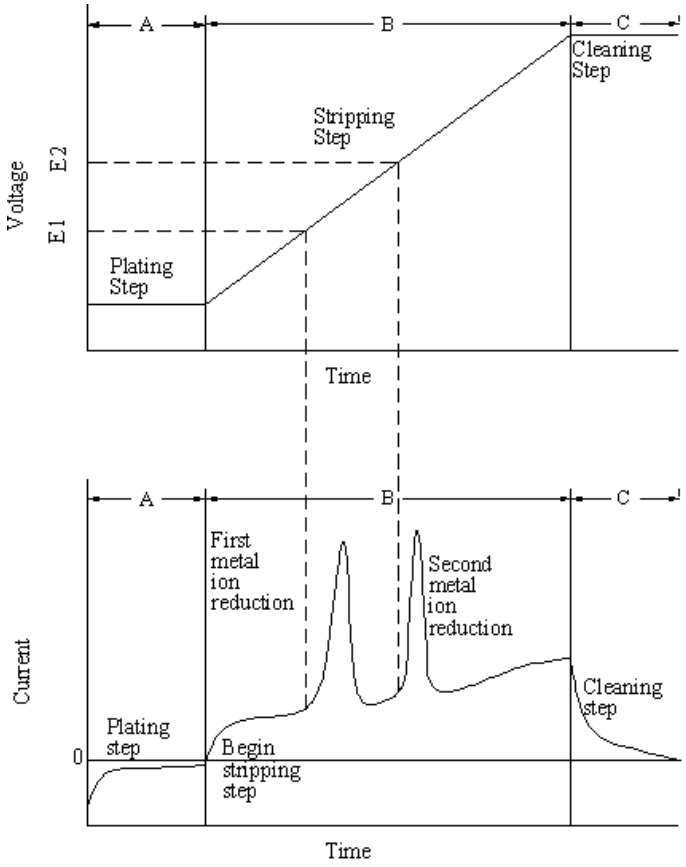

Figure 30. Potentiostatic steps (top) and resulting voltammograms (bottom) for an electrochemical cell with two metals with standard potentials E1 and E2. Adapted from [19].

Using Figure 30 as a model, section A shows the current response to the reduction of the bulk ionic analyte to metal on the surface of the working electrode, section B shows the anodic (positive) sweep in which oxidation peaks occur based on the standard potentials of analytes in the solution, and section C shows the cleaning step, which is simply a precautionary step to make sure the working electrode is clean of plated analyte.

If no plating step performed, the peak current of the oxidation peak during the linear sweep step has been shown to follow the Randles-Sevcik equation, and with the cylindrical geometry used here, it can be written as [19]:

$$i_p = \left(0.446 + 0.344\left(r\sqrt{\frac{nFv}{RTD}}\right)^{-0.852}\right)nFAC\left(\sqrt{\frac{nFvD}{RT}}\right)$$

where i_p is the peak current, r is the radius of the electrode, n is the number of electrons transferred in the given redox reaction, F is the Faraday constant, v is the scan rate, R is the ideal gas constant, T is the temperature, D is the diffusion coefficient, and C is the concentration of analyte in the bulk solution. However, once plating time is added, the direct application of the Randles-Sevcik equation is no longer

valid, since peak current increases with plating time. Repeatability can be enhanced by waiting a specific time between ASV measurements due to diffusion of the analyte metal ion in LiCl-KCl.

It is evident that ASV is a strong technique for detecting small concentrations of impurities in a greater bulk solution. At higher impurity concentrations, such as in pyroprocessing salt, ASV may be less useful due to surface saturation of electrodes resulting from the pre-concentration step of an already abundant impurity onto the working electrode's surface.

4.1.2.2 Cyclic Voltammetry (CV)

Cyclic voltammetry (CV) is a common electrochemical analysis technique. In CV, potential is ramped anodically and then reversed in the cathodic direction between two vertex points repeatedly at a constant scan rate, and the analyte both reduces and oxidizes on the WE surface. In general, the more repetitions of the cyclic sweep, the better the resulting voltammograms assuming no adsorption effects at the electrode surface [18]. Figure 31, Figure 32, and Figure 33 all depict the cyclic voltammogram with differing axes to depict how CV commences as a function of time and how a CV voltammogram is usually viewed on a current-voltage plot.

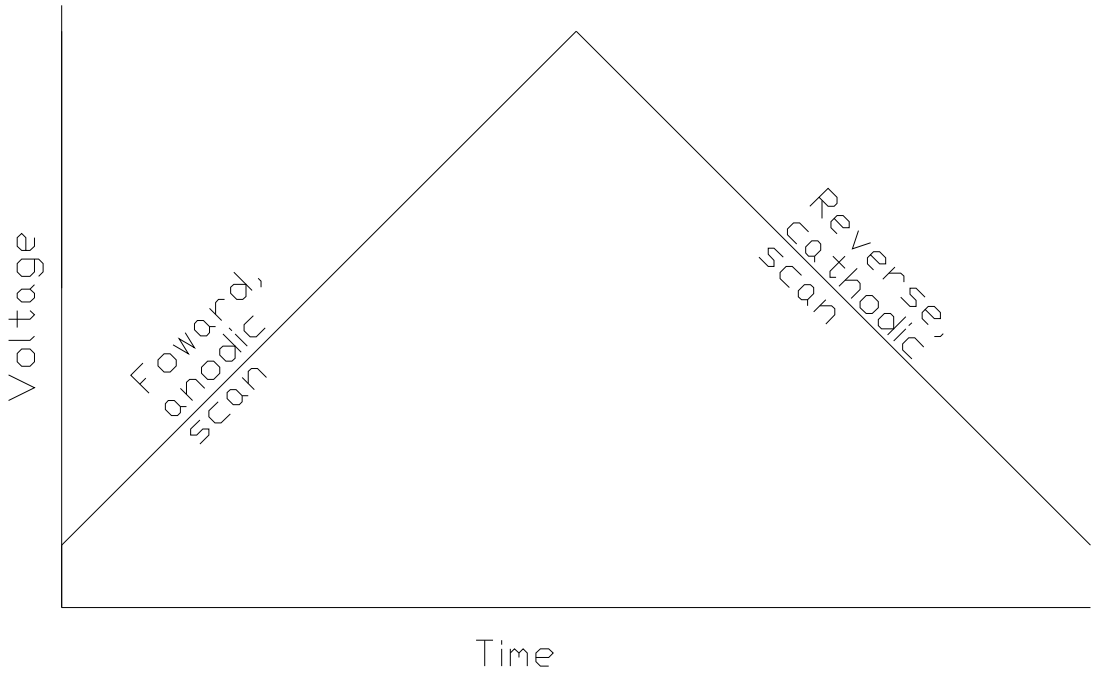

Figure 31. Voltage as a function of time for CV [19].

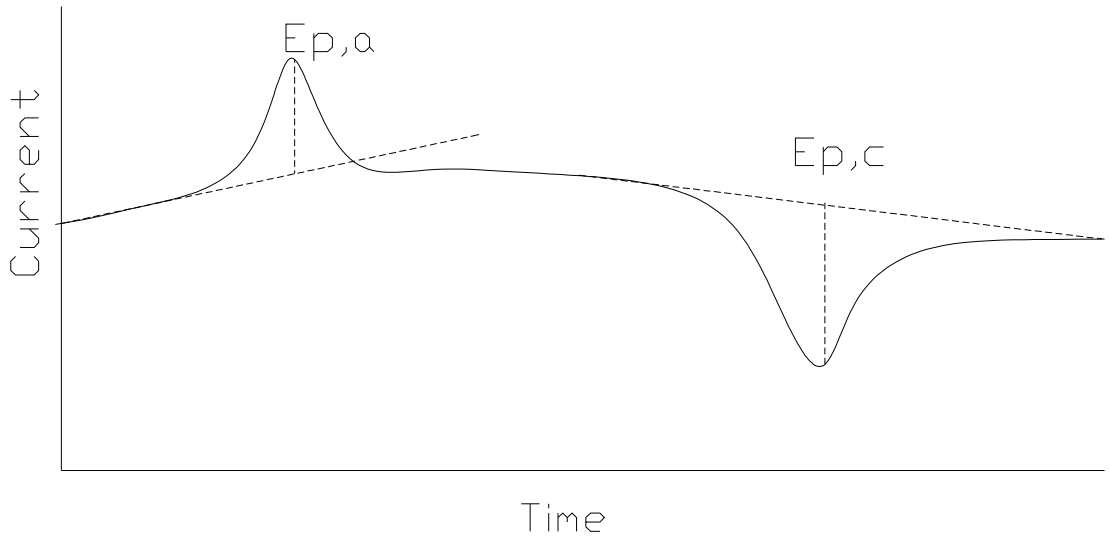

Figure 32. Current as a function of time for CV [19].

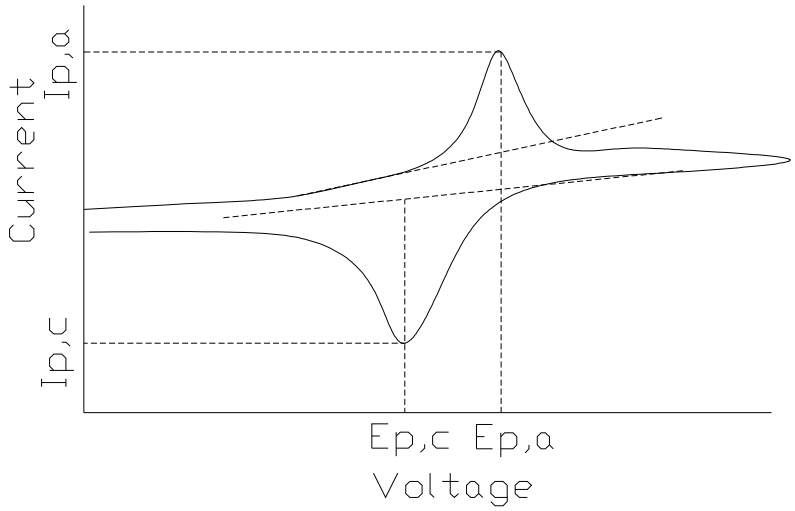

Figure 33. Current as a function of voltage for CV. Anodic and cathodic peaks are seen at voltages of Ep,a and Ep,c, respectively with currents of Ip,a and Ip,c, respectively [19].

Analysis of cyclic voltammograms data is achieved using the Randles-Sevcik equation, which can be applied only if the system is mostly reversible [20]. The electrochemical zssystem is considered reversible if $I_{p,a} \approx I_{p,c}$, $I_{p,c \text{ or } a} \sim \upsilon^{1/2}$, or if the peaks do not shift with υ [20]. Two of the three reversible characteristics are seen in typical data, so use of the Randles-Sevcik equation is valid. The Randles-Sevcik equation was discussed in the previous section on ASV, but it can be approximated as planar geometry for simplicity [21]:

$$I_p/\sqrt{\upsilon} = 0.446(nF)^{\left(\frac{3}{2}\right)}(RT)^{\left(-\frac{1}{2}\right)}C_{M^{n+}}D^{\left(\frac{1}{2}\right)}S$$

where I_p is peak current, ν is the sweep rate in V/s, n is the number of electrons transferred, F is the Faraday constant, R is the universal gas constant, T is the temperature in Kelvin, C is the concentration of the analyte in bulk solution in mol/m^3, D is the diffusion coefficient in m^2/s, and S is the electrode surface area in m^2. The difference between the cylindrical and planar forms of the Randles-Sevcik equation are negligible for small wires and rods, and it has been shown that for the electrode used in this work, the difference is empirically negligible.

The above equation can be used to determine either the reaction mechanism (number of electrons transferred) or the diffusion coefficient. When calculating one or the other, a literature value for n or D must be used. It is also possible to combine CV with the next section's chronopotentiometry to solve for both n and D simultaneously.

In addition, it is possible to compute the equilibrium potential using the anodic and cathodic peak voltages with cyclic voltammetry using the following equation:

$$E_{1/2} = \frac{E_{p,a} + E_{p,c}}{2}$$

where $E_{1/2}$ is the half-peak, or equilibrium potential, $E_{p,a}$ is the anodic peak voltage, and $E_{p,c}$ is the cathodic peak voltage. Plotting $E_{1/2}$ versus molar fraction of the analyte species yields a Nernstian slope of RT/nF and an intercept of E^0, the apparent standard potential.

4.1.2.3 Chronopotentiometry (CP)

Chronopotentiometry (CP) is another common technique used in the electrochemistry of molten salts. It, like ASV, consists of plating the analyte on the working electrode. However, for CP this process is a galvanostatic process, a constant-current process. The equilibrium current (i = 0A) is applied to the electrochemical cell, which forces a reduction reaction to occur. After the galvanostatic plating has occurred, the electrode will be at electrochemical equilibrium with the bulk electrolyte, and the only method of mass transport to the electrode is semi-infinite linear diffusion [22]. Once equilibrium is reached, a driving current is then applied. The driving current (i < 0A) is applied, which causes further reduction of the electroactive species in bulk electrolyte solution. At some point, all the oxidized ions in the immediate vicinity of the working electrode are reduced. The next electroactive species or the electrolyte, if there is no other electroactive species, is reduced to keep current flowing at the driving current [23]. When the transition from reducing one species to another (or the electrolyte) occurs, a sudden drop in potential happens. The time between the onset of driving current and the large potential change is called the 'transition time', τ, the time between a forced, constant-current equilibrium and the time when a state of complete concentration polarization occurs [22]. A graphical representation of chronopotentiometry is shown below in Figure 34 and Figure 35.

Figure 34. Galvanostatic current as a function of time for chronopotentiometry.

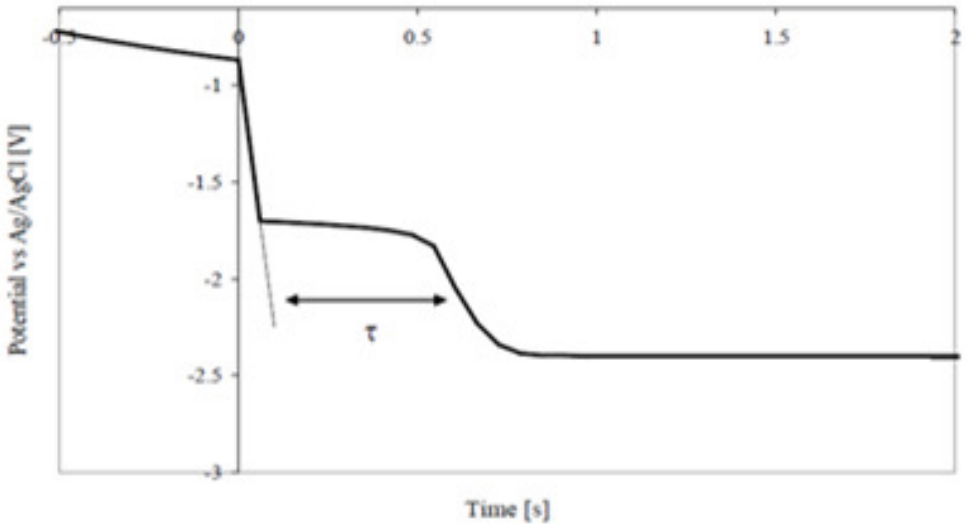

Figure 35. Typical chronopotentiogram of a Pu+LiCl+KCl salt from the literature [24].

Analysis of chronopotentiograms also requires that the system be reversible. Reversibility can be tested with chronopotentiometry by using multiple driving currents and plotting the graph of I vs. $\tau^{1/2}$. If the plot is linear, as shown in Figure 36, analysis of chronopotentiometry can commence using Sand's equation [24]:

$$i\sqrt{\tau} = \frac{nFC_{M^{n+}}A\sqrt{\pi D_{M^{n+}}}}{2} = \text{constant}$$

where i is the driving current, τ is the measured transition time, n is the number of electrons transferred, F is the Faraday constant, C is the concentration of ionic metal in solution, A is the surface area of the working electrode, and D is the diffusion constant of ionic metal in solution.

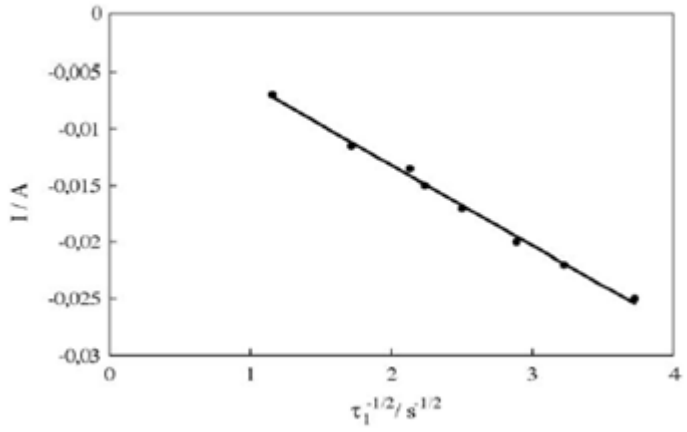

Figure 36. Linear dependence of I vs. √τ [24].

It is also possible to conduct chronopotentiometry on systems of two electroactive species simultaneously based on work by Berzins and Delahay via the following equation [25]:

$$(\tau_1 + \tau_2)^{\frac{1}{2}} - \tau_1^{\frac{1}{2}} = \frac{n_2 F \pi^{\frac{1}{2}} D_2^{\frac{1}{2}} C_2}{2i}$$

where 1 and 2 are the first and second electroactive species, respectively.

4.1.2.4 Open Circuit Potential Method (OCP)

One method of calculating the equilibrium potential involves the *in situ* electrodeposition of the analyte metal onto the working electrode and then measuring the resulting potential as a function of time [26, 27]. Once the electrodeposit has been created, the potential between the M|MCl-LiCl-KCl|AgCl-LiCl-KCl|Ag is measured as a function of time. An example of a usual resulting potentiogram is shown in Figure 37.

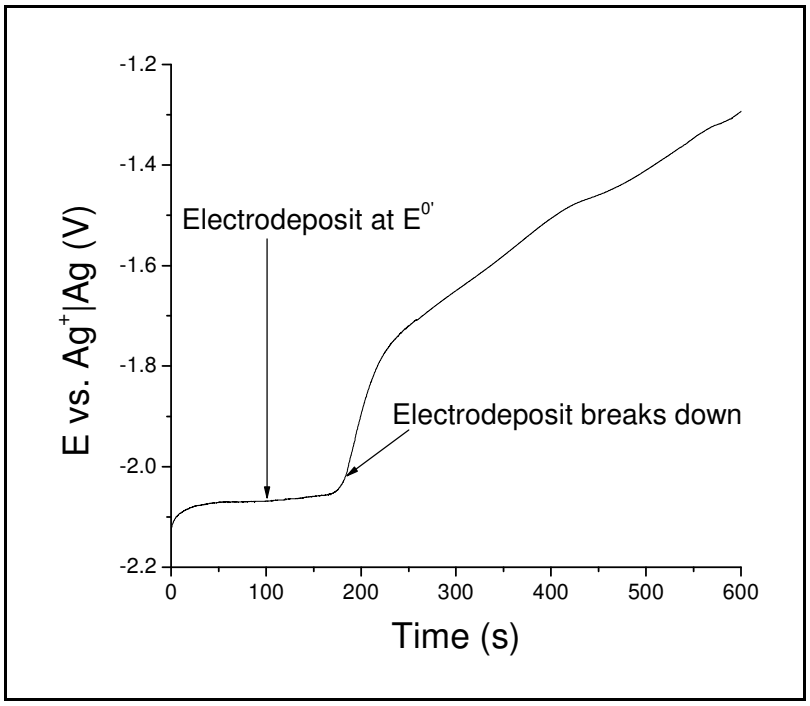

Figure 37. Measurement of the open circuit potential following an in situ electrodeposition of Nd from a ~0.8 wt% NdCl3 in LiCl-KCl solution at 500°C.

Since this method was found in the literature by the present author much later than CV, CP, and ASV and it was unable to be fully tested before being implemented, no data will be analyzed using the OCP technique, but it remains a viable and useful technique for future work in this area.

4.1.3 Analytical Techniques

Various analytical techniques were developed from information based in the literature, electrochemistry textbooks, and from previous experience with electrochemistry at the UW. Data was imported from the CorrView software into Microsoft Excel 2007 and 2010 and analyzed there using spreadsheets developed to organize the data. This data, once analyzed, was then consolidated into a larger database for comparison of the lanthanide elements in the LiCl-KCl eutectic salt.

4.1.3.1 Determination of Reaction Mechanism

The determination of the reduction/oxidation reaction mechanism (number of electrons transferred) is very important from the development perspective for an *in situ* electrochemical probe. A quick and easy way to determine the reaction mechanism can allow the operator to determine the number of electrons transferred of an unknown redox peak thereby providing information about the reaction. In a system with a well-studied redox reaction, the determination of a reaction mechanism experimentally can provide confidence that the system works as designed when it confirms reaction mechanism that is consistent with literature.

This work primarily uses cyclic voltammetry to confirm the redox reaction mechanisms of $LaCl_3$, $CeCl_3$, and $NdCl_3$ in a bulk LiCl-KCl eutectic salt. Using the Randles-Sevcik equation along with other known constants in the system, such as concentration, temperature, scan rate, and diffusion coefficient (determined from chronopotentiometry), the number of electrons transferred can be determined from a cyclic voltammogram. Cyclic voltammograms of 20, 50, 100, 150, and 200 mV/s were taken at each concentration and the number of electrons transferred was calculated from each voltammogram. The Randles-Sevcik equation, used for calculating the number of electrons, transferred is shown below:

$$n = \left(I_{p,c} \left[0.4463 \cdot S \cdot F \cdot C_{MCl_x} \cdot \sqrt{\frac{F \cdot D_{MCl_x} \cdot \nu}{RT}} \right]^{-1} \right)^{\frac{2}{3}}$$

where n is the number of electrons transferred, $I_{p,c}$ is the peak cathodic current, S is the wetted area of the working electrode, F is the Faraday constant, C_{MClx} is the bulk analyte concentration in molten LiCl-KCl eutectic, D_{MClx} is the diffusion coefficient of analyte in the electrolyte, ν is the scan rate, R is the ideal gas constant, and T is the operating temperature. Figure 38 (a) and (b) depict cyclic voltammograms from this work for a single-step and two-step redox reaction in liquid LiCl-KCl. The largest cathodic peak corresponds to a complete reduction to metal, while the largest anodic peak corresponds to the complete oxidation of the reduced metal to an ionic state. Figure 38 (b) also has a smaller set of peaks slightly more anodic than the stripping peak which corresponds to a soluble-soluble change in oxidation state, in this case $Nd^{3+} + e^- \leftrightarrow Nd^{2+}$.

Another way to determine the number of electrons transferred is to create a Nernst plot, a plot of equilibrium potential versus the natural logarithm of the molar fraction of the analyte solution. The slope of this plot should equal RT/nF, from which the reaction mechanism can be extracted. This method takes a great deal more time than simply using a quick cyclic voltammogram to determine/confirm the number of electrons transferred, but it may be more accurate in the case of single-step redox reactions. Redox reactions that occur in multiple steps are difficult to measure using the Nernst plots, so a cyclic voltammogram analysis of individual peaks may be more appropriate [26].

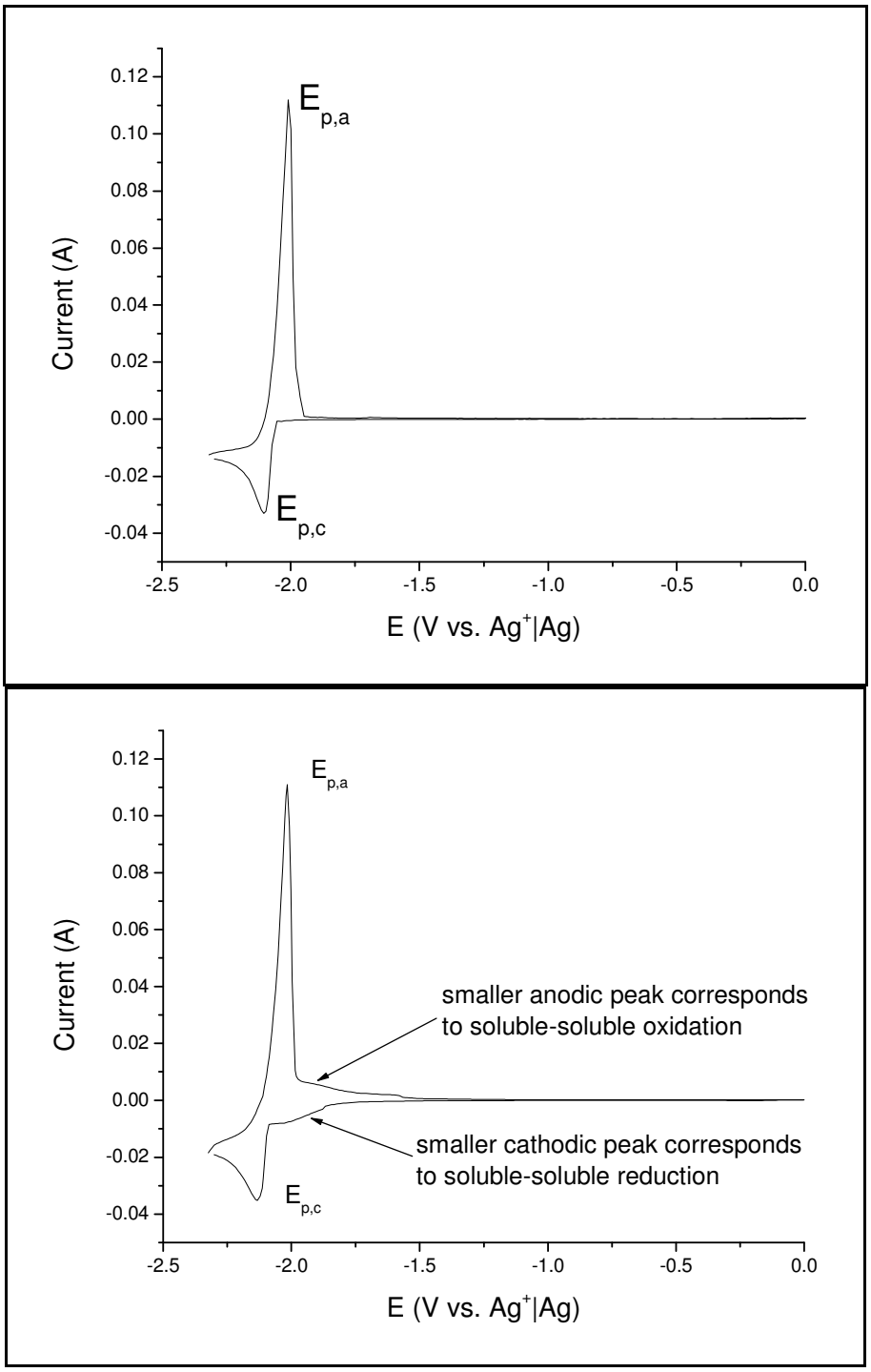

Figure 38. (a) single-step redox reaction of $Ce^{3+} + 3e^- \leftrightarrow Ce$ of 0.99 wt% (X = $2.27x10^{-3}$) $CeCl_3$ in LiCl-KCl at T=500°C. (b) two-step redox reaction of $Nd^{3+} + e^- \leftrightarrow Nd^{2+}$ and $Nd^{2+} + 2e^- \leftrightarrow Nd$ of 0.99 wt% (X = $2.23x10^{-3}$) $NdCl_3$ in LiCl-KCl at T=500°C.

4.1.3.2 Determination of Diffusion Coefficient of MCl_x in LiCl-KCl

Determination of the diffusion coefficient of an impurity in a bulk electrolyte solution is done typically through the use of the Sand equation as outlined in the chronopotentiometry section. Chronopotentiometric readings were taken with a 20 second constant-current plating time and a

subsequent 20 second galvanostatic reading at some driving currents, *i*. Multiple chronopotentiograms were taken at different driving currents to establish that the system was reversible and that the Sand equation was applicable. The currents chosen ranged from -0.001A to -0.4A based on the concentration of analyte in the bulk LiCl-KCl, and transition times, τ, were kept to under 5 seconds. Transition times greater than ~5 seconds, especially at high concentrations, seemed to be affected by a competing effect of re-oxidation of the reduced metal at the electrode/electrolyte interface.

Figure 39 shows actual data acquired in this work and shows the method of extracting transition time for any chronopotentiogram. In general, two potential plateaus are observed in a system in which a single electroactive species is dissolved in solution. The half-way point between these plateaus was determined and a horizontal line was drawn as shown in Figure 39. The capacitive current was then subtracted by extending the initial capacitive current with a straight line, as shown in Figure 39. The time lag between the intersection of the horizontal line and the chronopotentiogram less the capacitive current is the transition time, τ. Sometimes capacitive current did not appear, so in this case, the time at the intersection of the horizontal line and the chronopotentiogram is the transition time.

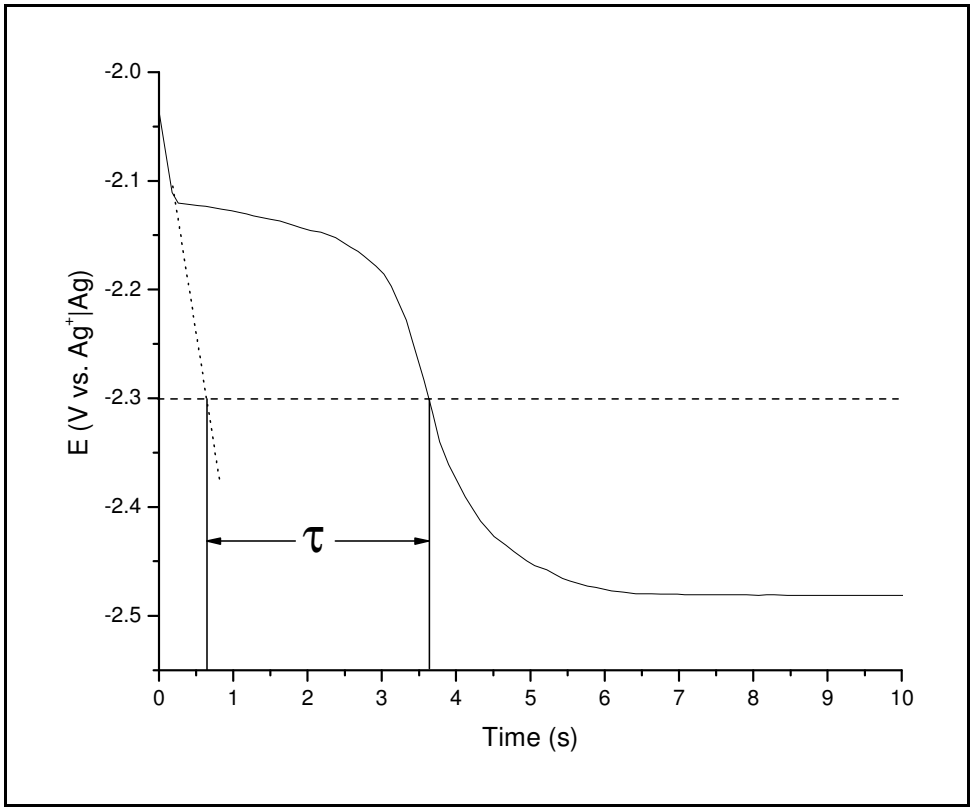

Figure 39. Typical chronopotentiogram for a single-step redox impurity in molten LiCl-KCl eutectic salt. I = 0A for 20 seconds followed by I = -0.03A for 20 seconds in 500°C LiCl-KCl eutectic with an added $X_{NdCl3}=2.33x10^{-3}$ (0.99 wt% $NdCl_3$).

Reversibility was verified at each concentration measured by taking five chronopotentiograms with differing driving currents and plotting *i* versus $\sqrt{\tau}$. When the linearity of this plot was confirmed, each chronopotentiogram was analyzed as explained previously and the extracted diffusion coefficients were then averaged to get an overall diffusion coefficient for the specific concentration.

The diffusion coefficient can also be extracted from the Randles-Sevcik equation from cyclic voltammetry if the number of electrons transferred, n, is known, although the literature has described chronopotentiometry to be the more accurate technique.

Since the present work deals with the development of an *in situ* electrochemical probe, it was decided that two separate techniques could be used to solve for the two unknowns in a voltammograms and potentiograms taken for known concentrations. First, the chronopotentiogram was analyzed as described above, and the diffusion coefficient was extracted. Next, the diffusion coefficient extracted via chronopotentiometry was input into the Randles-Sevcik equation, and the number of electrons transferred in the specific redox reaction was confirmed. This process could be iterative, but the reaction mechanisms for $LaCl_3$, $CeCl_3$, and $NdCl_3$ were widely known, so the first approximation of the diffusion coefficient was accurate.

4.1.3.3 Combined CV/CP Method

The ability to extract the reaction mechanism of an unknown electroactive species comes in the combination of two equations: the Randles-Sevcik equation and the Sand equation. Use of either one of these equations separately is useful when dealing with a known analyte, but use is difficult for a species of unknown reaction mechanism and diffusion coefficient. The following combination of equations allows for the calculation of reaction mechanism of an unknown analyte using a combination of cyclic voltammetry and chronopotentiometry [28].

$$Starting\ with:$$

$$Randles-Sevcik:\ \frac{I_p}{\sqrt{v}} = 0.446(nF)^{\left(\frac{3}{2}\right)}(RT)^{\left(-\frac{1}{2}\right)}C_{M^{n+}}D^{\left(\frac{1}{2}\right)}S$$

$$Sand:\ i\sqrt{\tau} = \frac{nFC_{M^{n+}}A\sqrt{\pi D_{M^{n+}}}}{2}$$

$$Eliminate\ D_{M^{n+}}\ through\ substitution:$$

$$n\ = \left(0.516302\left(\left(\frac{I_{p,c}}{\sqrt{v}}\right)\left(i\sqrt{\tau}\right)^{-1}\right)\right)^2$$

By combining both the Randles-Sevcik and Sand equations and eliminating D, the number of electrons transferred in an unknown redox reaction can be found. It follows that one could easily extract the diffusion coefficient using either the Randles-Sevcik or Sand equation in a second step by substituting in the number of electrons transferred.

4.1.3.4 Determination of the Apparent Standard Potential

The standard potential is defined as the potential at which the electrochemical cell is in reversible equilibrium with an analyte of concentration X=1.0 at 25°C at atmospheric pressure. This state cannot exist with a molten LiCl-KCl since the electrolyte and analyte will be solid at room temperature. Hence, it is common to extract an apparent standard potential based on extrapolations from the liquid state equilibrium potential readings.

Analysis of the Nernst equation for the half-cell reaction of $M^{3+} + 3e^- \leftrightarrow M$ shows the process of conducting a concentration study with the goal of extracting the apparent standard potential:

$$E_{MCl_x} = E^{0\prime}_{MCl_x} + \frac{RT}{nF}\ln X_{MCl_x} - E^0_{Ag(I)|Ag} + \frac{RT}{nF}\ln X_{AgCl}$$

where E_{MCl_x} refers to the measureable equilibrium potential, $E^{0\prime}_{MCl_x}$ is the apparent standard potential, X_{MCl_x} is the molar fraction of MCl_x in the electrolyte, $E^{0}_{Ag(I)|Ag}$ is the standard potential of the $Ag^{+}|Ag$ reference electrode, and X_{AgCl} is the molar fraction of the silver chloride in the liquid reference solution [27].

It was previously discussed that cyclic voltammetry could predict the equilibrium potential of a redox reaction by noting the half-way point between the anodic and cathodic peak potentials, or the mid-peak potential. For reversible systems, which this work deals with, the mid-peak potential does not shift significantly with scan rate, so for each set of cyclic voltammetry measurements, the mid-peak potential was taken and averaged to get an equilibrium potential for the specific concentration.

4.1.3.5 Determination of the Activity Coefficient of MCl_x in LiCl-KCl

Activity coefficient serves as a 'correction factor' to the idealized reaction. An activity coefficient of one would indicate that every chemical reaction that took place at a certain site, in this case the working electrode surface would react. Conversely, an activity coefficient greatly less than one indicates that complexation of the chemical compound has occurred during the chemical reaction and that the yield of a specific reaction is much less than ideally predicted. This coefficient has been measured for metal ions in liquid salts and liquid metals in literature, but there is usually variation in the data depending upon how the experiment was conducted. The following paragraphs describe the experimental extraction of activity coefficient performed in this work.

The apparent standard potential, also referred to as the formal potential, is defined as:

$$E^{0\prime}_{MCl_x} = E^{0}_{MCl_x} + \frac{RT}{nF}\ln\left(\gamma_{MCl_x}\right)$$

where $E^{0\prime}_{MCl_x}$ is the apparent standard potential, $E^{0}_{MCl_x}$ is the theoretical standard potential of the analyte in a liquid electrolyte at room temperature, and γ_{MCl_x} is the activity coefficient of the metal chloride in the given electrolyte solution [46]. Apparent standard potential depends on temperature and the activity coefficient only, so a measurement of E_{MCl_x} as a function of $\ln\left(X_{MCl_x}\right)$ will yield a plot with the apparent standard potential as the intercept.

The activity coefficient can be extracted from the Nernstian plot and by rearranging the equation for apparent standard potential as shown below:

$$\gamma_{MCl_x} = exp\left[\frac{\left(E^{0\prime}_{MCl_x} - E^{0}_{MCl_x}\right)nF}{RT}\right]$$

where $E^{0\prime}_{MCl_x}$ is the experimentally determined apparent standard potential. In order for the above equation to be completely true, the measured apparent standard potential must be on the chlorine reference scale because the activity coefficient is in control of the full-cell reaction as opposed to the half-cell reaction. Section 4.3.1 details the process in which the $Ag^{+}|Ag$ reference scale may be converted to the $Cl^{-}|Cl_2$ reference scale.

Once in the $Cl^{-}|Cl_2$ reference scale, the above equation can be written as:

$$\gamma_{MCl_x} = exp\left[\frac{\left(\Delta G^{0\prime}_{MCl_x} - \Delta G^{0}_{MCl_x,\ sc}\right)}{RT}\right]$$

where $\Delta G^{0'}_{MCl_x} = -nFE^{0'}_{MCl_x}$ and $\Delta G^{0}_{MCl_x,\ sc}$ is the standard state Gibb's free energy of the theoretical supercooled MCl_x-electrolyte in liquid state [46]. The supercooled free energy may be calculated from the thermodynamic crystal data of MCl_x, the enthalpy of fusion data, and the heat capacity data in the liquid phase [21].

While the supercooled state's free energy may be calculated for any energy, the values for the free energy of the supercooled states of $LaCl_3$, $CeCl_3$, and $NdCl_3$ were found in a paper by Castrillejo and coworkers [29]. The values were calculated for temperatures of 450°C and 550°C and were then linearly interpolated to 500°C knowing that Gibb's free energy is linearly proportional to temperature. These interpolated values are shown in Table VII.

Table VII. Gibb's free energy in the supercooled state for selected rare earth chlorides. Interpolated from [29].

MCl_x	$\Delta G^{0}_{MCl_x,\ sc}$ (kJ/mol)
$LaCl_3$	-854.87
$CeCl_3$	-850.22
$NdCl_3$	-840.85
$DyCl_3$	-794.61

4.1.3.6 Determination of Calibration/Working Curves with ASV and CV

A goal of this work was to develop a method to determine the concentration of rare earth elements in the LiCl-KCl melt at all times. It was decided that a measurement of peak height response as a function of rare earth chloride and rare earth ion concentration would provide calibration curves for the scientific basis of an *in situ* electrochemical probe which could be inserted into the electrorefiner to provide real-time measurements of lanthanide and fission product concentrations. As lanthanides and fission products build up in the electrorefiner salt during operation, the *in situ* electrochemical probe could be used to determine at which point the salt would need to be processed via ion exchange or disposed effectively disposed.

Three electrochemical peaks were measured and plotted as a function of rare earth chloride and rare earth ion concentration. The three electrochemical peaks measured were the ASV peak current, the CV's anodic peak current, and the CV's cathodic peak current. A constant scan rate of 50 mV/s was used because it was experimentally determined that this scan rate gave the best peak resolution to scan rate ratio without being too fast so as to overwhelm the data acquisition rate of the potentiostat used in this study.

4.2 Molten Salt Density

The density of a molten salt can be calculated using the experimental apparatus described in section 3.2 and the Archimedes' Principle which governs the buoyant forces acting on immersed bodies. The principle states that the upward or buoyant force acting on an immersed body is equal to the weight of fluid displaced by the body. In order to measure the density of the fluid, a bob of known mass and volume is attached to a balance via a thing wire. The buoyant force can then be calculated by measuring the difference in the mass of the bob at two states: immersed in the molten salt and in air at ambient temperature. This mass difference is then divided by the volume of the bob, as shown in below, to determine the density of the molten salt [30].

$$\rho = -\frac{(M_i - M_0)}{V_b\{1 + 3C(T - T_0)\}}$$

Where M_i and M_0 are the masses of the bob immersed in the salt and in air at ambient temperature (T_0) respectively. V_b is the volume of the bob at T_0, and C is the linear thermal expansion coefficient of the bob material. This equation accounts for the expansion of the volume of the bob in the molten salt at temperature T in degrees Celsius.

In order to calculate the density of the molten salt, an accurate measurement of the bob volume is needed. This is determined by immersing the bob in three fluids of known density: deionized water, acetone, and carbon tetrachloride. Literature data was used to determine the densities of the three fluids at the given ambient temperature [31], [32], [33]. The immersed weight of the bob was plotted versus the known density of the fluid as shown in Figure 40.The volume of the bob is equal to the slope of this plot. This calibration procedure was performed prior to each molten salt density measurement. Surface tension effects on the wire were determined to be negligible due to the very small diameter of the wire (0.02 mm). Bradshaw [30] showed that surface tension forces on the wire were negligible for a wire for a 0.2 mm diameter wire and a bob of similar weight.

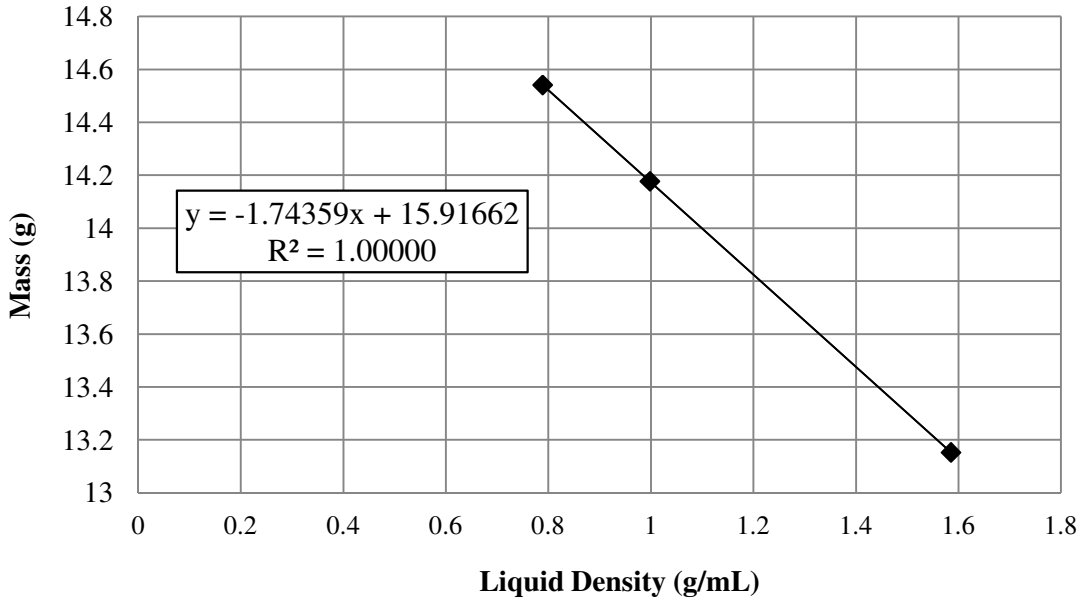

Figure 40. Nickel bob volume calibration curve.

The focus of this research is to measure the density of LiCl-KCl salt as a function of lanthanide chloride concentration. The theoretical density of an ideal multi-component fluid can be calculated in the following manner:

$$\frac{1}{\rho_{calc}} = \sum \left(\frac{w_i}{\rho_i}\right)$$

Where the overall fluid density, ρ_{calc}, can be determined from the sum of the ratio of the weight fraction of each component, w_i, to its pure density, ρ_i. So, for a mixture of LiCl-KCl eutectic and $LnCl_3$ (Ln=La, Nd, Ce) at 500°C, the formula becomes the following [38].

$$\frac{1}{\rho_{salt,\ calc}} = \frac{w_{LiCl}}{\rho_{LiCl,500°C}} + \frac{w_{KCl}}{\rho_{KCl,\ 500°C}} + \frac{w_{LnCl_3}}{\rho_{LnCl_3,\ 500°C}}$$

The densities at 500°C of lanthanide chlorides relevant to this research are listed in Table VIII. In addition, the parameters A, B, and C can be used to calculate the densities of the metal chlorides at any temperature according to the following equation.

$$\rho = kA + B(C + t)$$

Where A, B, and C are the parameters from Table VIII and t is the temperature in Celsius. Furthermore, Mariani and Vaden [34] applied a correction factor, k, to the densities of the metal chlorides. This correction factor accounts for non-ideal behavior of the metal chlorides in the salt. A k value of 1 implies ideal behavior. They applied a k value of 0.99973 to monovalent chlorides (LiCl and KCl) which they found to exhibit nearly ideal behavior. A k value of 0.82601 was applied to all trivalent chlorides. These values were determined by applying a correction factor to predicted data until it matched measured data from a LiCl-KCl-UCl_3 salt. The cause of this non-ideal behavior is thought to be the coordination chemistry of U^{3+}. If a solution exhibits ideal behavior, it is implied that the repulsive and attractive forces are negligible. This would be expected for a pure LiCl-KCl salt where the Cl^- ion would be equally attracted to both Li^+ and K^+ ions. However, when a trivalent chloride like UCl_3 is introduced into the mixture, the chlorine ions will bond more strongly to that ion, forming complexes such as UCl_6^{-3} which has a negative enthalpy of mixing due to the attractive forces [34].

Table VIII. Densities of selected metal chlorides [34].

Metal chloride	A	B	C	Density at 500°C (g/ml)
KCl	2.1359	-5.831E-04	273.15	1.6851
LiCl	1.8842	-4.328E-04	273.15	1.5496
$LaCl_3$	4.0895	7.774E-04	273.15	4.6905
$CeCl_3$	4.248	9.200E-04	273.15	4.9593
$NdCl_3$	5.0659	-1.522E-03	273.15	3.8891

Using these correction factors for the densities of the metal chlorides, Mariani and Vaden showed that they could accurately predict the density, and therefore the mass, of salt in the electrorefiner. This model will serve as a useful comparison for the experimental data obtained in this study. $LaCl_3$, $CeCl_3$, and $NdCl_3$ additions to LiCl-KCl will be investigated and it will be important to determine if they exhibit the same non-ideal behavior that Mariani and Vaden found UCl_3 to exhibit.

4.3 Differential Scanning Calorimetry

Differential Scanning Calorimetry (DSC) is a powerful thermoanalytical technique which can be used to measure a variety of physical properties of a sample. Most commonly, DSC is used to study thermal transitions as a function of time or temperature. The analysis is performed by measuring the energy required to keep a sample and an inert reference material at the same temperature while subjecting them both to identical heating or cooling programs. There are two types of DSC instruments: heat-flux

and power-compensation. A power-compensation DSC utilizes two separate and identical heaters for the sample and the reference. The sample and reference temperatures are measured and forced to be equal by adjusting the power input to the two furnaces. The difference in power input between the two furnaces can then be used to detect and analyze thermal transitions in the sample relative to the reference. Alternatively, the more common method of DSC, and method used for this research is heat-flux. In this method, both the sample and reference material are located in the same heater. The sample and reference pans both sit on a high conductivity heating block which ensures good heat transfer between the pans. In this case, thermal transitions in the sample cause the temperature of the sample to change relative to the reference. This small temperature difference is proportional to the heat transfer between the pans. This information is recorded and can be used to characterize the thermal transitions occurring in the sample [36]. Figure 41 shows schematics of both types of differential scanning calorimeters.

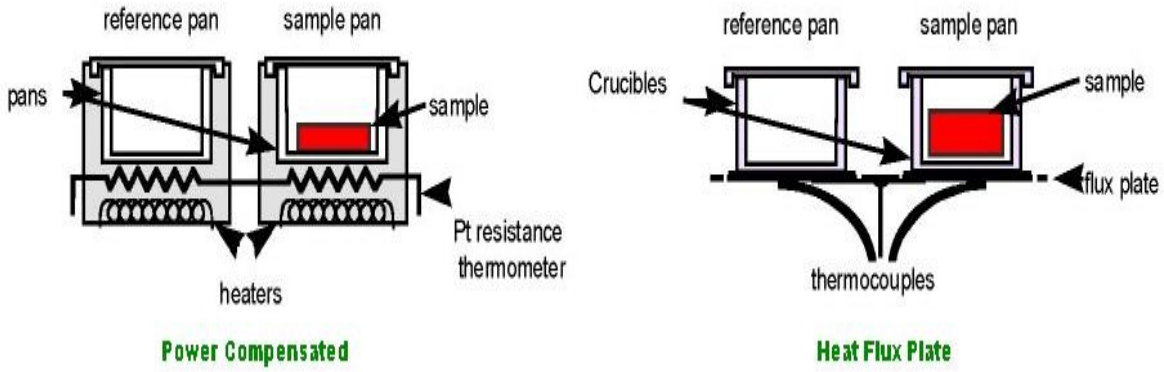

Figure 41. General schematics of power-compensated and heat flux differential scanning calorimeters [35].

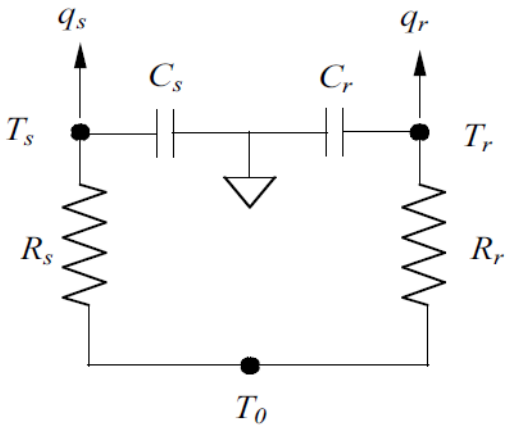

Figure 42. Circuit representation of heat flow measurement in the DSC [37].

Figure 42 is a circuit representation of the DSC heat flow measurement cell. T_s and T_r are the measured temperatures of the sample and reference calorimeters respectively, and T_0 is the temperature of the DSC enclosure. q_s and q_r are the sample and reference measured heat flows. C_s and C_r are the sample and reference calorimeter heat capacities and R_s and R_r are the sample and reference calorimeter resistances. Using this circuit model, heat balances can be written for the sample and reference calorimeters as follows [37]:

$$\dot{q_s} = \frac{T_0 - T_s}{R_s} - C_s \frac{dT_s}{dt}$$

$$\dot{q_r} = \frac{T_0 - T_r}{R_r} - C_r \frac{dT_r}{dt}$$

The difference between the sample and reference heat flows can then be written as shown below where $\Delta T = T_s - T_r$ and $\Delta T_0 = T_0 - T_s$.

$$\dot{q} = \frac{\Delta T}{R_r} + \Delta T_0 \left(\frac{1}{R_s} - \frac{1}{R_r}\right) + (C_r - C_s)\frac{dT_s}{dt} - C_r \frac{d\Delta T}{dt}$$

The first term on the right hand side of the above equation represents the conventional DSC heat flow. The second and third terms account for differences between the thermal resistances and heat capacities of the sample and reference calorimeters. Lastly, the fourth term quantifies the difference in the heating rates of the two calorimeters. Accounting for the differences between the sample and reference calorimeters is a relatively new practice which significantly increases the accuracy of the DSC measurements. The baseline response, reproducibility, and heat flow resolution are dramatically improved [37].

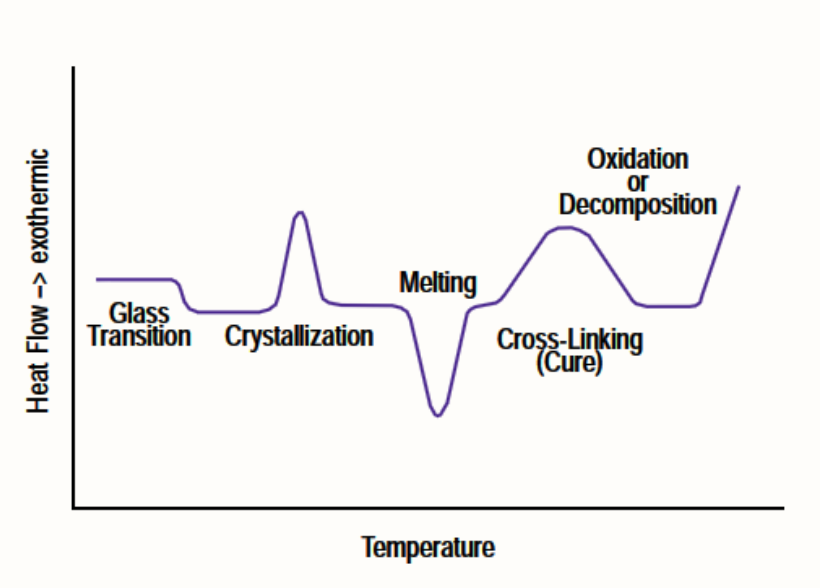

Figure 43. General DSC scan showing the typical shapes of common thermal transitions [38].

When an endothermic reaction occurs in the sample (e.g. melting), the sample temperature will lag behind the reference temperature, heat will be transferred to the sample, and an endothermic peak will be observed. On the other hand, an exothermic reaction (e.g. crystallization) will cause heat to be transferred away from the sample and an exothermic peak will be observed in the opposite direction of the endothermic peak. Figure 43 shows the general shapes of common thermal transitions observed in DSC analysis. It is also important to be able to differentiate between true thermal transition signals and spurious artifacts on the DSC scans. Figure 44 shows common artifacts observed in DSC analysis. Artifact (a) represents sample movement in the DSC pan. All of the (b) signals are the result of a change in the heat transfer between the DSC pan and the sensor. (b1), (b2), and (b3) represent sample pan distortion, pan movement in furnace, and a mechanical shock to the bench respectively. If an ingress of cool air into the measurement cell occurs, a noisy signal similar to (c) will appear. The (d1) and (d2) artifacts are the result of miscellaneous electrical effects. (e) is the result of atmospheric changes such as the room temperature increasing and (f) is caused by the bursting of the sample pan. (g) is caused by the periodic opening and closing of the hole in the lid of the sample pan often due to condensation. Lastly, (h) is the result of contamination of the cell from a previous sample [39].

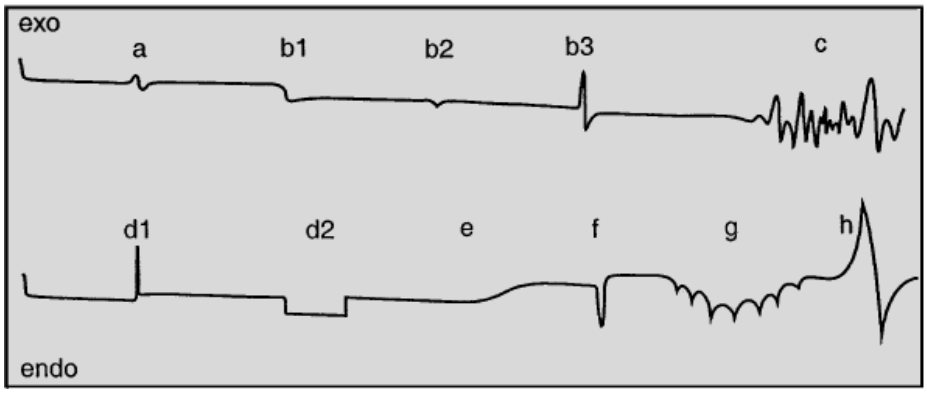

Figure 44. Various spurious signals commonly observed with DSC. A description of each artifact is given in the text above [39].

This research will be mostly concerned with the endothermic melting peaks. The size of shape of a melting curve can vary dramatically depending on the composition of the sample. Figure 45 shows DSC melting curves for samples of various different compositions. Pure substances will exhibit a very sharp, well-defined endothermic peak as shown in sample (a) of Figure 45. In this case, the low temperature side of the peak is nearly linear and the melting point can simply be defined at the temperature where the heat flow first begins to deviate from the baseline measurement at the base of the peak on the low temperature side. This is known as the onset temperature. For less pure samples with slightly more broad melting peaks, an extrapolated onset temperature can be used to define the melting point. As shown in Figure 46, the extrapolated onset temperature is defined as the intersection of a line extrapolated from the baseline heat flow and a line tangent to the most linear portion of the low temperature side of the melting peak. For significantly broad peaks, the peak temperature may serve as a more accurate way to characterize the transition. In Figure 46, the lower temperature peak has an extrapolated onset temperature of 351.72°C and a peak temperature of 353.23°C. The higher temperature peak has an extrapolated onset temperature of 438°C and a peak temperature of 448.13°C.

For this research, mixtures LiCl-KCl eutectic and rare earth chlorides will be studied with DSC. Sample (b) in Figure 45 shows the melting processes of a sample containing a eutectic impurity. In this

case, there are two clear peaks. The first peak is the eutectic peak whose size will vary depending on the amount of eutectic in the sample. The second peak at higher temperature is the main melting peak.

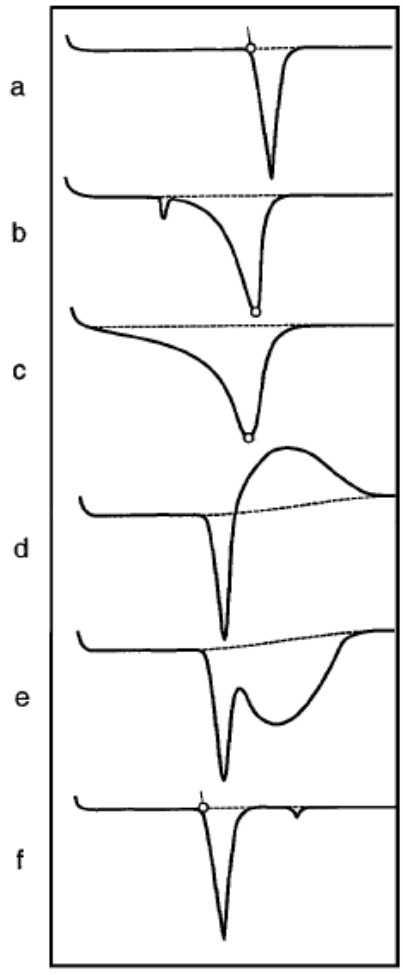

Figure 45. Various melting processes: a: a nonpolymeric pure substance; b: a sample with eutectic impurity; c: a partially crystalline polymer; d and e: melting with decomposition; f: a liquid crystal [39].

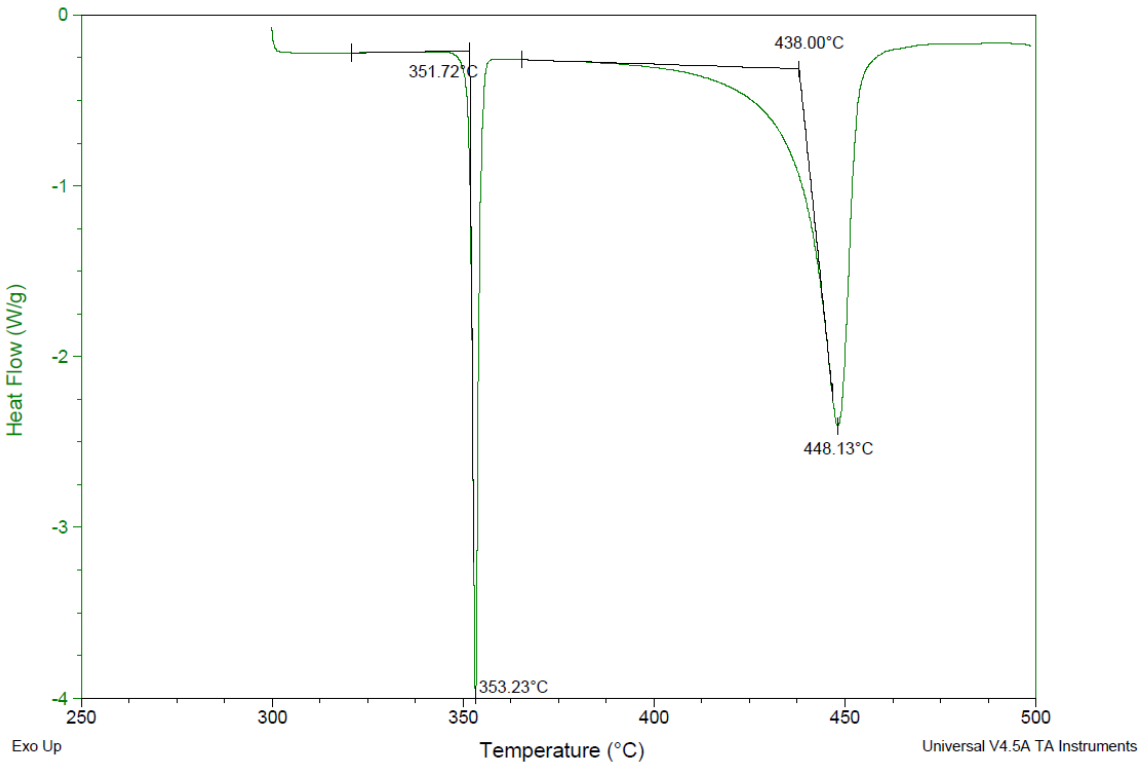

Figure 46. Example DSC curves showing the peak and extrapolated onset temperatures.

Several other parameters have an effect on the shape of the DSC scan. Most important for this research are the DSC temperature scan rate and the sample mass. The effect of scan rate is shown in Figure 47. Increasing the temperature scan rate will increase the sensitivity of the heat flow measurement, so a peak which is clearly visible at a high scan rate may be barely discernible at a low scan rate. This can be seen in Figure 47 by comparing the $0.5°min^{-1}$ and $16°min^{-1}$ curves. The first peak is clearly visible in the higher scan rate, yet just appears as a small bump at the lower scan rate. In addition to causing an increase in sensitivity, faster scan rates also decrease resolution. This effect can best be observed by comparing the $16°min^{-1}$ and $64°min^{-1}$ curves in Figure 47. While two peaks are clearly visible at $16°min^{-1}$, only one peak can be resolved at $64°min^{-1}$. So, scan rate causes competing effects on the sensitivity and resolution which must be balanced to achieve the most accurate results. For this research, it has been found that a scan rate of $10°min^{-1}$ is fast enough to see most transitions, yet slow enough to resolve necessary peaks.

Scan rate can also have an effect on the onset temperature of certain transitions. Many transitions such as evaporation, crystallization, and decompositions are kinetic so they will shifter to higher temperatures as the heating rate is increased. However, melting point is generally not very sensitive to this effect. So, relatively low heating rates should be used to detect the true temperatures at which thermal transitions occur [40].

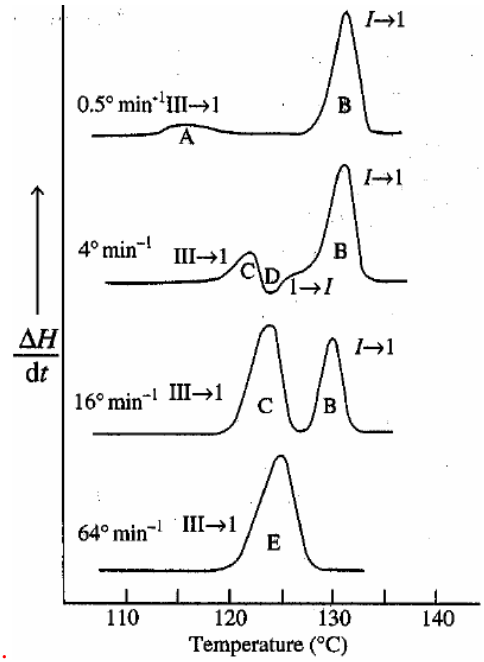

Figure 47. Effect of temperature scan rate on DSC sensitivity and resolution [41].

The mass of the DSC sample also has an effect on the heat flow measurement. Using small sample masses will achieve high resolution but poor sensitivity. On the other hand, larger samples increase sensitivity but can also cause thermal lag due to the heat transfer between the bulk material and the sensor. The energy required to cause an endothermic reaction such as melting is proportional to the sample mass. So, if a sample is too large, there will be a thermal lag and the thermal transition peaks will be shifted from their true values. Good contact between the sample and the bottom of the sample pans ensures good heat transfer and reduces the thermal lag effect [41]. Also, samples should be large enough that they are an accurate representation of the bulk material that they are taken from. This is especially important multi-component materials. Ultimately, samples between of less than 10 milligrams were found to produce good results.

The temperature calibration of the system was performed by measuring the melting point of a high purity metal with a well known melting point. Indium was used in this case. High purity metals are used because they have very sharp endothermic peaks for which the onset temperature can very easily and accurately be defined. The measured value of the onset temperature can then be matched to the known literature value in order to calibrate the system. In addition, when analyzing DSC heat flow measurements, it necessary to perform a correction for the baseline heat flow. Every DSC, when operated empty, will read a non-zero heat flow. This is the result of the small differences in the thermal resistances and heat capacities of the sample and reference calorimeters. This baseline signal must be subtracted from the DSC signal of the sample [37].

4.3.1 Phase Diagrams

Differential scnanning calorimetry can be used to construct phase diagrams which are temperature vs. composition plots at a constant pressure. For this research, the pseudo-binary system of LiCl-KCl eutectic and lanthanide trtichloride ($LnCl_3$: Ln= La, Ce, Nd) is of interest. The amount of LiCl-KCl will remain fixed and the $LnCl_3$ concentration will be varied up to approximately 25 mol%. In order to construct a phase diagram, many DSC samples are created with various compositions spanning the

desired range of the phase diagram. For example, in this study LiCl-KCl-$LnCl_3$ samples were made with varied $LnCl_3$ concentration from 0-25 mol% in 2 mol% increments. Then, DSC scans are performed for each sample over the desired temperature range of the phase diagram. Then, the temperature (onset or peak) of each distinct thermal transition is noted. The thermal transition temperatures for all the compositions are plotted together and the points defining thermal transitions can be connected with lines to define various phase regions. An example of this technique is shown in Figure 48 which displays a hypothetical phase diagram and the hypothetical DSC curves used to construct the phase diagram. Curves (a) and (g) represent the melting of samples of pure A and B respectively. Curve (d) shows the melting of a sample at the eutectic composition of A and B. In this case, there is only one peak (d1) on the DSC curve representing the eutectic invariant reaction where the liquid solidifies into a solid solution of the same composition at asingle temperature. Points a2, b3, c2, d1, e3, f3, and g1 form the liquidus line of the system which is defined as the point at which the last solid has melted upon heating. In addition, the solidus line is defined as the point at which melting first occurs upon heating.

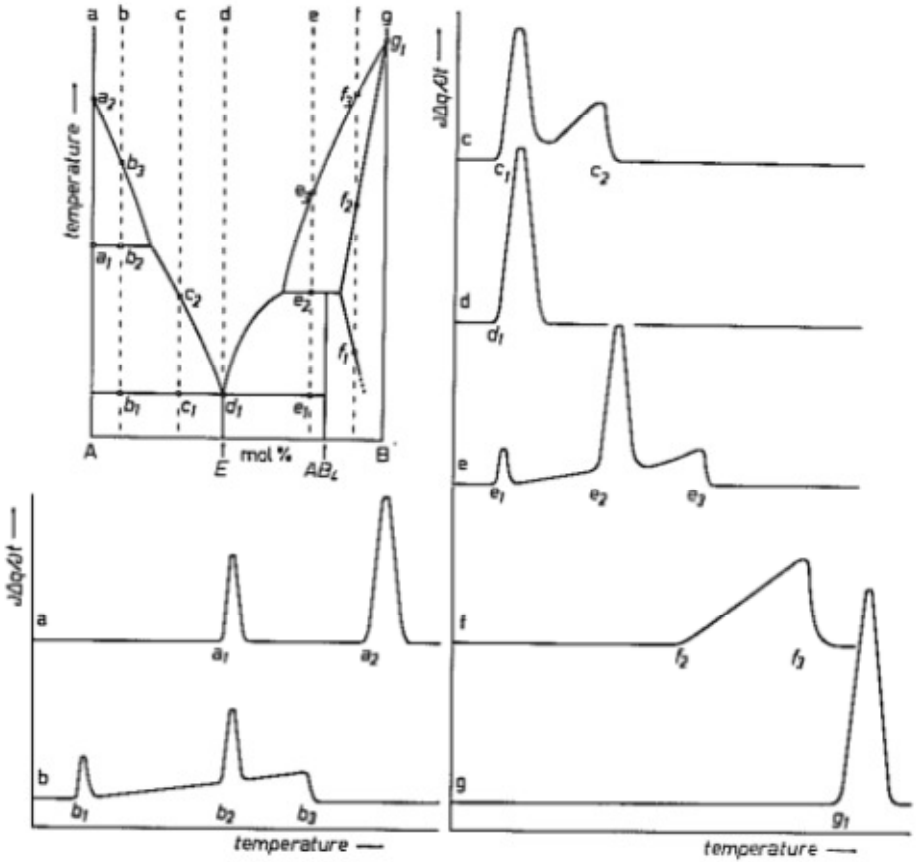

Figure 48. Hypothetical phase diagram and DSC scans used to construct the phase diagram [40]**.**

5. Experimental Results

Over the course of this project, a large amount of data has been collected investigating the electrochemical properties of LiCl-KCl salt containing various concentrations of rare-earth chlorides. In

addition, the density and melting point of the salt has been measured as a function of rare earth concentration. This section summarizes results obtained in all of these areas over the past three years.

5.1 Electrochemistry of rare-earth chlorides

Electrochemical studies of $LaCl_3$, $CeCl_3$, $NdCl_3$, and $DyCl_3$ have been completed. Rare earth chloride concentrations of approximately 0.05 wt% up to 10 wt% (500 – 100000 ppm) were examined. Various concentration-dependent effects have been observed that have not been previously reported in literature. These effects were expected but, so far, have been undocumented in the literature, since most electrochemical studies are concerned with only the electrochemical aspect, but not the use of the electrochemistry for an engineering, non-steady state system. For the electrorefiner, the concentration of fission products and lanthanides changes with each fuel batch added to the same LiCl-KCl, so these effects are important to the full understanding of the electrorefining salt.

Throughout the course of the studies with the three lanthanides, hundreds of ASV's, CV's, and CP's were taken along with a handful of open circuit equilibrium potential measurements and many couloamperometric measurements to study the electrodeposition behavior. Many interesting plots have been created, such as the calibration curves, Nernstian plots, and diffusion coefficient as a function of concentration. All experiments in this section were conducted at 500±1°C.

5.1.1 Lanthanum (III) Chloride in LiCl-KCl

The electrochemical reversibility of the lanthanum redox reaction was confirmed using cyclic voltammetry. Figure 49 shows typical cyclic voltammograms with the expected trends which were consistent for cyclic voltammograms for all concentrations investigated in this research. The reversibility of the redox reaction can be confirmed by plotting the anodic and cathodic peak currents as a function of the square root of the scan rate. In such a plot a linear relationship between the peak currents vs. square root of the scan rate establishes reversibility. This relationship can be seen in Figure 50.

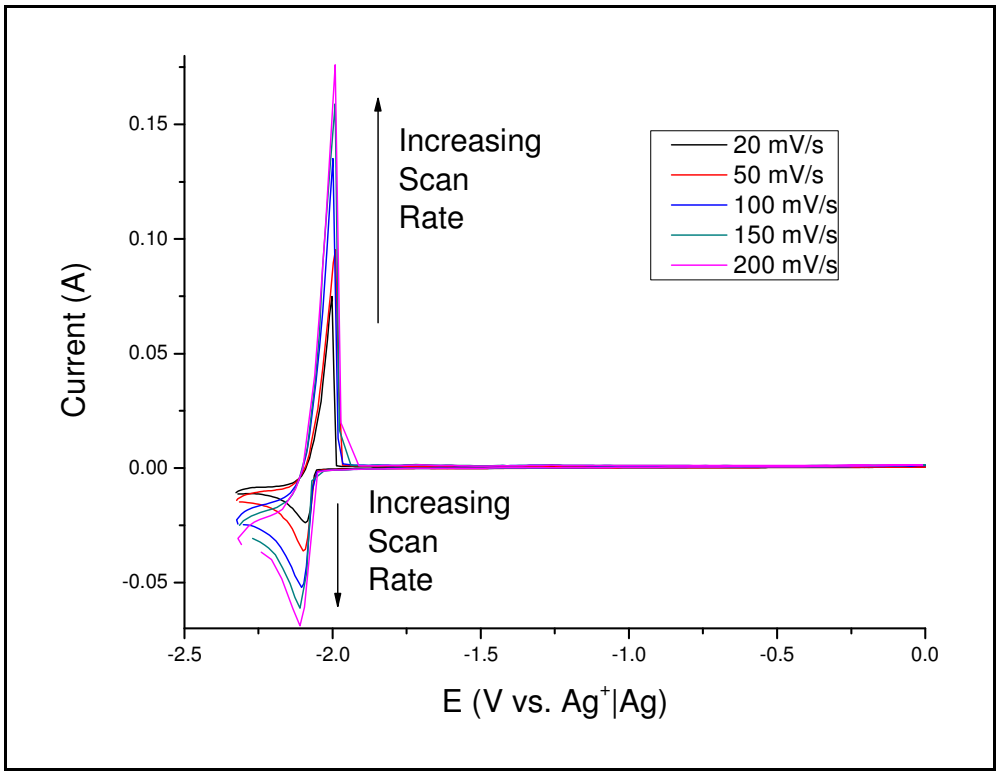

Figure 49. Cyclic voltammograms of 0.99 wt% $LaCl_3$ (X_{LaCl3} =2.27x10^{-3}) in LiCl-KCl with scan rates: 20, 50, 100, 150, and 200 mV/s. A single, large peak is observed with the anodic peak being slightly larger and steeper than the cathodic peak, which is typical of a soluble-insoluble transition. As expected, peaks increase in magnitude with the scan rate.

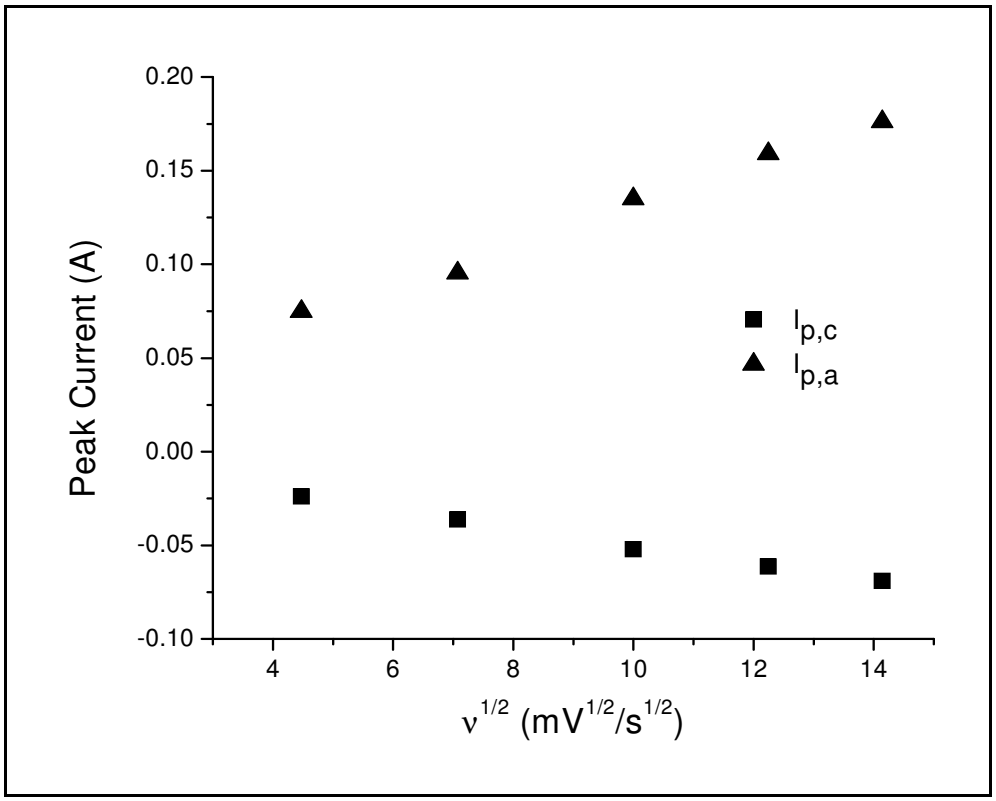

Figure 50. Peak cathodic and anodic current as a function of $\nu^{1/2}$. Linearity of this relationship is a characteristic of an electrochemically reversible reaction. Data from $LaCl_3$-LiCl-KCl with $LaCl_3$ concentration of 0.99 wt% ($X_{LaCl3} = 2.27x10^{-3}$).

The lanthanum redox reaction was confirmed to be La(III) → La(0) + $3e^-$ using cyclic voltammetry at all $LaCl_3$ concentrations. The electrochemical reaction was also confirmed independently using a combined chronopotentiometric and cyclic voltammetry approach, the average electrons transferred using this method was n=2.911, which can be rounded to 3 since n must be an integer value.

Additionally, the diffusion coefficient of lanthanum in the pyroprocessing salt was determined using chronopotentiometry and Sand's equation. Figure 51 shows how diffusion coefficient changes as a function of concentration. The exact mechanism underlying the change in diffusion coefficient as a function of analyte concentration is being investigated.

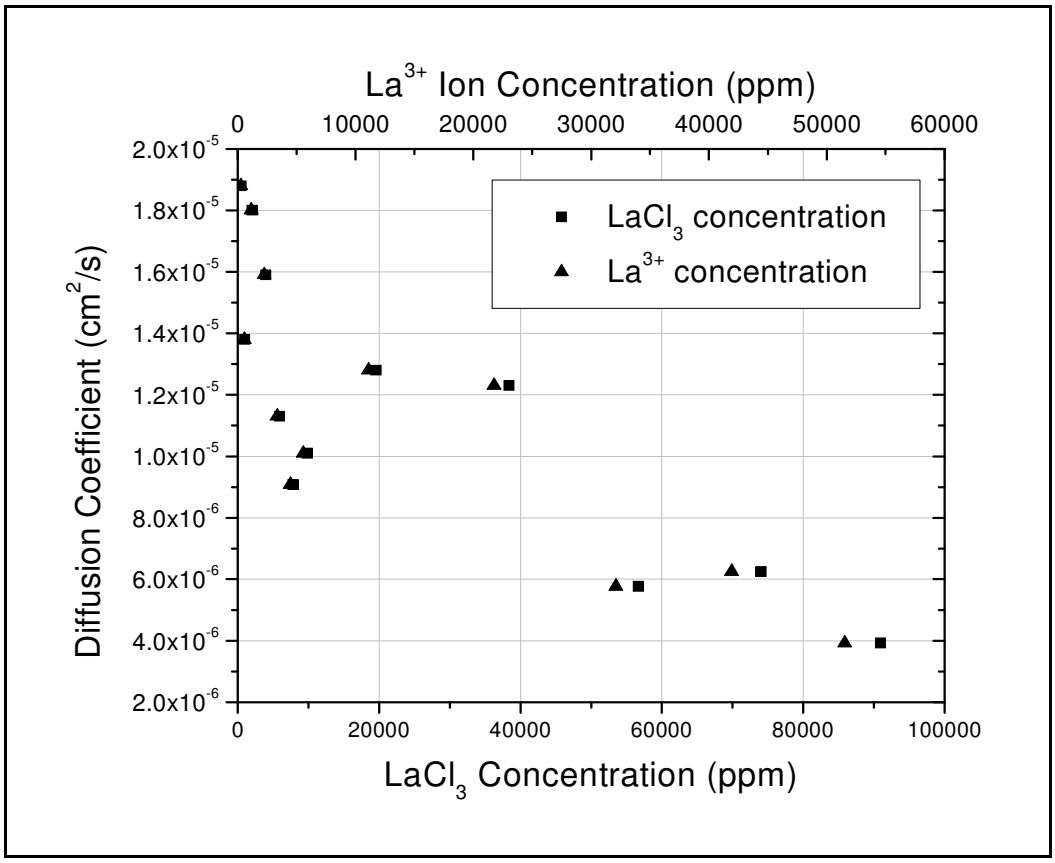

Figure 51. Diffusion coefficient of lanthanide metal ions in LiCl-KCl at 500°C over a large range of concentrations of both $LaCl_3$ and La^{3+} ion concentration. Note the dependence of diffusion coefficient on analyte concentration.

Furthermore, the apparent standard potential of lanthanum at 500°C was calculated using a Nernst plot. Figure 52 shows the Nernst plot used to find the apparent standard potential. While some scatter is observed at higher concentrations, a majority of the lower concentrations yield reasonably good linear plots. From Figure 6, the intercept is the apparent standard potential, $E^{0'}$ = -1.9593V vs. $Ag^{+}|Ag$ reference scale ($E^{0'}$ = -3.11V vs. $Cl^{-}|Cl_2$).

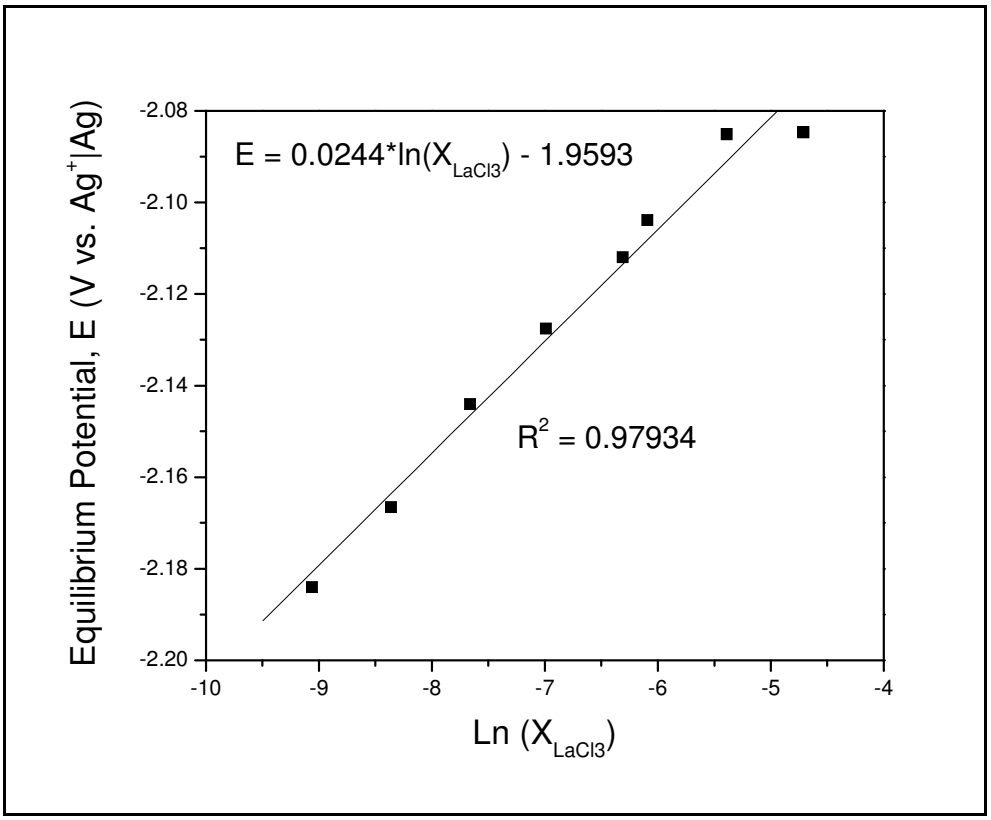

Figure 52. Nernst plot of the $LaCl_3$-LiCl-KCl concentration study. The slope of this plot should be equal to RT/nF, and the intercept is the apparent standard potential versus the 5 mol% $Ag^+|Ag$ reference electrode.

Lastly, ASV was used to determine peak current density as a function of lanthanum concentration. This data, shown in Figure 53, can be used as the fundamental basis for an electrochemical *in situ* probe to determine $LaCl_3$ concentration in real pyroprocessing salt. This ASV working curve starts out with a somewhat exponential increase at low concentrations, continues into a linear regime up to approximately 10000 ppm $LaCl_3$, and then proceeds to enter into a quasi-logarithmic response at higher concentrations (> 10000 ppm $LaCl_3$). A possible explanation to this trend is based on the effects on the working electrode's surface. At low concentrations, there is not enough analyte in solution to fully utilize the surface area of the electrode, at medium concentrations the analyte is at sufficient concentration to coat the working electrode in single, ordered layers during the plating step, and at high concentrations the concentration of analyte in solution is so great that surface saturation effects are noticed.

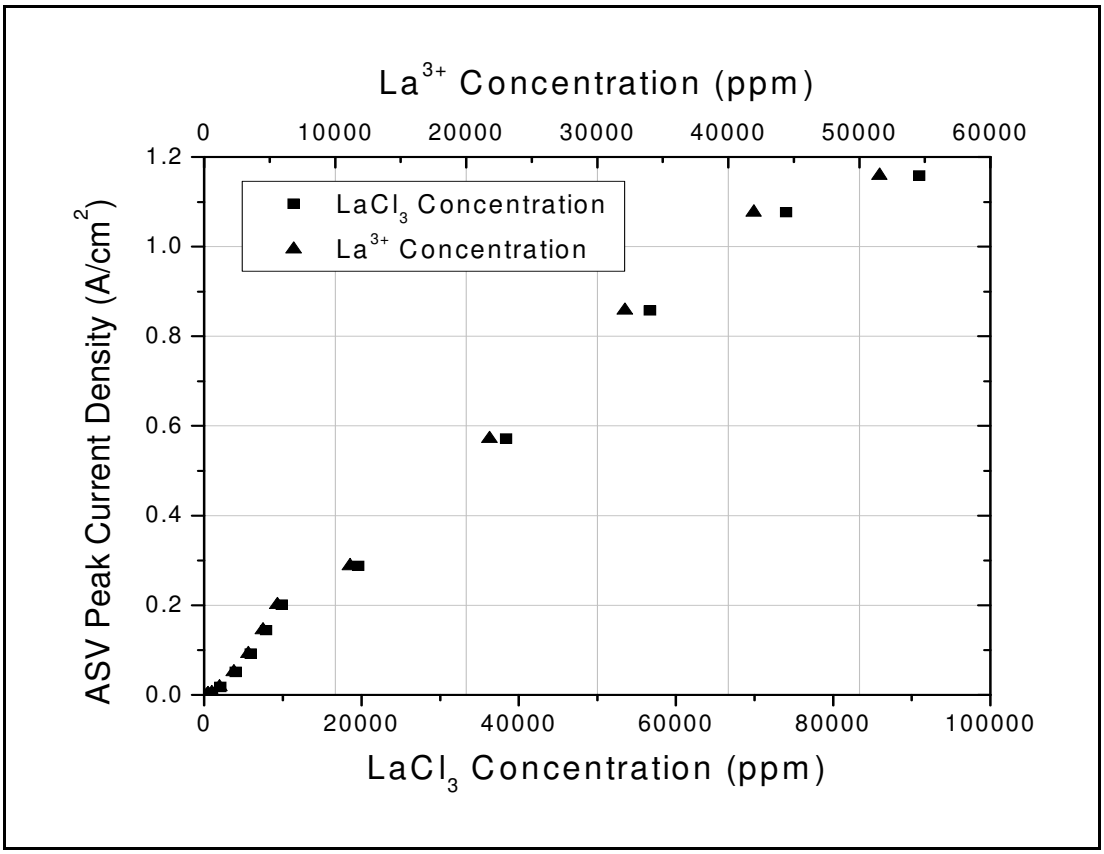

Figure 53. ASV calibration curve relating peak current density from an ASV (plating time = 60 sec., scan rate = 50 mV/s, ΔE = -2.4V – 0V) to lanthanum chloride and lanthanum ion concentration in LiCl-KCl.

5.1.2 Cerium (III) Chloride in LiCl-KCl

$CeCl_3$ demonstrated similar concentration-dependent effects as $LaCl_3$. Early in working with $CeCl_3$, it was determined that the same parameters used in the electrochemical measurements for $LaCl_3$ could be used for all the $CeCl_3$ measurements due to its chemical and electrochemical similarities to $LaCl_3$. Like $LaCl_3$, $CeCl_3$ cyclic voltammograms exhibited large, single-step reduction and oxidation peaks such that a full reduction and oxidation of Ce^{n+} to Ce metal could be expected. Figure 54 shows the typical response of $CeCl_3$ in LiCl-KCl eutectic salt for scan rates of 20, 50, 100, 150, and 200 mV/s. Analysis of these cyclic voltammograms confirmed that both the anodic and cathodic peak currents were linearly proportional to the square root of the scan rate (Figure 55), and the mid-peak potential did not shift with scan rate (Figure 56). These relationships were true for all concentrations measured in this study, and they confirm the reversibility of the cerium redox reaction and the applicability of the Randles-Sevcik equation. Thus, The Randles-Sevcik equation was applied, and the reaction mechanism was determined to be a single-step transfer of n = 3 electrons. Hence, the full redox reaction for $CeCl_3$ in LiCl-KCl eutectic salt is:

$$\text{Cerium half} - \text{cell: } Ce^{3+}_{(aq)} + 3e^- \leftrightarrow Ce_{(s)}$$

$$\text{Chlorine half} - \text{cell: } \frac{3}{2}Cl_{2(g)} + 3e^- \leftrightarrow 3Cl^-_{(aq)}$$

$$\text{Full reaction: } Ce^{3+}_{(aq)} + 3Cl^-_{(aq)} \leftrightarrow \frac{3}{2}Cl_{2(g)} + Ce_{(s)}$$

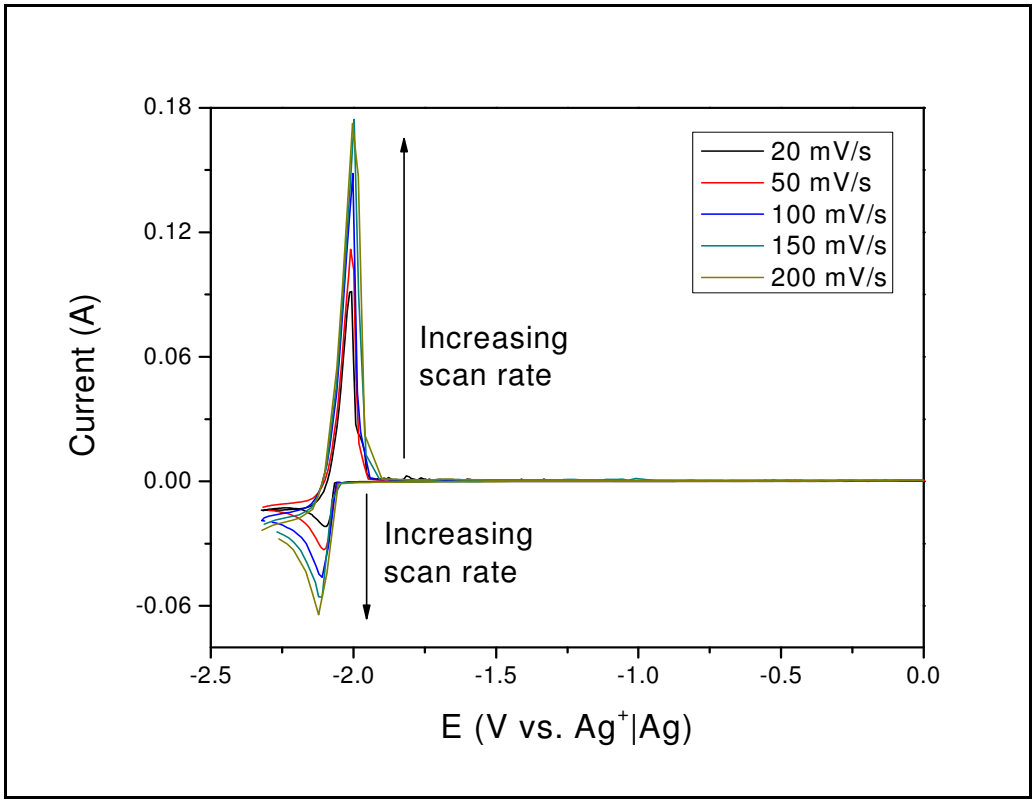

Figure 54. Cyclic voltammograms of $CeCl_3$ at 0.99 wt% ($X_{CeCl3} = 2.27x10^{-3}$) in LiCl-KCl.

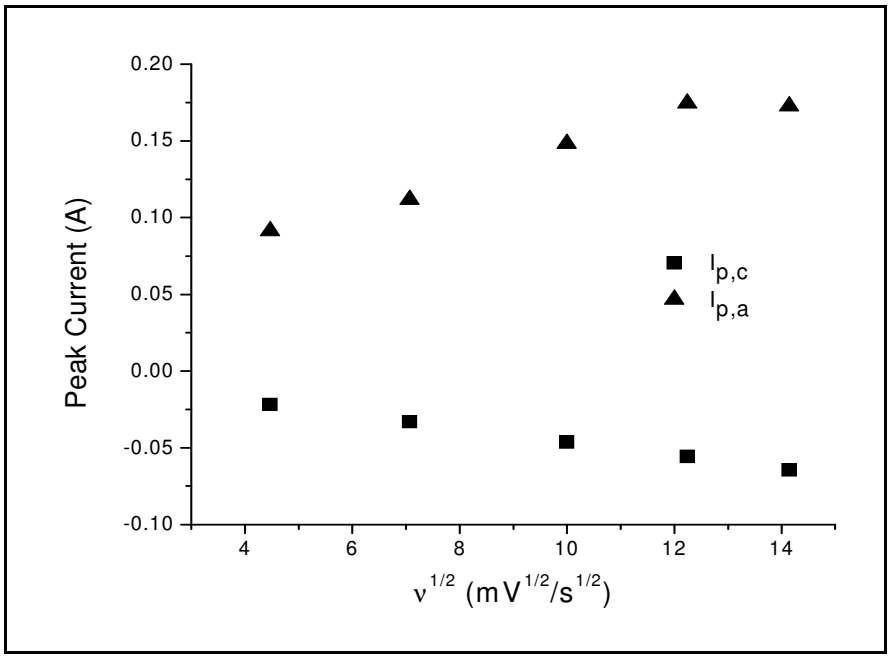

Figure 55. Peak cathodic and anodic current as a function of $\nu^{1/2}$. Data from $CeCl_3$-LiCl-KCl with $CeCl_3$ concentration of 0.99 wt% ($X_{CeCl3} = 2.27x10^{-3}$).

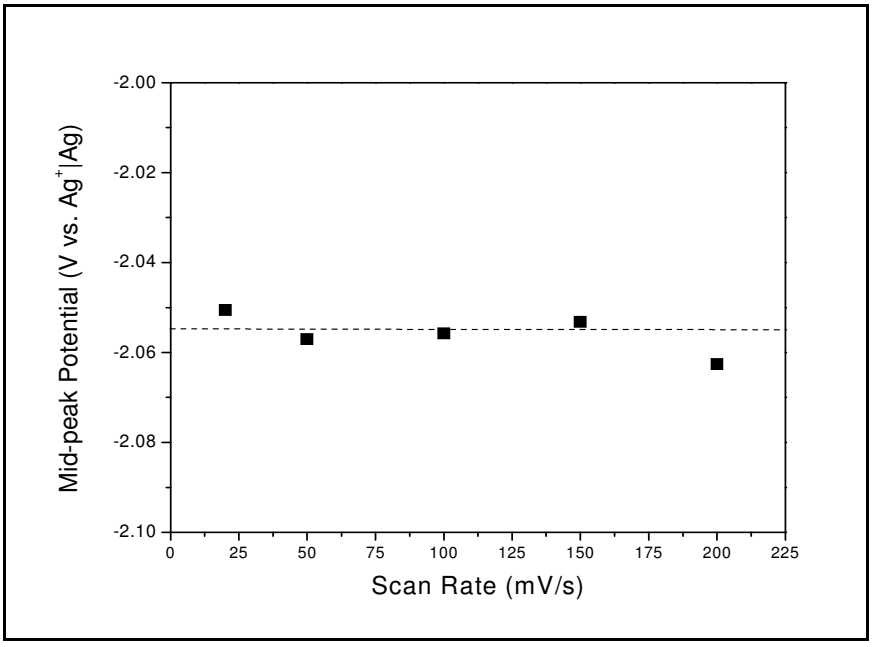

Figure 56. Mid-peak potential as a function of scan rate. Data from $CeCl_3$-LiCl-KCl with $CeCl_3$ concentration of 0.99 wt% ($X_{CeCl3} = 2.27x10^{-3}$). The dashed line represents the average mid-peak potential for 0.99 wt% $CeCl_3$.

Diffusion coefficients of cerium ions in LiCl-KCl behaved similarly to the lanthanum ions in that they were somewhat inversely dependent upon the concentration of the analyte in the melt. Figure 57 shows the diffusion coefficient, as calculated by chronopotentiometry data, as a function of $CeCl_3$ concentration and Ce^{3+} ion concentration.

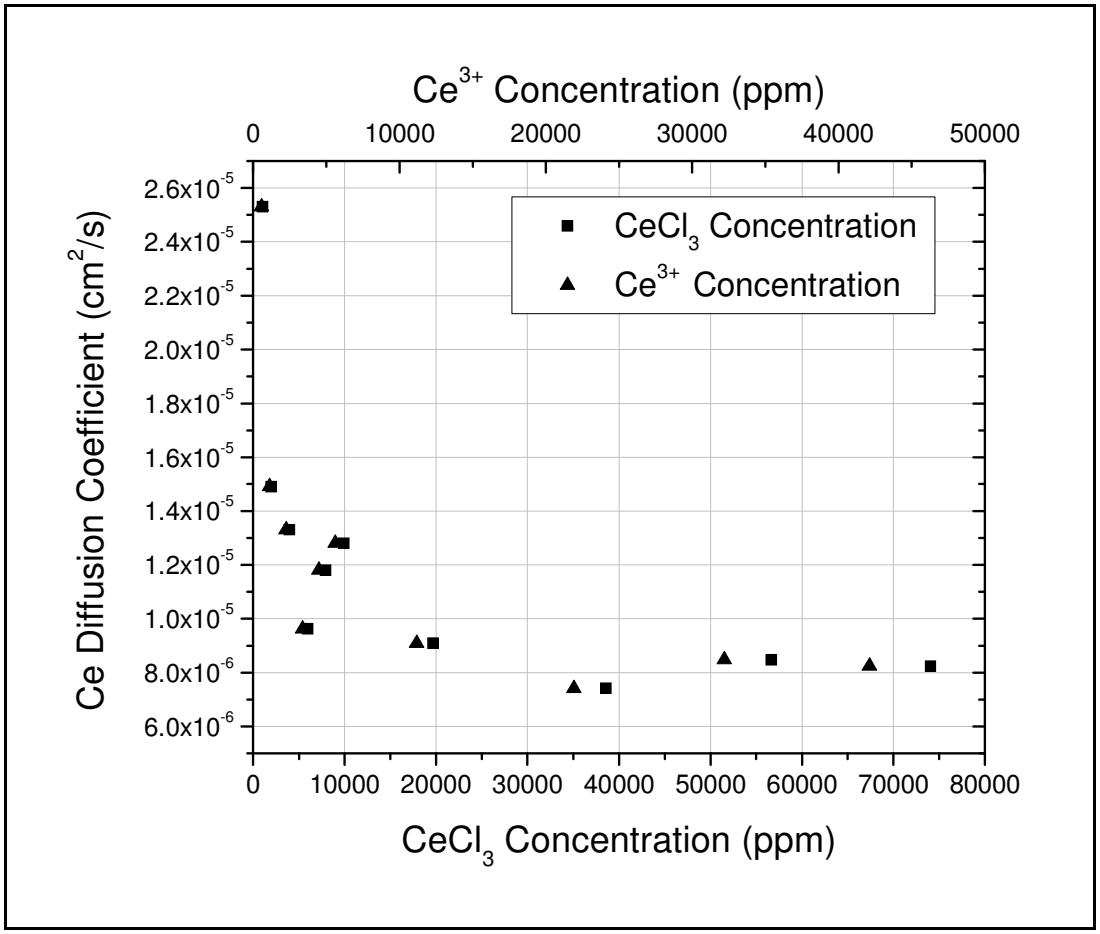

Figure 57. Ce metal ion diffusion coefficient as a function of analyte concentration.

Since Ce^{3+} goes through the same single-step, three electron transfer redox reaction as La^{3+}, the same methods were used in creation of a Nernst plot, Figure 58, for extraction of the Ce apparent standard potential. Operational procedure of the electrochemistry system had been fine-tuned for the $CeCl_3$ concentration study, so good data was attained with respect to the equilibrium potential measurements throughout the entirety of the concentration study.

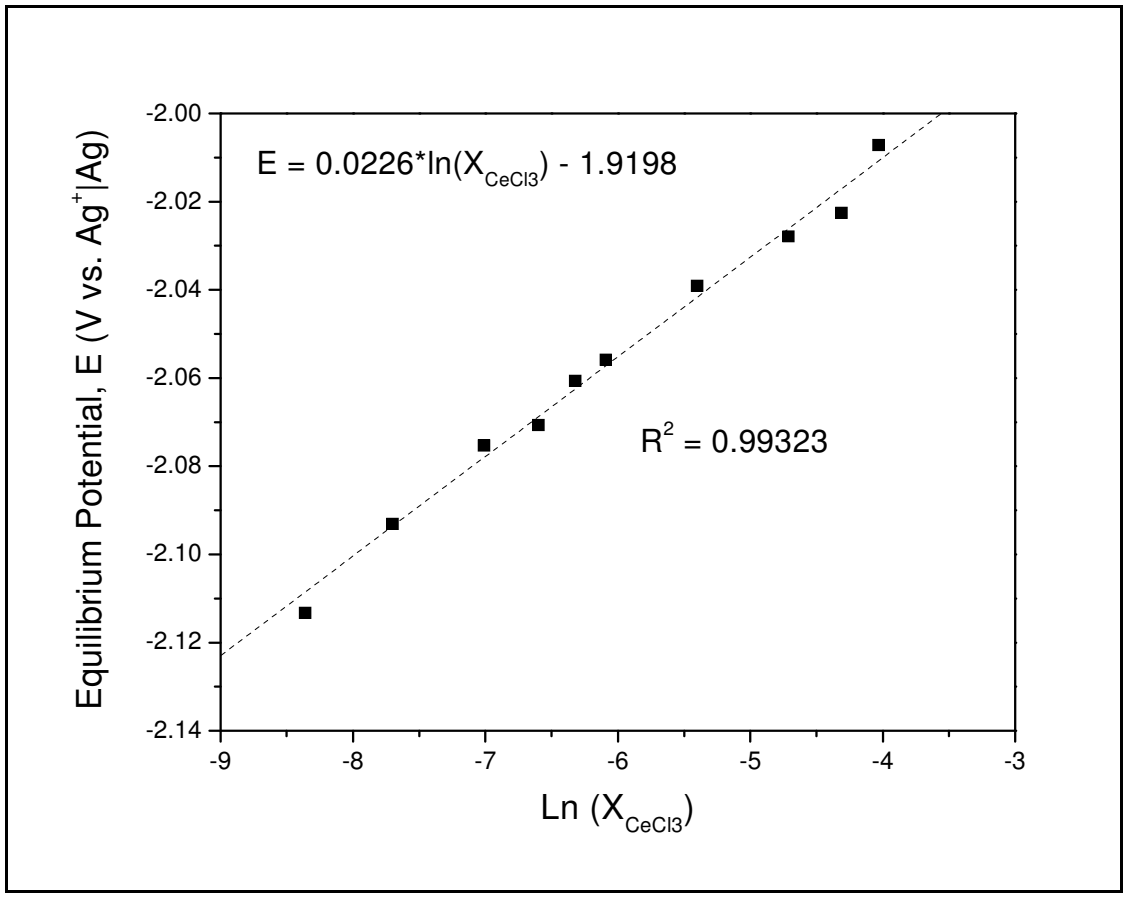

Figure 58. Nernst plot of the $CeCl_3$-LiCl-KCl concentration study. The slope of this plot should be equal to RT/nF, and the intercept is the apparent standard potential versus the 5 mol% $Ag^+|Ag$ reference electrode.

Again, the electrons transferred was calculated to be n = 2.95 ≈ 3 from the slope of the line in Figure 58, and the apparent standard potential was equal to $E^{0'}$ = -1.9198V on the $Ag^+|Ag$ reference scale ($E^{0'}$ = -3.07V vs. $Cl^-|Cl_2$).

The activity coefficient was then calculated by use of definition of the apparent standard potential:

$$\gamma_{CeCl_3} = exp\left[\frac{\left(E^{0'}_{CeCl_3} - E^{0}_{CeCl_3}\right)nF}{RT}\right] = exp\left[\frac{\left(\Delta G^{0'}_{CeCl_3} - \Delta G^{0}_{CeCl_3,\ sc}\right)}{RT}\right] = 3.03\text{x}10^{-3}$$

The peak current density responses from ASV and CV (both anodic and cathodic) were determined and found to be similar to the relationships found in the lanthanum concentration study. Figure 59 and Figure 60 are the ASV and cathodic CV calibration curves as functions of $CeCl_3$ concentration and Ce^{3+} ion concentration, respectively. Scan rate of 50 mV/s and plating step times of 60 seconds were used for all ASV experiments. The potential window was -2.4 – 0V vs. the $Ag^+|Ag$ reference electrode.

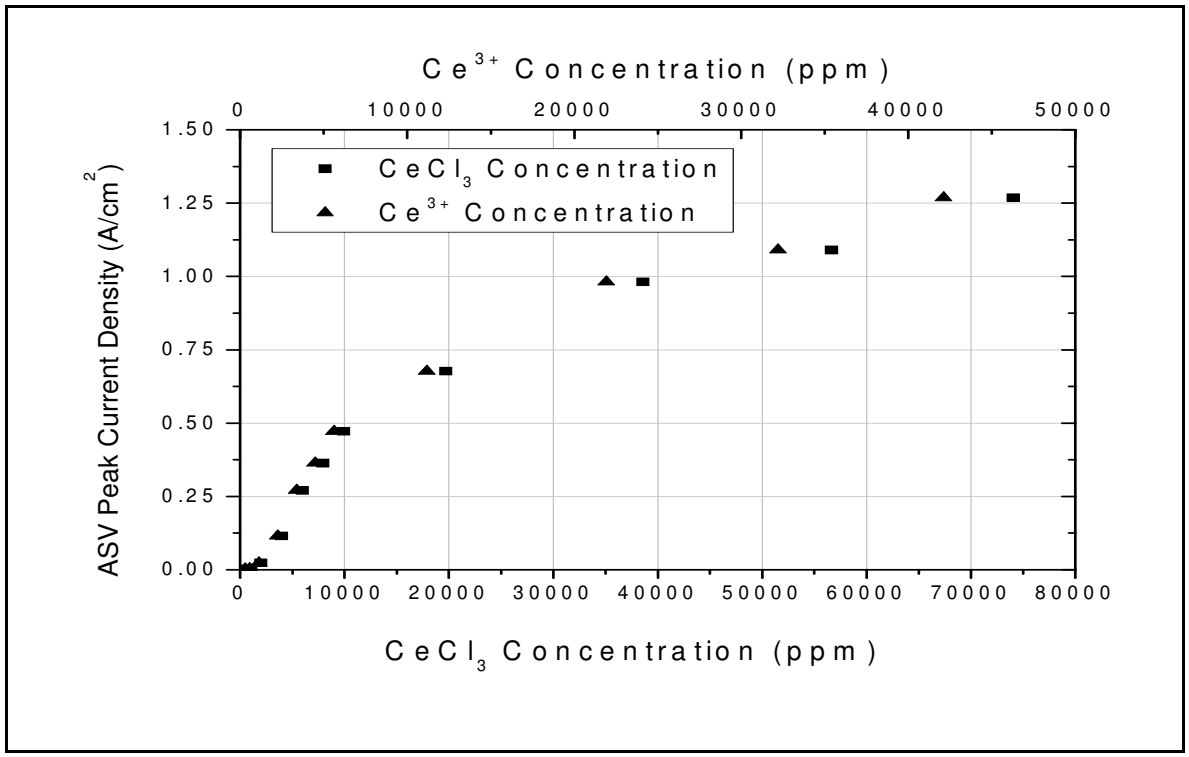

Figure 59. Cerium concentration study ASV calibration curve.

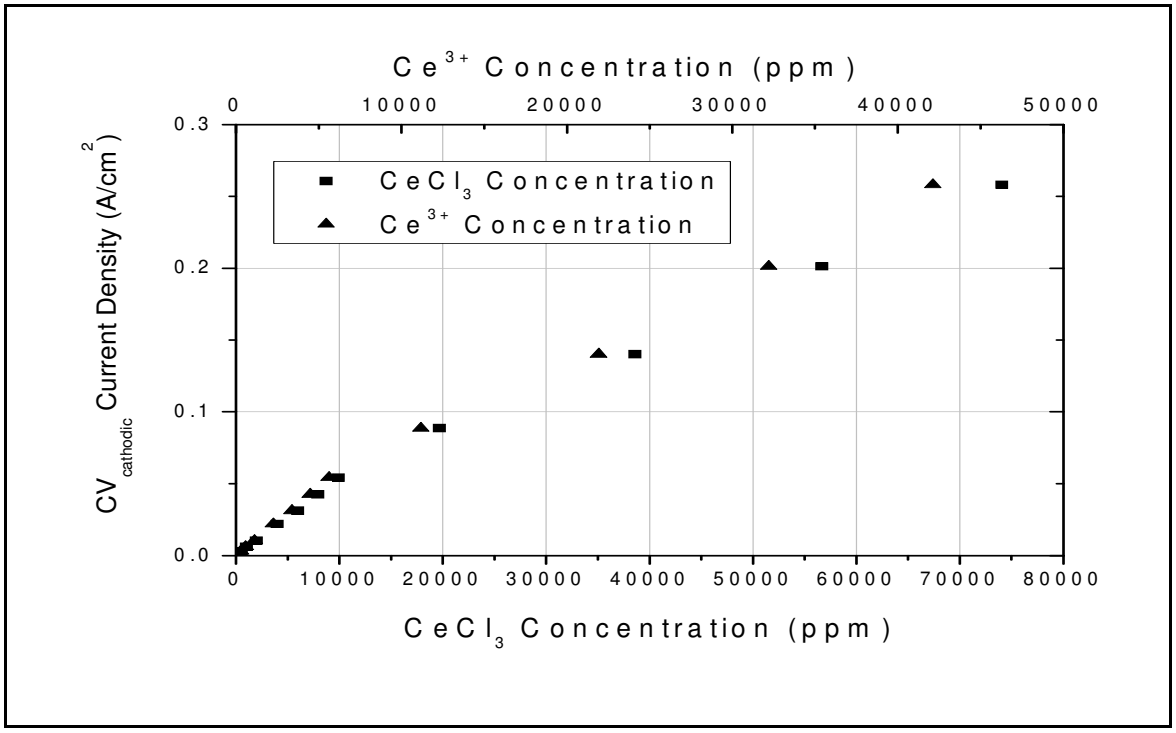

Figure 60. Cerium concentration study of absolute magnitude of cathodic CV peak current density.

The ASV curve, Figure 59, is once again slightly more bent than the CV cathodic curve, Figure 60, owing to the pre-concentration step in the ASV curve. The cathodic CV curve shows a very linear response to concentration with a nearly zero intercept as would be expected of a curve like this. However, there still seems to be some slight surface saturation effect at concentrations greater than 10,000 ppm $CeCl_3$.

5.1.3 Neodymium (III) Chloride in LiCl-KCl

The study of neodymium chloride in LiCl-KCl was slightly different from the La and Ce chlorides since the standard potential of neodymium chloride was slightly more anodic and the reaction mechanism proceeds in a two-step redox couple. Due to this two-step redox reaction, some ingenuity was needed to calculate the standard potential with the methods used for lanthanum and cerium. However, a method was developed based on a study of the two-step redox reaction of americium in molten LiCl-KCl [26].

A quick study of cyclic voltammograms obtained from the $NdCl_3$-LiCl-KCl salt immediately revealed differences between the $NdCl_3$-containing salt and both the $CeCl_3$ and $LaCl_3$-containing salts. Figure 61 shows typical cyclic voltammograms for the $NdCl_3$-LiCl-KCl salt system. While the large reduction and oxidation peaks look similar to the soluble-insoluble transition peaks seen in the La and Ce studies, a set of peaks shifted slightly to the right (positively) of the large peaks can be seen. These small, broad peaks can be associated with a soluble-soluble redox transition; that is, a transition in which the oxidation state is changed, but the analyte remains in solution.

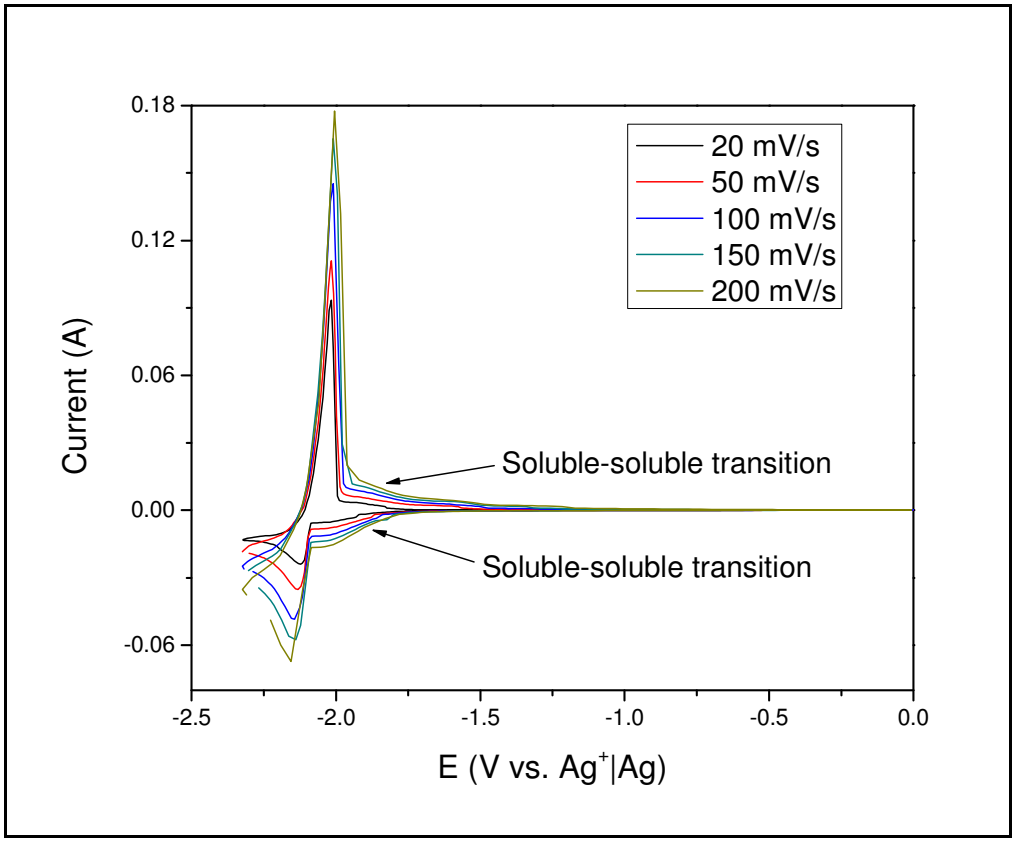

Figure 61. Cyclic voltammograms of $NdCl_3$ at 0.99 wt% ($X_{NdCl3} = 2.23x10^{-3}$) in LiCl-KCl.

Analyses of the cyclic voltammograms reveal that the large stripping and nucleation peaks corresponding to the soluble-insoluble transition are reversible in that the anodic and cathodic peak heights are proportional to the square root of scan rate and that the mid-peak potential does not shift significantly with scan rate. Further, through use of the Randles-Sevcik equation, the large stripping and nucleation peaks were determined to have a reaction mechanism that involves n = 2 electrons transferred. The smaller soluble-soluble transition peaks were not measureable since the peaks were broad, and the anodic peak was slightly covered by the much larger stripping peak. However, by logical reasoning, this small transition should correspond to a transfer of n = 1 electron. The full redox reaction occurring in an $NdCl_3$-LiCl-KCl salt is:

$$\text{Neodymium half} - \text{cell:}$$

$$\text{Step 1: } Nd^{3+}_{(aq)} + e^- \leftrightarrow Nd^{2+}_{(aq)}$$
$$\text{Step 2: } Nd^{2+}_{(aq)} + 2e^- \leftrightarrow Nd_{(s)}$$

$$\text{Chlorine half} - \text{cell: } \frac{3}{2}Cl_{2(g)} + 3e^- \leftrightarrow 3Cl^-_{(aq)}$$
$$\text{Full reaction: } Nd^{3+}_{(aq)} + 3Cl^-_{(aq)} \leftrightarrow \frac{3}{2}Cl_{2(g)} + Nd_{(s)}$$

Although two oxidation states of Nd exist in LiCl-KCl, their atomic sizes are similar and their diffusion coefficient may be assumed to be identical. Diffusion coefficient of Nd ions in the eutectic LiCl-KCl was determined using chronopotentiometry. Figure 62 shows a typical set of chronopotentiograms of $NdCl_3$-LiCl-KCl molten salt. The shape of this curve is important in establishing that the two types of ions reduce close enough to achieve a double-plateau chronopotentiogram since each potential plateau represents a specific species' reduction potential. Hence, the only potential plateaus observed are the Nd ion reduction plateau and the final electrolyte reduction plateau.

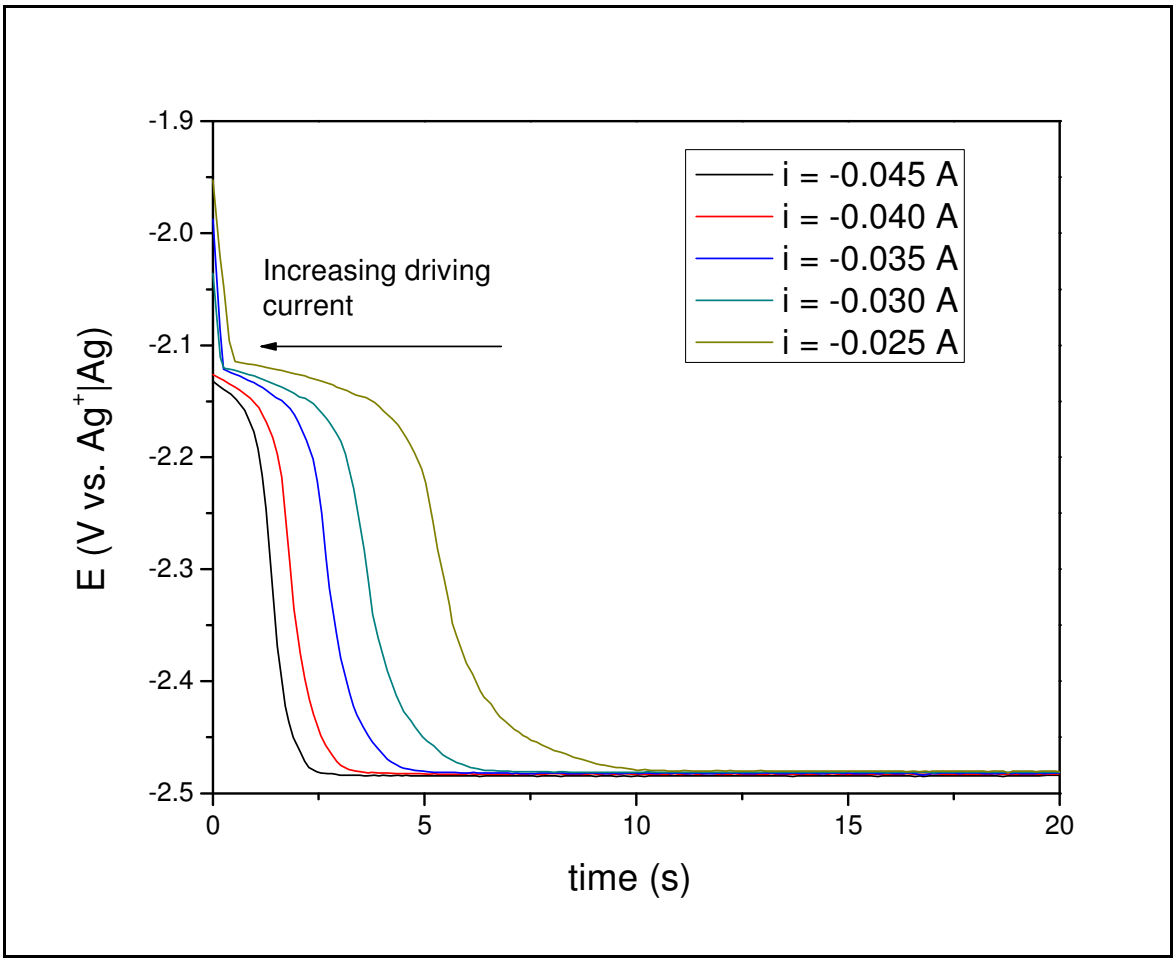

Figure 62. Typical chronopotentiograms of the $NdCl_3$-LiCl-KCl system. Data from 0.99 wt% $NdCl_3$ ($X_{NdCl3} = 2.23x10^{-3}$) in LiCl-KCl.

Nd metal ion diffusion coefficient in the eutectic LiCl-KCl is plotted as a function of $NdCl_3$ concentration and of Nd ion concentration in Figure 62. The neodymium ions exist in both the +2 and +3 oxidation states in the eutectic melt, so the neodymium ion concentration could be assumed to be the summation of total number of both ions in solution. Neodymium also exhibits an inverse dependency on the concentration of $NdCl_3$ and Nd ions in the eutectic melt, although the trend is not as severe as those observed for La and Ce.

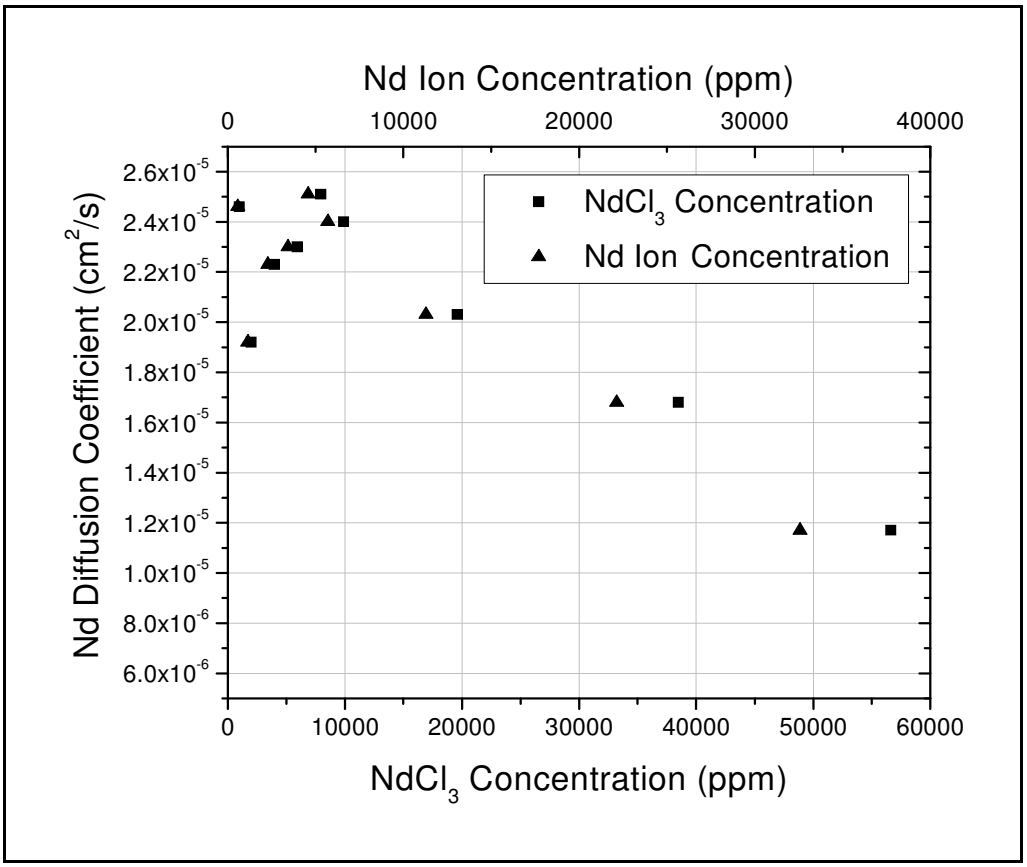

Figure 63. Neodymium diffusion coefficient as a function of $NdCl_3$ concentration and Nd metal ion concentration in the eutectic LiCl-KCl at 500°C.

Due to the coexisting 2^+ and 3^+ oxidation states of Nd in LiCl-KCl, the usual method of calculating the apparent standard potential of the $Nd^{3+} + 3e^- \leftrightarrow Nd$ redox couple can no longer be applied since the exact amount of Nd^{3+} in the melt is unknown. However, a method applied to americium, which has 2+ and 3+ oxidation states, in a journal article by Fusselman and colleagues [26] provides a route to calculating the standard potential of both the 3+ and the 2+ redox couple. The derivation is as follows:

Three redox couples exist in LiCl-KCl with dissolved Nd:

$$\begin{cases} Nd^{2+} + 2e^- \leftrightarrow Nd \\ Nd^{3+} + e \leftrightarrow Nd^{2+} \\ Nd^{3+} + 3e^- \leftrightarrow Nd \end{cases} \rightarrow \begin{matrix} \Delta G^{0'}_{Nd^{2+}} + RT\ln(X_{Nd^{2+}}) + 2\Delta G_{e^-} = \Delta G_{Nd(0)} \\ \Delta G^{0'}_{Nd^{3+}} + RT\ln(X_{Nd^{3+}}) + \Delta G_{e^-} = \Delta G_{Nd^{2+}} \\ \Delta G^{0'}_{Nd^{3+}} + RT\ln(X_{Nd^{3+}}) + 3\Delta G_{e^-} = \Delta G_{Nd(0)} \end{matrix}$$

Substituting that $\Delta G^{0'} = -nFE^{0'}$ and that $\Delta G_{Nd(0)} = 0$ (unit activity):

$$\begin{cases} 2^+: \ln(X_{Nd^{2+}}) = \dfrac{2F\left(E - E^{0'}_{Nd^{2+}}\right)}{RT} \\ 3^+: \ln(X_{Nd^{3+}}) = \dfrac{3F\left(E - E^{0'}_{Nd^{3+}}\right)}{RT} \end{cases}$$

Since the concentrations of Nd^{2+} and Nd^{3+} are unknown, these variables must be written in terms of total Nd ions, Nd^{Ox}, which is known:

$$X_{Nd^{Ox}} = X_{Nd^{2+}} + X_{Nd^{3+}}$$
$$X_{Nd^{2+}} = \varepsilon \cdot X_{Nd^{Ox}}$$
$$X_{Nd^{3+}} = (1-\varepsilon) \cdot X_{Nd^{Ox}}$$

where ε is the ratio of 2+ ions to the total oxidized ions in the salt. Combining the equations:

$$\varepsilon = \frac{1}{X_{Nd^{Ox}}} \cdot \exp\left[\frac{2F\left(E - E^{0'}_{Nd^{2+}}\right)}{RT}\right]$$

$$E^{0'}_{Nd^{3+}} = E - \frac{RT}{3F}\ln\left((1-\varepsilon)X_{Nd^{Ox}}\right)$$

The apparent standard potential of the 2+ state is found by measuring the equilibrium potential of the cyclic voltammograms attained at each concentration and making a Nernst equation, as shown in Figure 64. The intercept of this plot is the apparent standard potential of the 2+ state, $E^{0'}_{Nd^{2+}}$ = -1.8172V vs. $Ag^{+}|Ag$ reference (-2.9635V vs. $Cl^{-}|Cl_2$), which can then be used calculate the ε. The slope of Figure 64 yields a reaction mechanism of n = 1.62 ≈ 2 electrons, which illustrates the difficulty of measuring the apparent standard potential of a two-step redox couple as has been noted by Fusselman and coworkers [26].

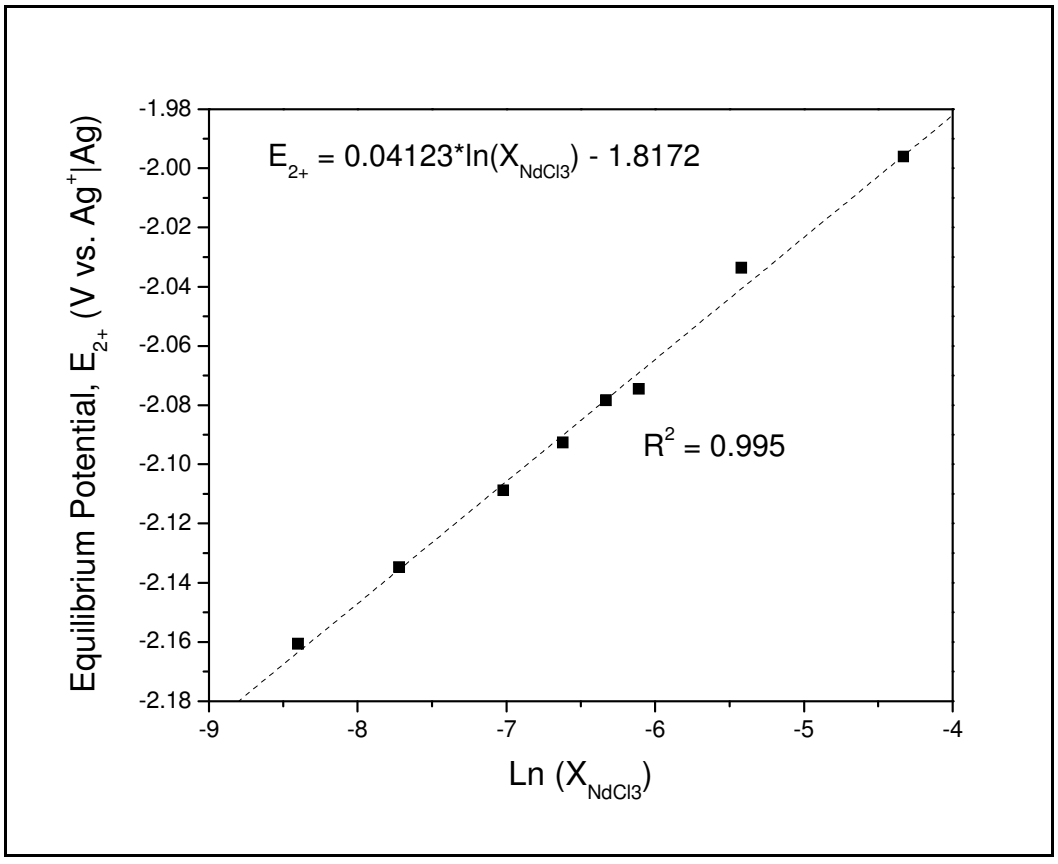

Figure 64. Nernst plot for the equilibrium potential, E_{2+}, with a slope of ~RT/nF and an intercept of the apparent standard potential for the $Nd^{2+}|Nd$ redox couple.

The apparent standard potential for the $Nd^{3+}|Nd$ redox couple was then determined by averaging each concentration's extracted $E^{0'}_{Nd^{3+}}$ together, which yielded an apparent standard potential of -1.94V vs. $Ag^{+}|Ag$ reference, or -3.0813V vs. $Cl^{-}|Cl_2$ reference scale.

Activity coefficient of $NdCl_3$ in LiCl-KCl at 500°C was calculated in a manner analogous to $CeCl_3$ and $LaCl_3$:

$$\gamma_{NdCl_3} = exp\left[\frac{\left(E^{0'}_{NdCl_3} - E^{0}_{NdCl_3}\right)nF}{RT}\right] = exp\left[\frac{\left(\Delta G^{0'}_{NdCl_3} - \Delta G^{0}_{NdCl_3,\ sc}\right)}{RT}\right] = 3.55\text{x}10^{-4}$$

The concentration vs. current density plots for $NdCl_3$ are similar in trend to those determined for $LaCl_3$ and $CeCl_3$. For all peak measurements, the peak height of the $Nd^{2+}|Nd$ couple was measured, and a scan rate of 50 mV/s and plating time of 60 seconds was maintained for all concentrations for the construction of the ASV calibration curve. The plating potential during ASV was also changed to -2.3V vs. $Ag^{+}|Ag$ reference state. Figure 65 depicts the ASV peak current density response. The CV anodic and cathodic peak current density responses showed similar trends. The ASV curve does not exhibit the three-regime behavior as was observed for $LaCl_3$ and CeCl3 concentration studies, but instead seems to exhibit constant quasi-logarithmic behavior. The absolute peak current for the cathodic CV curve is once again very linear for a large range of concentrations.

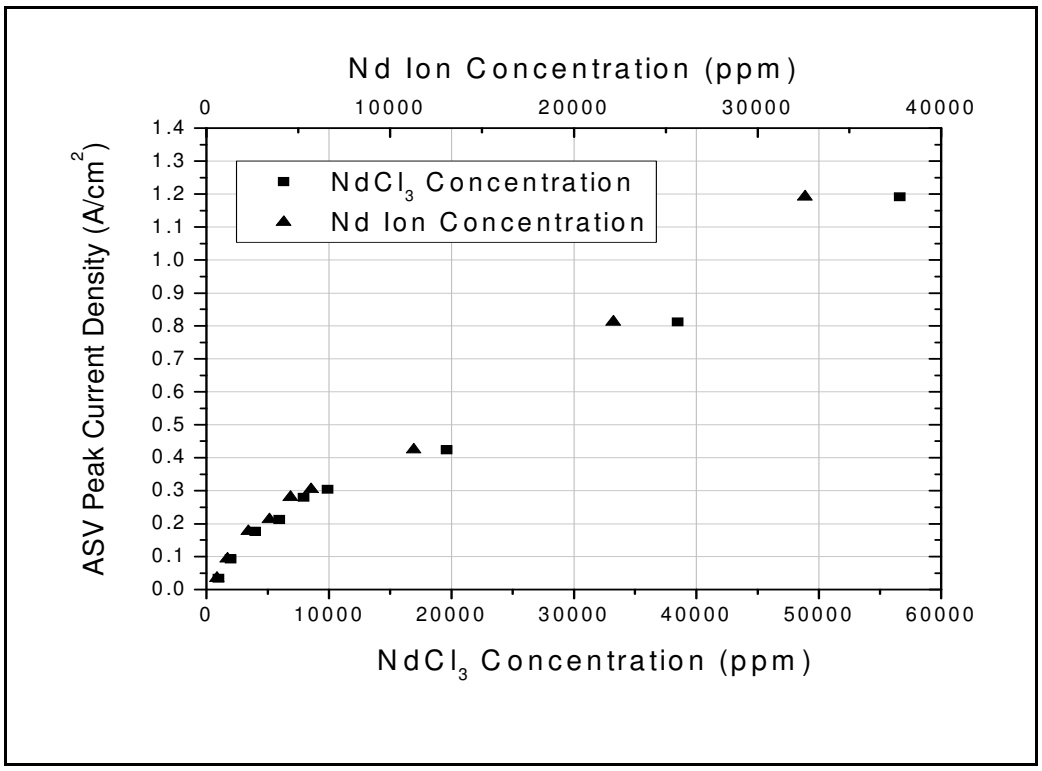

Figure 65. Peak current density as a function of neodymium concentration in ASV experiments.

5.1.4 Dysprosium (III) Chloride in LiCl-KCl

The electrochemical behavior of dysprosium (III) chloride in LiCl-KCl eutectic salt at 500°C was characterized using CV, CP, and ASV. $DyCl_3$ concentrations of 0.5-8 wt% were investigated. Figure 66 shows typical cyclic voltammograms obtained from the $DyCl_3$-LiCl-KCl salt containing 2 wt% $DyCl_3$. Figure 67 shows a plot of the anodic and cathodic peak currents from the cyclic voltammograms in Figure 66 as a function of the square root of the scan rate. The linearity of this plot confirms the reversibility of the redox reaction and the applicability of the Randles-Sevcik equation. The small deviation from linearity of the peak anodic current at high scan rates is the result of the slow data collection rate of the potentiostat. The potentiostat is only able to measure 8 points per second, and at high scan rates, the potentiostat is not able to capture the true shape of the oxidation peak since the reaction happens so quickly. The peak current curve often appears "jagged" and the peak current value is missed because the reaction happens so quickly and the potentiostat cannot collect enough data points at the peak of the curve. The Nernstian behavior of the reaction can be further confirmed by observing the mid-peak potential as a function of scan rate as shown in Figure 68. The mid-peak potential does not shift significantly with scan rate, so the redox reaction can be considered reversible.

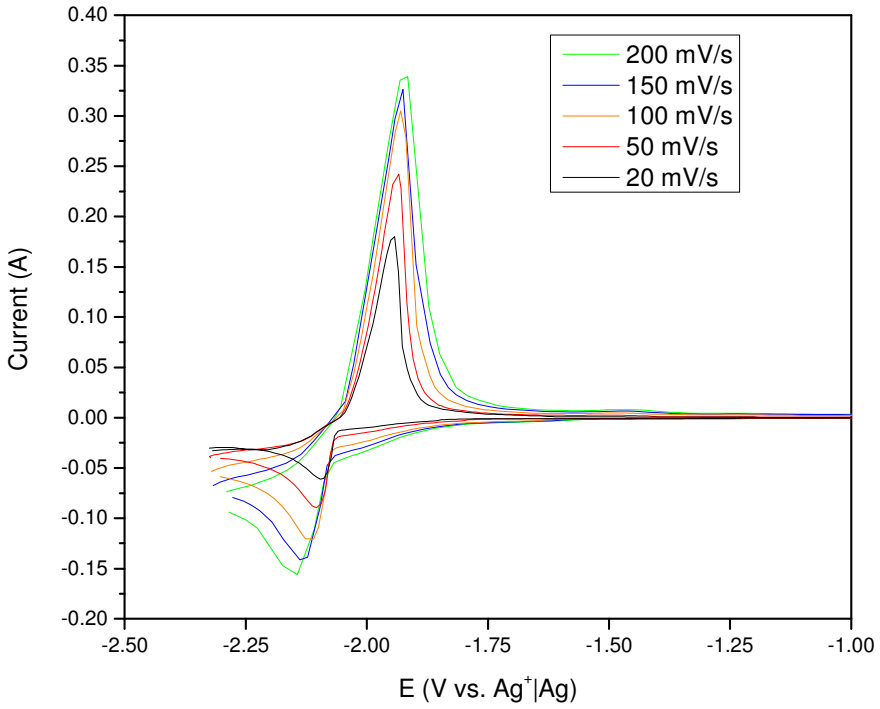

Figure 66. Cyclic voltammograms of $DyCl_3$ at 2 wt% in LiCl-KCl at 500°C.

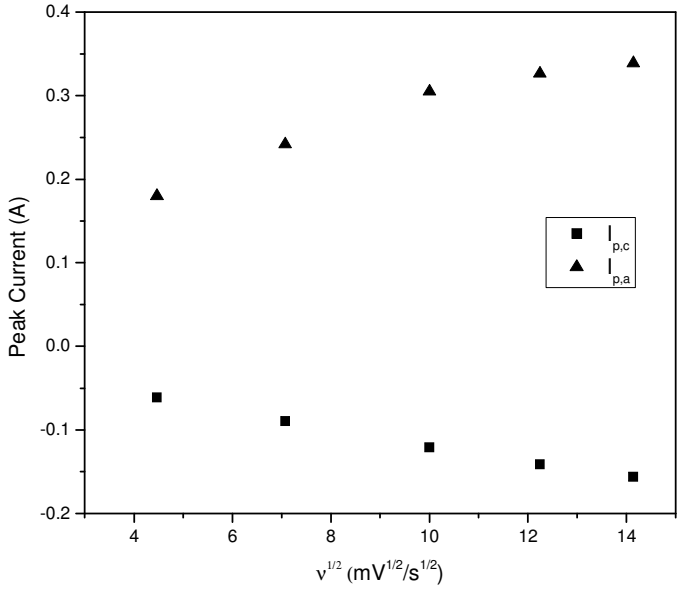

Figure 67. Peak cathodic and anodic current as a function of the square root of the scan rate, $\nu^{1/2}$. Data obtained from $DyCl_3$-LiCl-KCl salt containing 10,000 ppm $DyCl_3$. The linearity of this plot confirms the reversibility of the redox reaction.

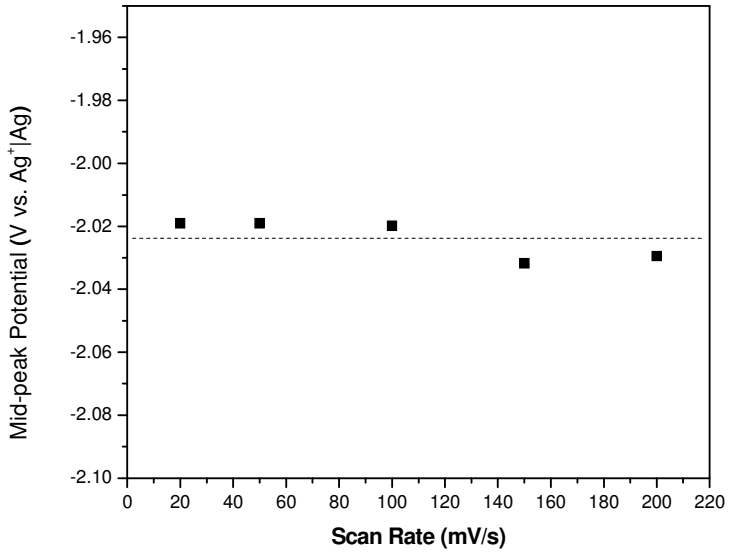

Figure 68. Mid-peak potential as a function of scan rate. Data obtained from $DyCl_3$-LiCl-KCl salt containing 2 wt% $DyCl_3$. The dashed line represents the average mid-peak potential.

The large oxidation peak is has the characteristics shape of a soluble-insoluble redox reaction. This peak represents the oxidation of insoluble Dy metal to soluble Dy^{3+}. Visual inspection of the cyclic

voltammograms and comparison to the previous rare earth studies seemed to show some indication of a soluble-soluble transition between the 2+ and 3+ oxidation states on the cathodic sweep of the voltammogram. The evidence for this intermediate transition was the small broad peaks located to the right of main peak on the cyclic voltammograms. However, the presence of these soluble-soluble peaks is debatable based on visual analysis alone. Castrillejo and coworkers [42] concluded that the electroreduction of Dy^{3+} is composed two very close cathodic steps from Dy^{3+}/Dy^{2+} and Dy^{2+}/Dy. Due to the difficulty of resolving the two separate cathodic peaks, other researchers including Chang and coworkers [46] have treated the Dy^{3+} reduction as a single-step process from Dy^{3+} to Dy with successful results. A quantitative analysis of the large cathodic peaks of the cyclic voltammograms using the Randles-Sevcik equation yielded the number of electrons transferred to be n≈3 for almost all concentrations (see Table IX). Therefore, for all further analysis, the electroreduction of Dy^{3+} will be treated as a single-step process redox process, which is shown below:

$$\text{Dysprosium half} - \text{cell:} \quad Dy^{3+}_{(aq)} + 3e^- \leftrightarrow Dy_{(s)}$$

$$\text{Chlorine half} - \text{cell:} \quad \frac{3}{2}Cl_{2(g)} + 3e^- \leftrightarrow 3Cl^-_{(aq)}$$

$$\text{Full Reaction:} \quad Dy + 3Cl^-_{(aq)} \leftrightarrow \frac{3}{2}Cl_{2(g)} + Dy_{(s)}$$

Table IX. Number of electrons transferred in dysprosium reduction reaction at various concentrations. Values were calculated from the cathodic peak of the 50 mV/s voltammogram at each concentration.

$DyCl_3$ Concentration (ppm)	Electrons Transferred
1017	2.74
2008	1.93
3996	3.01
5999	3.08
8006	3.07
10017	3.05
20028	3.03
39990	2.93
60018	3.02
79996	3.10

Chronopotentiometry was also performed on the $DyCl_3$-containing salts in order to determine the diffusion coefficient of dysprosium ions in LiCl-KCl. Figure 69 shows a typical set of chronopotentiograms from LiCl-KCl containing 2 wt% $DyCl_3$ at 500°C. As with CV, the first step is to confirm the reversibility of the electrode reaction. Once this has been shown, analysis can proceed using the Sand equation. Figure 70 shows the driving current of the chronopotentiograms in Figure 69 as a function of the inverse of the square root of the transition time. The linear relationship between the two parameters demonstrates that the reduction of dysprosium ions onto the working electrode is a reversible, diffusion-controlled process and the Sand equation is applicable. This relationship was found at all $DyCl_3$ concentrations.

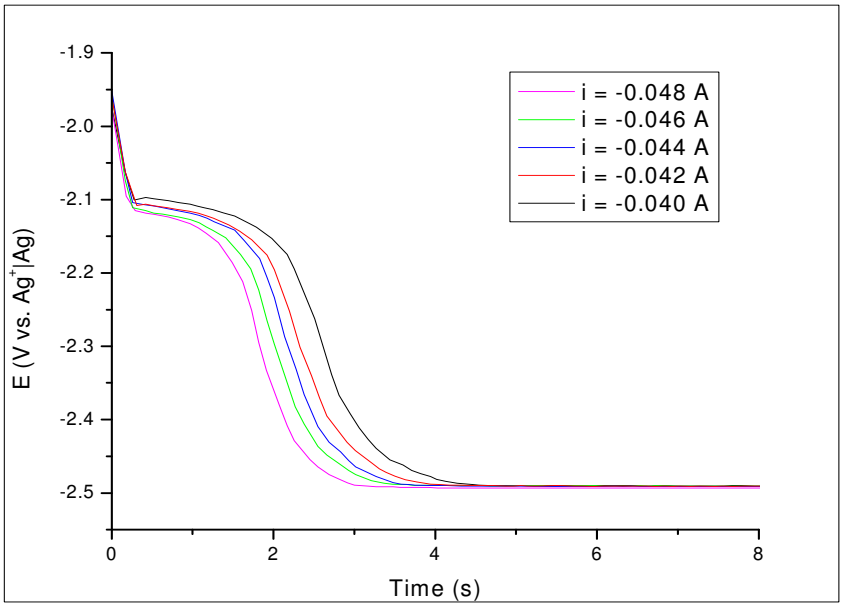

Figure 69. Typical chronopotentiograms of the $DyCl_3$-LiCl-KCl system. Data obtained from 2 wt% $DyCl_3$ salt.

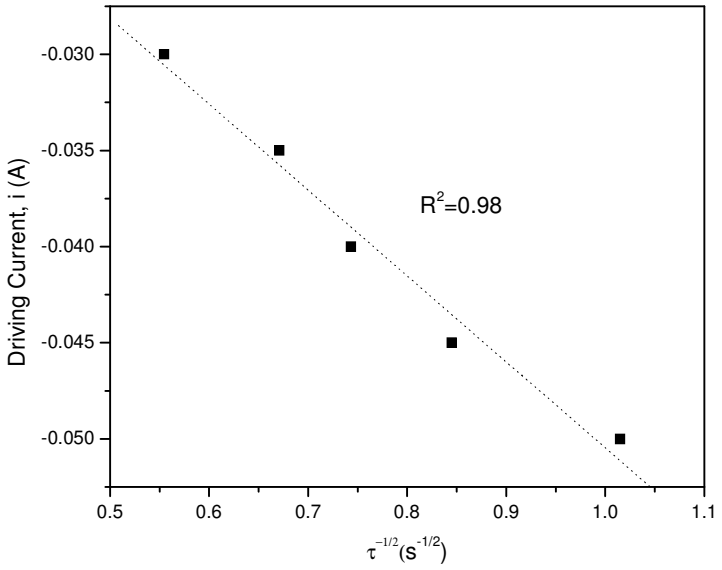

Figure 70. Driving current as a function of the inverse of the square root of the transition time for chronopotentiograms taken from LiCl-KCl containing 2 wt% $DyCl_3$ at 500°C. Linearity of this plot confirms the reversibility of the redox reaction.

The double-plateau shape of the chronopotentiograms in Figure 69 indicates that the two oxidation states of dysprosium, Dy^{3+} and Dy^{2+}, reduce at close enough potentials that their diffusion coefficients may be assumed to be identical. If the diffusion coefficients were significantly different, a third plateau would be visible on the chronopotentiograms. As expected, the transition time of the chronopotentiograms decreased as the driving current increased. At high concentrations (>40,000ppm), the chronopotentiograms would often not reach the second plateau at approximately -2.45 V corresponding to the reduction potential of Li^+. The first voltage plateau corresponds to the equilibrium potential of the $Dy^{3+}|Dy$ reaction. As all of the Dy ions in the vicinity of the working electrode are reduced, the next most electroactive species (Li in this case) will begin to reduce in order to keep the current flowing and the voltage will transition to the second plateau. At high concentrations, there is a large amount of material being plated onto the working electrode and it is theorized that there is a competing reoxidation of the reduced metal which the driving current cannot suppress. This is thought to be the reason why the second voltage plateau is not observed in chronopotentiograms at high concentrations. This behavior was also observed in the previous electrochemical studies of La, Ce, and Nd. Unfortunately, this seems to be a limiting issue for chronopotentiometry. However, increasing the surface area of cathode might help to deter the re-oxidation of reduced metal. A WE with a larger area would produce a thinner electrodeposit therefore reducing the resistance between the WE and the bulk electrolyte.

Figure 71 shows the results obtained investigating the diffusion coefficient as a function of $DyCl_3$ concentration. The diffusion coefficients were calculated using the Sand equation and assuming a three electron transfer. At each concentration, a diffusion coefficient was calculated using each of the five chronopotentiograms and an average value was determined. The Dy ion diffusion coefficient measured by Castrillejo and coworkers [42] is included on the plot for reference. The error for each concentration was determined by taking the standard deviation of the measured values. Additional sources of error not accounted for in the error bars are the measurement of the wetted length of the WE and the graphical measurement of the transition time.

Previous studies investigating La, Ce, and Nd diffusion coefficients studies revealed an inverse relationship between diffusion coefficient and concentration. The Dy ion diffusion coefficient seems to follow a similar trend, however, it drops off more quickly below 1 wt% and then appears to level out somewhat. The Dy diffusion coefficient varies by approximately one order of magnitude over the range of concentrations studied. La, Nd, and Ce were found to decrease by a similar magnitude. The exact reason for this trend is not known, however, it is theorized that increased interaction between the liked-charged ions at high concentrations slows the diffusion of the ions towards the electrode.

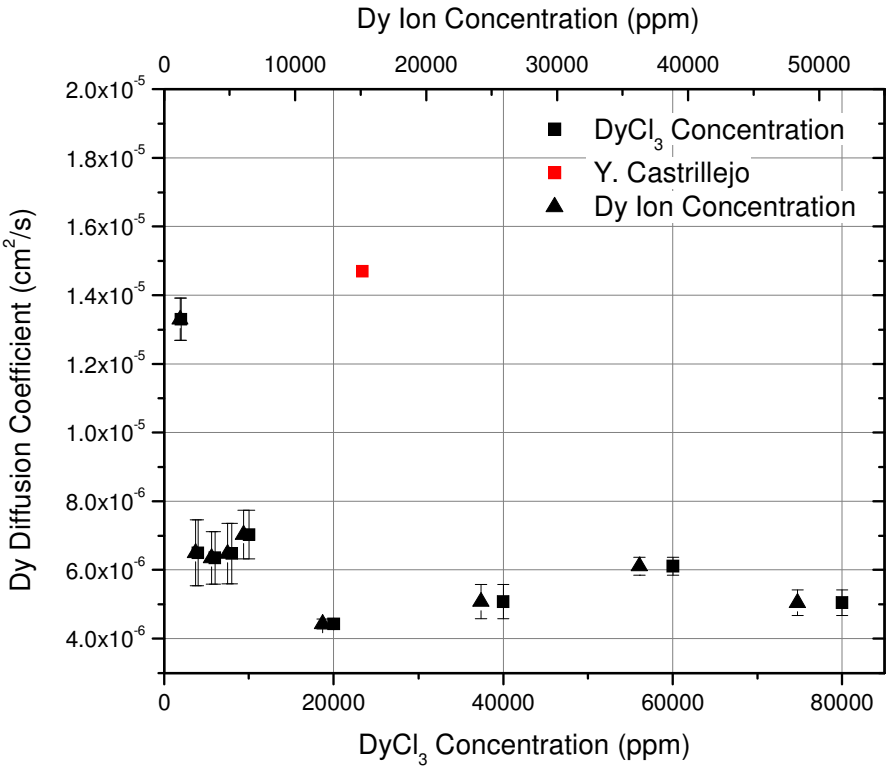

Figure 71. Dysprosium ion diffusion coefficient as a function of $DyCl_3$ concentration in molten LiCl-KCl salt at 500°C.

Figure 72 depicts the ASV peak current density response as a function of $DyCl_3$ concentration. This curve depicts a familiar trend with a slight change in slope below 10,000 ppm. This "bend" has also been observed in the previous rare earth studies and is attributed to surface saturation effects of the working electrode. The error was determined by calculating the standard deviation of the peak heights at each concentration. The error increases significantly at high concentrations. At high concentrations there was difficulty obtaining a well-mixed salt with no mechanical mixing and this could be a partial cause of the higher error. In addition, at high concentrations, there is a much larger amount of material being reduced onto the working electrode during the plating step. It is theorized that this large amount of material causes complications in the oxidation process which distorts the stripping peak. ASV curves at high concentrations sometimes exhibited a "hump" to the right of the main stripping peak. Reducing the plating time of the pre-concentration step might help to prevent this behavior.

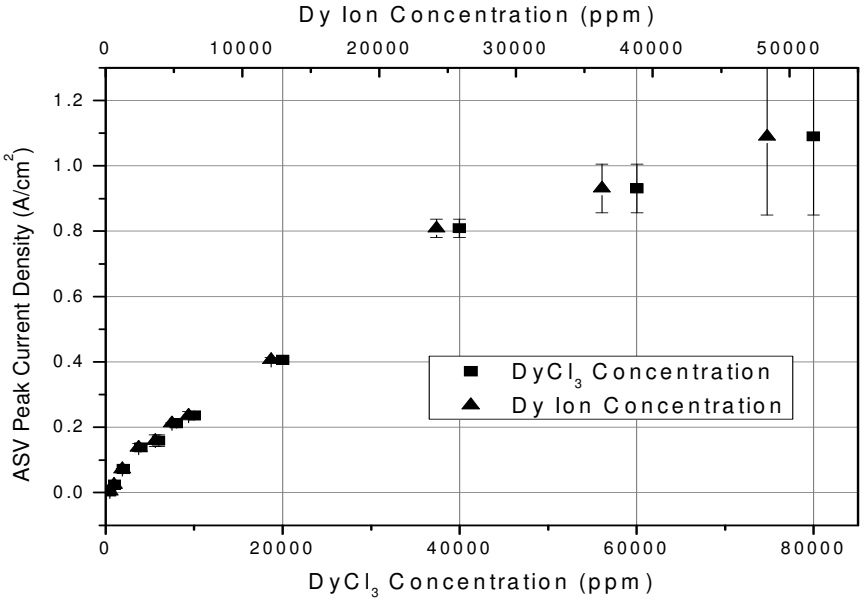

Figure 72. Peak current density as a function of $DyCl_3$ and Dy ion concentration for ASV experiments (plating time = 60 sec., scan rate = 50 mV/s, ΔE = -2.3V-0V).

The cathodic and anodic peak current densities are plotted as a function of $DyCl_3$ and Dy ion concentration in Figure 73 and Figure 74 respectively. These CV curves exhibit a similar shape to the ASV working curve, however, they do not have the "bend" near 10,000 ppm that the ASV curve does. The CV curves stay very linear in this region while the ASV curve shows a higher slope at low concentrations which is believed to be a result of the initial plating step which causes more severe surface saturation effects. Matching observations from previous studies, the CV cathodic curve is more linear than CV anodic curve. The 80,000 ppm point on the anodic curve appears to have a rather low current density which breaks linear trend of the previous points. This is attributed to the salt not having been mixed completely. Since no mechanical mixing is employed, high concentration salts need more time at temperature to allow diffusion and convection to sufficiently mix the salt. However, thermal cycling of the system puts significant stress on the glassy carbon crucible and breakages were very common when attempting to measure the higher concentration salts. Therefore, it was difficult to obtain accurate results from a well-mixed salt before the glassy carbon crucible would break. In future studies, it would be beneficial to use a stirrer or bubble inert gas through the salt to speed up the mixing process.

Error bars are not included on the CV working curves because an accurate calculation of the error was not possible as it was with ASV. With ASV, ten scans were taken and the standard deviation in the peak height was obtained. With CV, only one or two scans were obtained at each scan rate so an accurate calculation of the peak height standard deviation was not possible. Furthermore, additional error is introduced with the measurement of the wetted length of the WE. However, this error cannot accurately be quantified because it involves the subjective judgment of the researcher to correctly identify the wetted depth on the electrode.

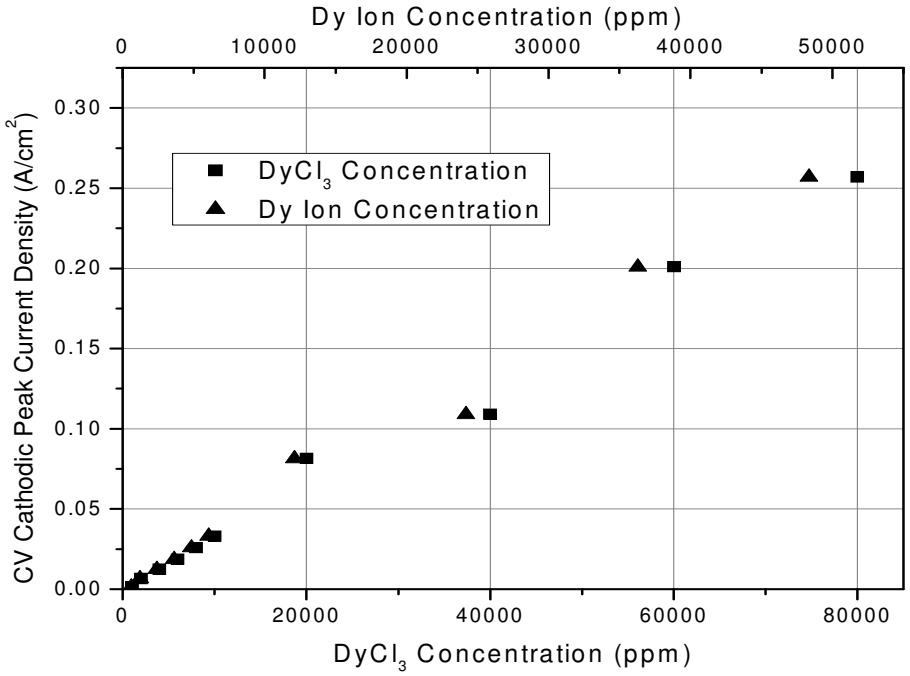

Figure 73. Cathodic peak current as a function of $DyCl_3$ and Dy ion concentration for CV experiments.

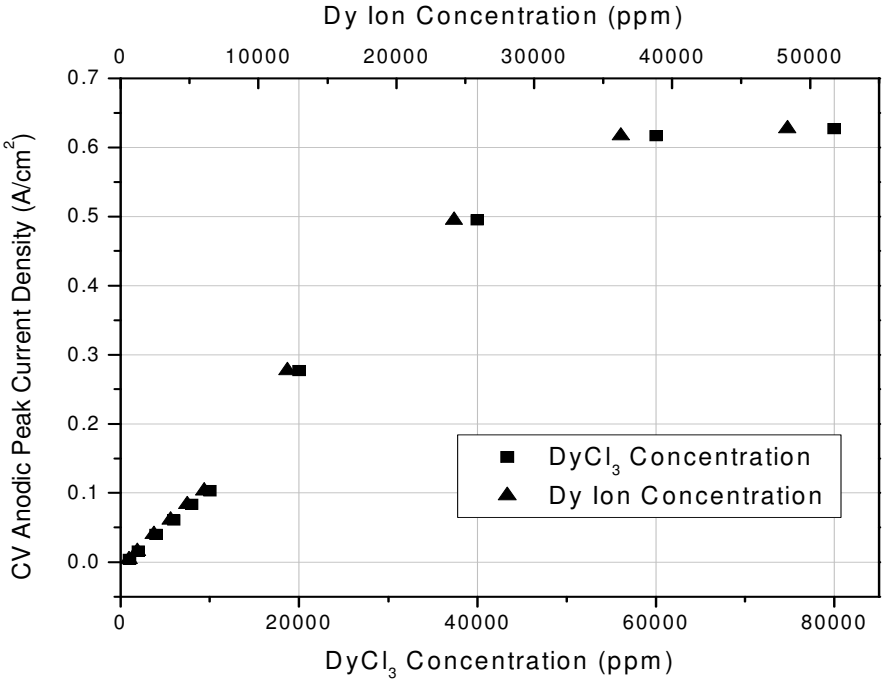

Figure 74. Anodic peak current as a function of $DyCl_3$ and Dy ion concentration for CV experiments.

Since the Dy^{3+} redox reaction is being treated as a single-step process, the apparent standard potential of Dy^{3+}/Dy reaction can be determined with a Nernst plot, using the same method described in section 5.1.2.1. The same method was successfully used to determine the apparent standard potentials of La^{3+} and Ce^{3+} redox reactions which were studied with this apparatus prior to the current Dy study. The dysprosium Nernst plot is shown in Figure 75 below. The plot shows the average mid-peak potential of the cyclic voltammograms as a function of the natural log of the molar concentration of dysprosium. The apparent standard potential is determined by applying a linear fit to the data and extrapolating the equilibrium potential to X=1.0 (the y-intercept of the plot). Observing Figure 75, it can be seen that the apparent standard potential of dysprosium is -1.958 V vs. the 5 mol% Ag^{+}|Ag reference electrode or -3.104 V vs. $Cl^{-}|Cl_2$ reference electrode. This compares well with the value of -3.150 V vs. $Cl^{-}|Cl_2$ determined by Chang and coworkers [43] at 450°C.

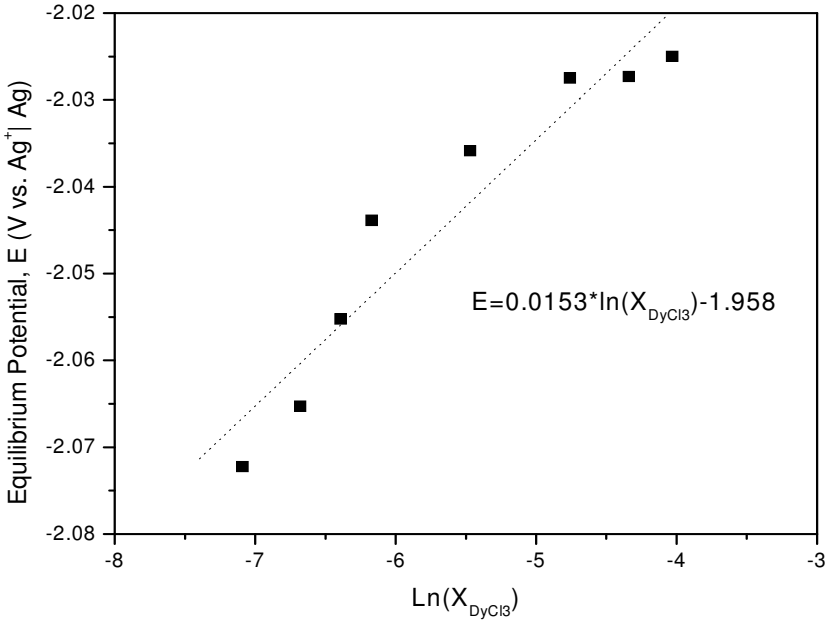

Figure 75. Nernst plot of the $DyCl_3$-LiCl-KCl concentration study. The y-intercept of the linear fit is the apparent standard potential versus the 5 mol% Ag^{+}|Ag reference electrode.

5.1.5 Depleted Uranium (III) Chloride in LiCl-KCl

A short study investigating the electrochemical behavior of depleted UCl_3 was performed at the Center for Advanced Energy Studies at Idaho National Laboratory. Figure 76 shows the cyclic voltammograms obtained from the LiCl-KCl eutectic containing 1 wt% UCl_3 at 500°C. Voltage scan rates of 25, 50, 100, 150, and 200 mV/s are shown. Three anodic peaks (I_a, II_a, and III_a) and three cathodic peaks (I_c, II_c, and III_c) are clearly visible. The largest anodic and cathodic peaks (I_a and I_c) appear to have the characteristic shape of a soluble-insoluble redox transition. Multiple studies have reported these peaks to be the result of the $U^{3+/}U$ redox couple. Some report this reaction to be reversible while others have found it to be quasi-reversible [44], [45], [46]. Figure 77 shows a plot of the cathodic peak (I_c) current as

a function of the square root of the scan rate, $\nu^{1/2}$. A linear relationship is apparent, indicating that the reduction process is reversible. However, the anodic peak does not show the same result. Figure 78 shows a plot of the anodic peak (I_a) current as a function of the scan rate and it can be seen that a linear relationship does not exist. Shirai [47] also found no correlation between this anodic peak current and the square root of the scan rate and suggested that this behavior could be caused by the formation of an alloy between U and the working electrode material. The mid-peak (I_a/I_c) potential is plotted as a function of scan rate in Figure 79. There is only a slight change in the mid-peak potential at the lowest scan rate of 25 mV/s. Furthermore, the potential difference between the anodic and cathodic peak was measured (see Table X) and determined to be twice or three times as large as the theoretical value, and increased with scan rate. Considering all of this evidence, the I_a/I_c redox couple will be treated as a quasi-reversible reaction. The Randles-Sevcik equation was used to determine the number of electrons transferred in the redox reaction using the cathodic peak current and a diffusion coefficient calculated using chronopotentiometry. The number of electrons transferred was calculated to be 2.39. This illustrates the inaccuracy of using the Randles-Sevcik equation to analyze a system that does not exhibit completely reversible behavior.

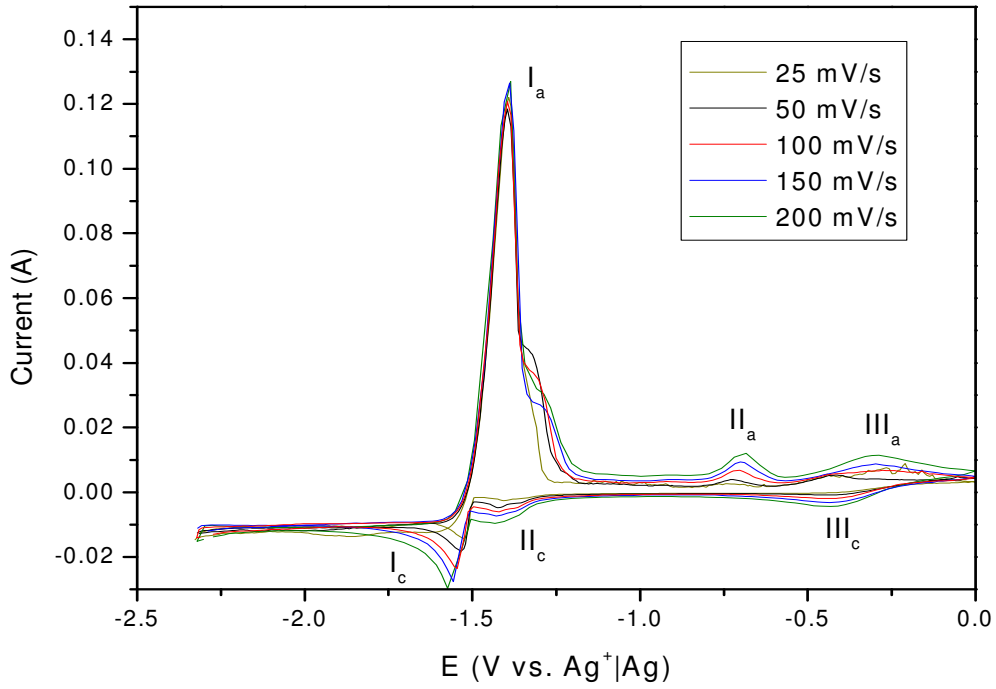

Figure 76. Cyclic voltammograms of LiCl-KCl eutectic containing 1 wt% UCl_3 at 500°C.

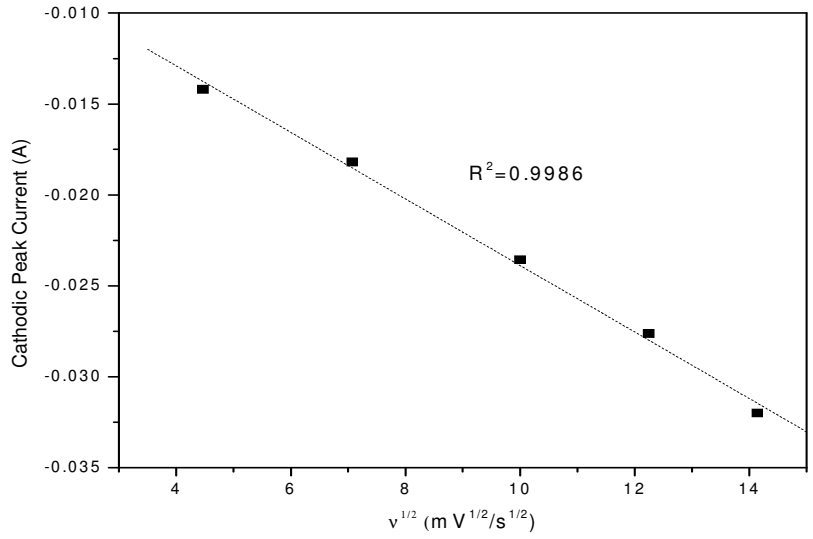

Figure 77. Peak (I_c) cathodic current as a function of the square root of the scan rate, $\nu^{1/2}$. Data obtained from cyclic voltammograms of LiCl-KCl salt containing 1 wt% UCl_3 at 500°C.

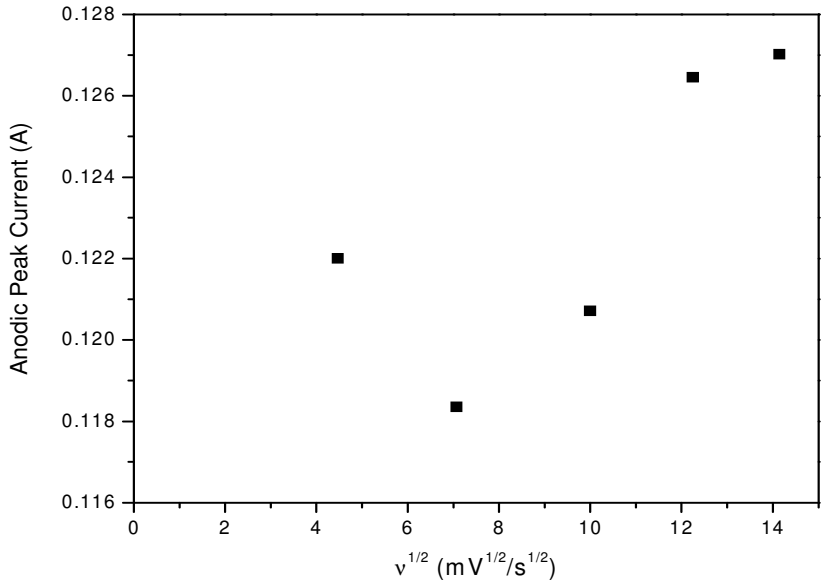

Figure 78. Peak (I_a) anodic current as a function of the square root of the scan rate, $\nu^{1/2}$. Data obtained from cyclic voltammograms of LiCl-KCl salt containing 1 wt% UCl_3 at 500°C.

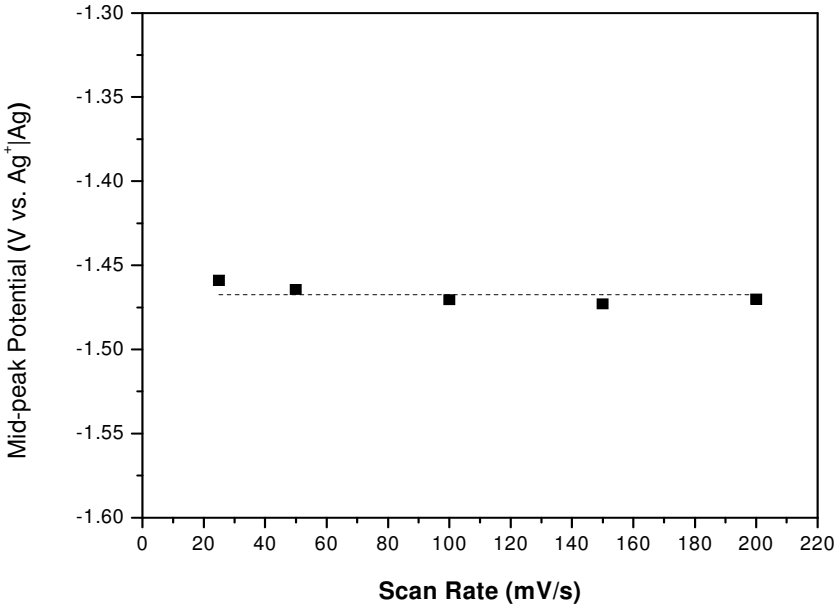

Figure 79. Mid-peak (I_a/I_c) potential as a function of scan rate. Data obtained from cyclic voltammograms of LiCl-KCl salt containing 1 wt% UCl_3 at 500°C.

Table X. Measured and calculated peak potential difference for cyclic voltammograms at various scan rates. ΔE is measured between peaks I_a and I_c.

	ΔE (V)	
Scan Rate (mV/s)	measured	calculated
25	0.135	0.051
50	0.139	0.051
100	0.150	0.051
150	0.168	0.051
200	0.167	0.051

The second anodic and cathodic peaks (II_a and II_c) show a large separation voltage which is indicative of irreversible behavior. A reversible redox process with a one electron transfer at 500°C is expected to show a difference in peak potential of 153 mV. However, the average ΔE between peaks II_a and II_c for all scan rates is 711 mV. This large ΔE confirms the irreversible behavior of this electrode process. Serrano and Taxil [48] observed similar pre-peaks in their investigation of uranium in NaCl-KCl and attributed their presence to the adsorption and desorption of an insoluble uranium monolayer on the working electrode.

The last two peaks, III_a and III_c, are shorter and broader peaks located at more positive potential. Figure 80 plots the anodic and cathodic peak potential versus the scan rate. The linearity of these plots confirms the reversibility of the redox process. The 25 mV/s scan was omitted from these plots because it was very noisy in the potential range of this redox couple and the peaks could not be discerned with

significant accuracy. The 50 mV/s scan was also somewhat noisy and this could be the reason for the slight deviation from linearity of the 50 mV/s point in Figure 80. Furthermore, Figure 81 shows little variation in the mid-peak potential as a function of scan rate with the exception of the 50 mV/s point, which once again is attributed to a noisy signal. In addition, the potential differences between the anodic and cathodic peaks, shown in Table XI, were found to be reasonably close to the theoretical value (with the exception of the 50 mV/s scan). Assuming that the deviation from reversibility of the 50 mV/s scan was due to a noisy signal, it can be concluded that the reaction is reversible. Using the peak separation equation ($n = 2.3 \cdot R \cdot T/(\Delta E \cdot F)$) to calculate the number of electrons transferred yields an average value of $1.04 \approx 1$. This suggests that the III_a/III_c peaks represent the U^{4+}/U^{3+} redox couple. This conclusion is supported by multiple other researchers [44], [45], [46].

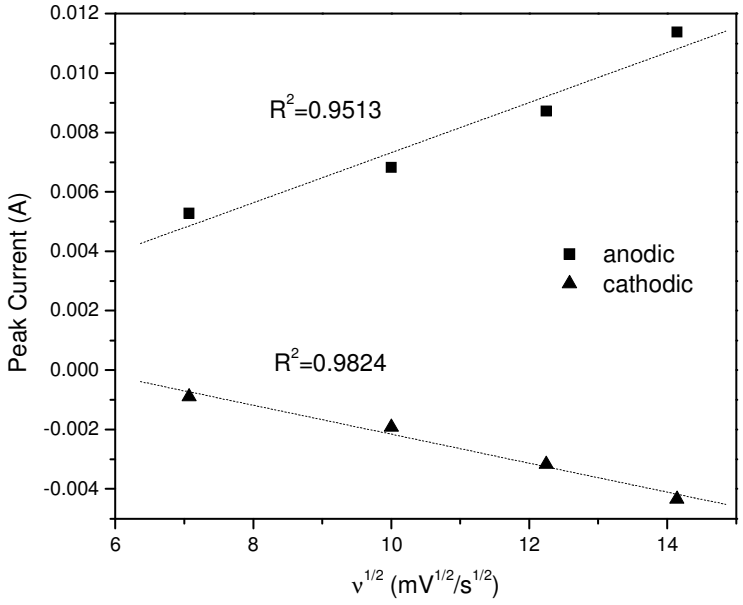

Figure 80. Peak cathodic (III_c) and anodic (III_a) current as a function of the square root of the scan rate, $\nu^{1/2}$. Data obtained from LiCl-KCl salt containing 1wt% $DyCl_3$.

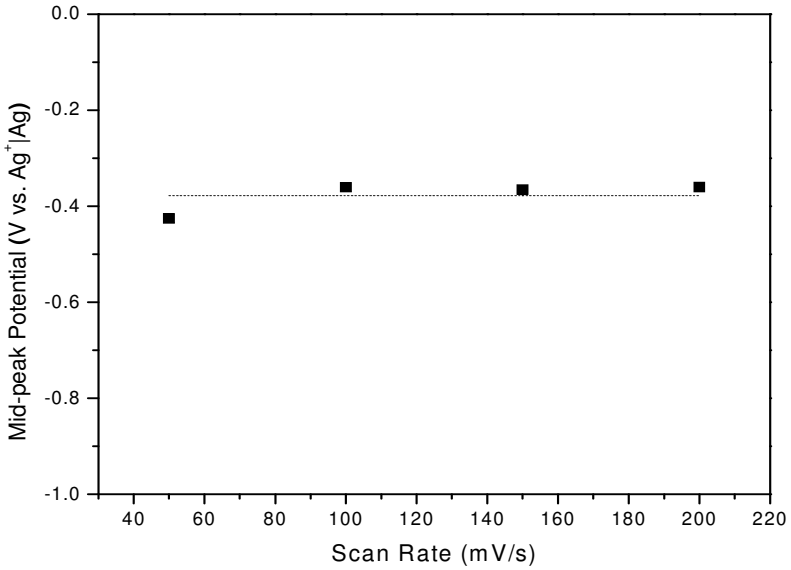

Figure 81. Mid-peak (III_a/III_c) potential as a function of scan rate. Data obtained from cyclic voltammograms of LiCl-KCl salt containing 1 wt% UCl_3 at 500°C.

Table XI. Measured and calculated peak potential difference for cyclic voltammograms at various scan rates. ΔE is measured between peaks III_a and III_c.

	ΔE (V)	
Scan Rate (mV/s)	measured	calculated
50	0.015	0.153
100	0.166	0.153
150	0.136	0.153
200	0.144	0.153

Figure 82 shows chronopotentiograms obtained from the 1 wt% UCl_3 salt at 500°C for driving currents of 15, 20, 25, and 30 mA. The chronopotentiograms exhibit a double-plateau shape. The first plateau occurs near -1.55 V (vs. Ag+|Ag reference) corresponding to the reduction potential of U^{3+}. The second plateau occurs at the reduction potential of Li^+, approximately -2.5V. The absence of a plateau near the reduction potential of U^{4+} (approximately -0.4V) indicates that only U^{3+} ions are being reduced. A linear relationship was observed between the inverse of the square root of the transition time and the applied driving current, as shown in Figure 83. This suggests that the reduction process is reversible and diffusion-controlled. Therefore, the Sand equation may be used to calculate the diffusion coefficient of U^{3+} ions in LiCl-KCl. Assuming a three electron transfer, a diffusion coefficient was calculated for each of the chronopotentiograms and an average was taken. The resulting value was 7.79×10^{-6} cm^2/s. This compares well to literature values which range from 3.17×10^{-5} to 8.70×10^{-6} cm^2/s [44], [45], [49].

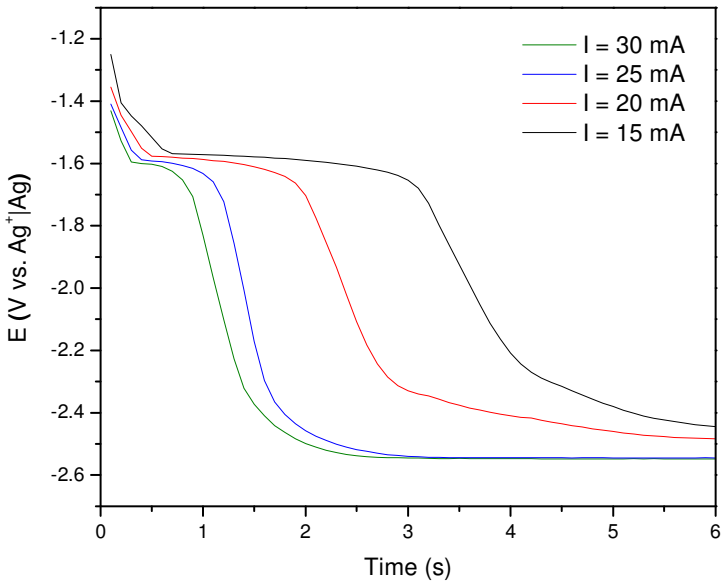

Figure 82. Chronopotentiograms obtained from the UCl_3-LiCl-KCl salt (1 wt% UCl_3) for driving currents of 15, 20, 25, and 30 mA.

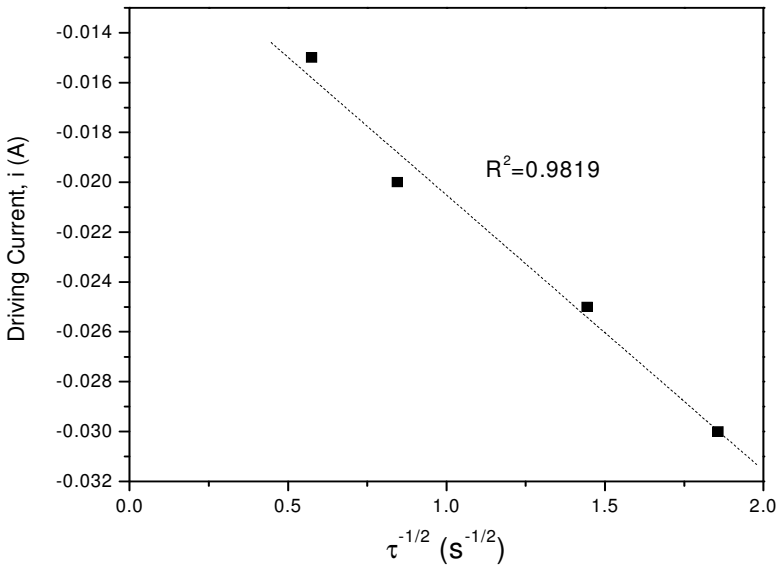

Figure 83. Driving current as a function of the inverse of the square root of the transition time for chronopotentiograms taken from LiCl-KCl containing 1 wt% UCl_3 at 500°C.

Anodic stripping voltammetry was also performed on the LiCl-KCl-UCl_3 salt. Figure 84 shows the anodic stripping voltammograms obtained from the 1 wt% UCl_3 salt at 500°C. The large stripping

peaks were well-defined and occurred at an average voltage of -1.3722 V ± 0.0112 V and had an average peak height of 0.1258 A ± 0.0175 A. The small uncertainty in the peak height measurement indicates that ASV would serve well as a concentration-detection method. However, the uncertainty is likely to increase with uranium concentration. A noisy signal on the right side of the peak indicates complications in the oxidation process. This could be the results of too much uranium being plated onto the working electrode in the pre-concentration step. If this phenomenon is exacerbated at higher concentrations, like was seen with the dysprosium study, thought should be given to decreasing the plating time of the pre-concentration step to reduce the amount of material that is reduced onto the electrode.

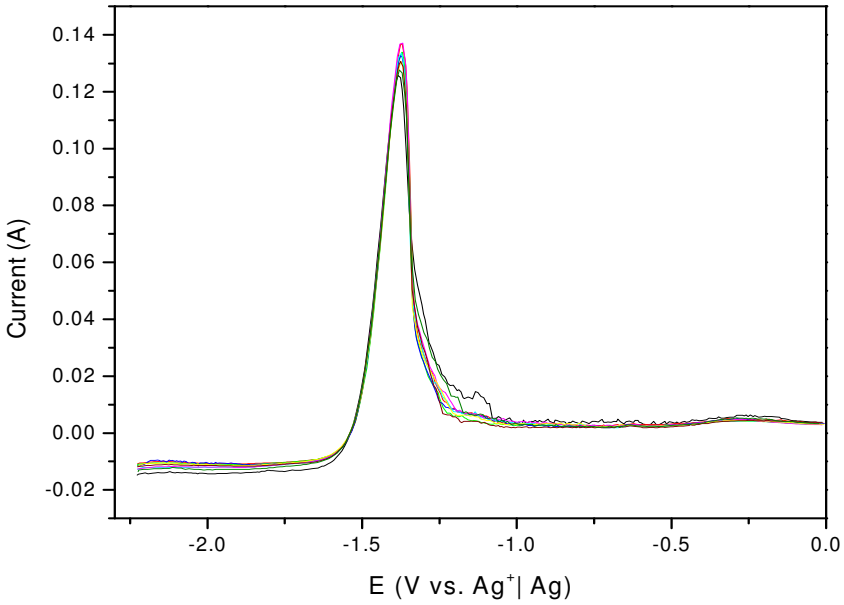

Figure 84. Anodic stripping voltammograms obtained from LiCl-KCl containing 1 wt% UCl_3 at 500°C.

5.1.6 Discussion of Electrochemical Results

5.1.6.1 Ionic Diffusion Coefficients in LiCl-KCl

Studies investigating the diffusion coefficient of La, Ce, Nd, Dy, and U ions have shown that the diffusion coefficient tends to decrease slightly with increasing ionic concentration. It is theorized that this behavior is caused by the increased interaction between the liked-charged ions at higher concentrations. In order to investigate this theory further, the measured diffusion coefficients were plotted as a function of ionic potential, Z/r. This data is shown in Figure 85. Ionic potential is the ratio of the electric charge to the radius of the ion. Ionic potential serves as a means to quantify the charge density of the ion and therefore gives a sense of how strongly the ion will be attracted to or repel other ions. Figure 85 shows the measured diffusion coefficients for La, Ce, Nd, Dy, and U ions in red. This data can also be found in Table XII. All measured diffusion coefficients were obtained from LiCl-KCl containing 1 wt% metal chloride concentration at 500°C. Diffusion coefficients for various other metal ions taken from literature [53] are also plotted in Figure 85. These elements are also listed in Table XIII. Observing Figure 85, it can be seen that there is a slight decrease in the diffusion coefficient as the potential of the ions increases. Measured values for the diffusion coefficient fit in very well with the trend of the literature data. This

supports the theory that increasing increased ionic interaction has an effect on the diffusion coefficient, since ions with higher ionic potential tend to have lower diffusion coefficients.

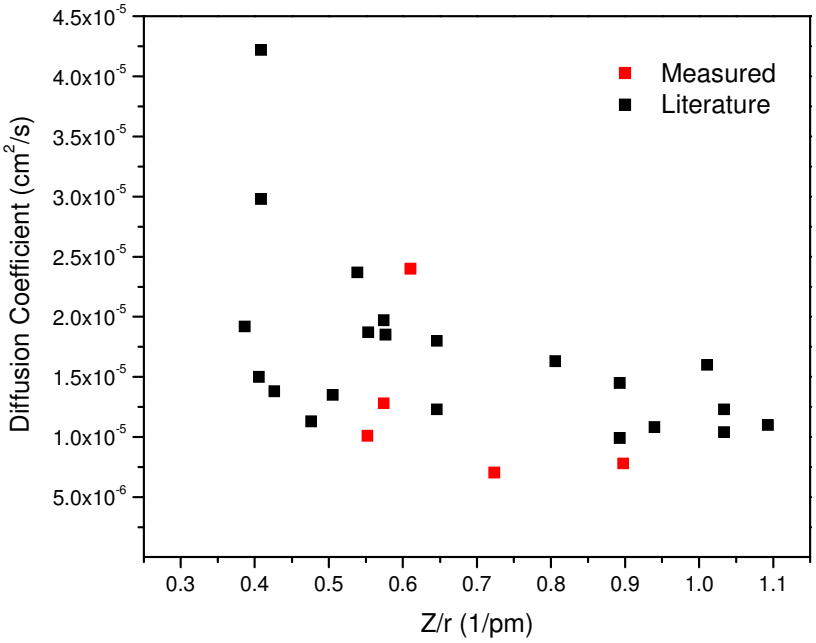

Figure 85. Diffusion coefficients of several ions as a function of their ionic potential, Z/r. Measured diffusion coefficients for La, Ce, Nd, Dy, and U are shown in red and were all taken from 1wt% data (see Table XII). Black points are literature values for various other elements which are shown in Table XIII [53].

Table XII. Measured diffusion coefficients and ionic potential, Z/r, for several metal ions in LiCl-KCl at 500°C. Diffusion coefficients were all obtained from salt with 1 wt% metal chloride concentration.

Element	Diffusion coefficient (cm^2/s)	Ionic radius, r (pm)	Z	Z/r (1/pm)
La(III)	1.01E-05	103.2	57	0.552
Ce(III)	1.28E-05	101	58	0.574
Nd(III)	2.40E-05	98.3	60	0.610
Dy(III)	7.03E-06	91.2	66	0.724
U(III)	7.79E-06	102.5	92	0.898

Table XIII. Diffusion coefficient for metal ions in LiCl-KCl at 500°C and ionic potential data for various elements plotted in Figure 85 [53].

Element	Diffusion coefficient (cm^2/s)	Ionic radius (pm)	Z	Z/r (1/pm)
Sm(III)	1.23E-05	96	62	0.646
U (III)	1.45E-05	103	92	0.893
Ag(I)	2.98E-05	115	47	0.409
Au(I)	1.85E-05	137	79	0.577
Fe(II)	1.38E-05	61	26	0.426
Ni(II)	1.50E-05	69	28	0.406
Ag(I)	4.22E-05	115	47	0.409
Cd(II)	1.35E-05	95	48	0.505
Pb(II)	1.92E-05	119	46	0.387
Bi(III)	1.63E-05	103	83	0.806
U(IV)	1.04E-05	89	92	1.034
U(III)	9.92E-06	103	92	0.893
U(IV)	1.23E-05	89	92	1.034
Pu(III)	1.08E-05	100	94	0.940
Pu(IV)	1.10E-05	86	94	1.093
Zr(IV)	1.13E-05	84	40	0.476
La(III)	1.87E-05	103	57	0.553
Ce(III)	1.97E-05	101	58	0.574
Sm(III)	1.80E-05	96	62	0.646
Eu(II)	2.37E-05	117	63	0.538
Pa(IV)	1.60E-05	90	91	1.011

5.1.6.2 Concentration Detection Methods

This research has investigated three different electrochemical methods as a means to determine the concentration of certain elements in pyroprocessing salt: ASV, CV cathodic peak, and CV anodic peak. Some thought should be given to effectiveness of each method. Anodic stripping voltammetry utilizes the pre-concentration step, which reduces the ionic species onto the working electrode for 60 seconds prior to the linear voltage sweep. The existence of this step makes ASV best suited for detection of elements at low concentrations. The ASV curves for all the elements exhibit a change in slope near 1 wt%. It is believed that this is due to a change in the surface area of the working electrode. Below 1 wt%, the entire working electrode area is not being covered by the reduced metal species. Above 1 wt %, it is thought that the reduced metal begins to cover the entire wetted area of the electrode and the area begins to increase as additional layers of metal are added. At higher concentrations, it is likely that the reduced metal takes on a dendritic morphology. Dendritic formation of uranium is a well-documented phenomenon [52] and it is not unlikely that the lanthanides would display a similar morphology. The distortion of the ASV curves at high concentration (see section 6.1.3) indicates that the dendritic morphology could be causing complications in the oxidation process of the stripping step. Some dendrites

could be breaking off during the stripping step and therefore their oxidation would not be registered by the potentiostat. This would explain the lower slope of the ASV working curve above 1 wt%. The decreased slope could also be attributed to the reduced metal increasing the resistance between the working electrode and the bulk salt, and therefore decreasing the current efficiency of the oxidation process.

Figure 86 shows the standard deviation of the measured ASV peak current as a function of concentration for La, Ce, Nd, and Dy. A significant increase in the standard deviation is observed at concentrations higher than 2 wt% for all elements. This increase would result in a decrease in the precision of the concentration measurement if ASV was being used as a concentration detection technique. Due to all of these results, it is believed that ASV would best be employed as a concentration detection method for elements that exist at concentrations below 1 wt%.

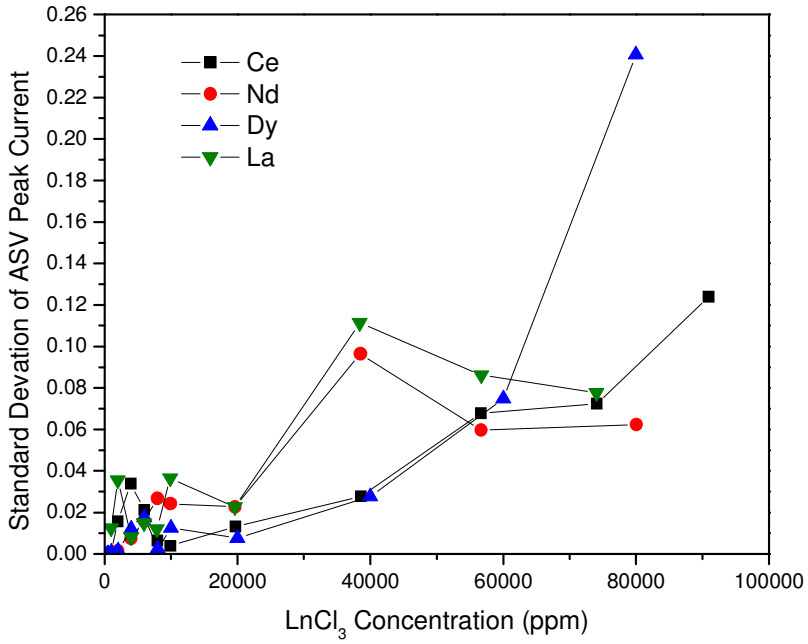

Figure 86. Standard deviation of ASV peak current measurement for La, Ce, Nd, and Dy as a function of concentration.

Alternatively, cyclic voltammetry does not use the initial plating step which seems to plague ASV at high concentrations. As a result, cyclic voltammetry is better suited for detection of elements at concentrations higher than 1 wt%. This is supported by the fact that the CV working curves are much more linear than the ASV working curves. Furthermore, a comparison of the CV anodic and cathodic peaks was made. A linear regression was performed on the anodic and cathodic working curve data for each element. The coefficient of determination, R^2, for each curve is listed in Table XIV. The average coefficient of determination for the anodic and cathodic curves was found to be 0.9470 and 0.9769 respectively. The greater linearity of the cathodic curve indicates that it would serve as the most effective technique for determining the concentration of elements in LiCl-KCl above 1 wt%.

Table XIV. Coefficients of determination for linear fits of the CV anodic and cathodic working curves for various elements.

	Coefficient of Determination	
Element	Anodic	Cathodic
La	0.9414	0.9591
Ce	0.9506	0.9849
Nd	0.9666	0.9796
Dy	0.9295	0.9839
Average	0.9470	0.9769

5.1.6.2 Apparent Standard Potentials

The apparent standard potentials of La, Ce, Nd, and Dy have been determined using this electrochemical cell. This information will be very useful when attempting to selectively extract certain elements from the pyroprocessing salt. The measured apparent standard potentials of these elements in LiCl-KCl at 500°C are listed in Table XV. These values are also compared with values found in literature. Measured values were recorded against a $Ag^{+}|Ag$ (5 mol% AgCl) reference electrode. Measured values were also converted to the chlorine scale for convenience. Differences between measured and literature values can be attributed to differences in experimental conditions and temperature. Also, any impurities in the salt could have an effect on these values.

Since only one concentration of UCl_3 was measured, calculation of the apparent of the apparent standard potential was not performed. Instead, Table XV lists the equilibrium (mid-peak) potentials measured from LiCl-KCl containing 1 wt% UCl_3 at 500°C. The equilibrium potentials for the $U^{3+}|U$, $U^{4+}|U^{3+}$, and adsorption/desorption peaks are listed for various scan rates.

Table XV. Apparent standard potentials of Ln (Ln = La, Ce, Nd, Dy) in LiCl-KCl eutectic at 500°C.

Redox Couple	$E^{0'}_{Ln^{n+}}$ **vs. $Ag^{+}|Ag$ (V)**	$E^{0'}_{Ln^{n+}}$ **vs. $Cl^{-}|Cl_2$ (V)**	**Lit. vs. $Cl^{-}|Cl_2$ (V) ** = 450°C**
$La^{3+}|La$	-1.959	-3.106	-3.146 [11]**
$Ce^{3+}|Ce$	-1.920	-3.066	-3.085 [54]
$Nd^{2+}|Nd$	-1.187	-2.964	-3.073 [11]**
$Nd^{3+}|Nd$	-1.935	-3.081	-3.113 [11]**
$Dy^{3+}|Dy$	-1.958	-3.104	-3.150 [43]**

Table XVI. Equilibrium potentials obtained from cyclic voltammograms of LiCl-KCl containing 1 wt% UCl_3 at 500°C.

	Equilibrium Potential (V vs. Ag+|Ag)		
	$U^{3+}|U$	**$U^{4+}|U^{3+}$**	**ads/des**
25 mV/s	-1.459	-	-

50 mV/s	-1.464	-0.425	-1.074
100 mV/s	-1.471	-0.361	-1.063
150 mV/s	-1.473	-0.366	-1.065
200 mV/s	-1.470	-0.360	-1.059

5.2 Differential Scanning Calorimetry (DSC)

Differential scanning calorimetry (DSC) has been used to analyze the effect of lanthanide chloride and sodium chloride concentration on the melting point of LiCl-KCl eutectic salt. For each of three lanthanide chlorides ($LaCl_3$, $CeCl_3$, $NdCl_3$), the concentration in LiCl-KCl was varied from 0 to 22 mol%. NaCl was studied up to a concentration of 30 mol%.

5.2.1 Sample Preparation and Initial Testing

Preparation of the DSC samples was performed in the electrochemistry glovebox which is maintained with a positive pressure of argon at all times. Approximately 2 grams of pure LiCl-KCl salt was placed in a small glassy carbon crucible along with the desired amount of $LaCl_3$, $CeCl_3$, $NdCl_3$, or NaCl. Three of these crucibles were then placed inside an alumina and stainless steel crucible inside the electrochemistry furnace inside the glovebox. The samples were heated to 500°C and maintained that temperature for 2 hours. Then, the samples were allowed to cool until they solidified before being heated to 500°C for another 2 hours. This heating process was used for all samples to help ensure proper mixing and the creation of a homogeneous sample. After the melting process, the samples were removed from the glassy carbon crucibles and placed into plastic bags in order to transport them to the DSC. The samples were then removed from the bags and a razor blade was used to remove <10 mgs of salt from the side of the larger sample ingot. Salt was removed from approximately the same location on every sample. The <10 mg of salt was then placed inside the aluminum DSC sample pan which was then closed and placed inside the DSC.

Initially, there were two main concerns with sample preparation processes: sample homogeneity and contact with the air. Since less than10 mg of salt is removed from the larger (~2g) sample ingot, it is important that the milligram sample be representative of the larger sample. Therefore, it must be confirmed that all samples are well-mixed and homogeneous. In order to test homogeneity of the samples, a coffee grinder was used to pulverize previously prepared samples. The ground samples were then placed back into the glassy carbon crucibles and re-melted. DSC scans were performed of the once-mixed and twice-mixed samples. No significant difference was apparent, so it was concluded that one melting process was enough to create a homogenous sample.

During the sample preparation process, the salt comes into contact with the air for a short period of time before it is sealed in the DSC sample pan. Because of this, initially there were concerns that the water absorbed from the atmosphere would affect the DSC results of the salt. In order to test this, a salt sample that was left in contact with the air for approximately 10 minutes was analyzed in the DSC and there was no significant difference between this sample and a sample prepared in the normal manner. Figure 87 shows the DSC scan of pure LiCl-KCl salt with 99+% purity and Figure 88 shows the DSC scan of pure LiCl-KCl after it was left in contact with air for a approximately 10 minutes. Both scans only show one endothermic peak in the temperature range of the scan (300-500°C) and the onset points of the peaks are 355.58°C and 354.18°C for the dry and wet samples respectively. Since there is no significant difference in the melting point of these samples, it can be confirmed that the small time the DSC samples

are exposed to atmosphere does not have a significant effect on the DSC analysis. Further investigation of a pure LiCl-KCl sample left in contact with air for 10 minutes showed multiple dehydration peaks occurring between 100 and 200°C (see Figure 89). When the same exact sample was re-tested in the DSC over the same temperature range, the dehydrations did not appear, indicating that all water is removed from the sample once the sample is heated above approximately 250°C.

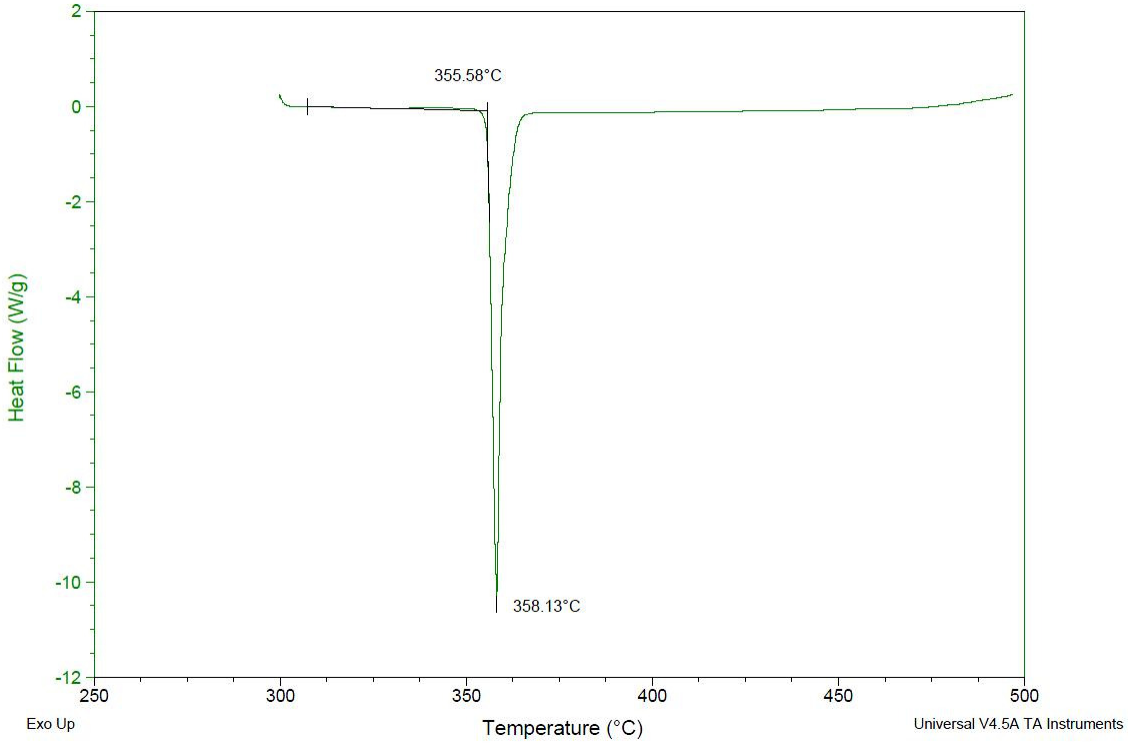

Figure 87. DSC scan of pure LiCl-KCl (99+% purity).

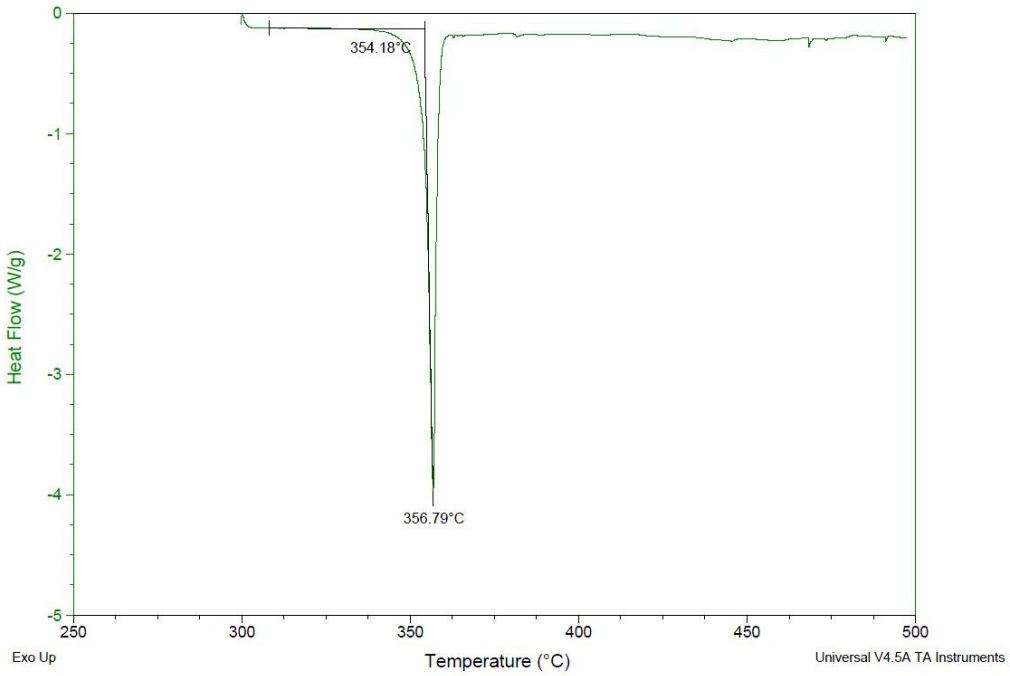

Figure 88. DSC scan of pure LiCl-KCl left into contact with air for 10 minutes.

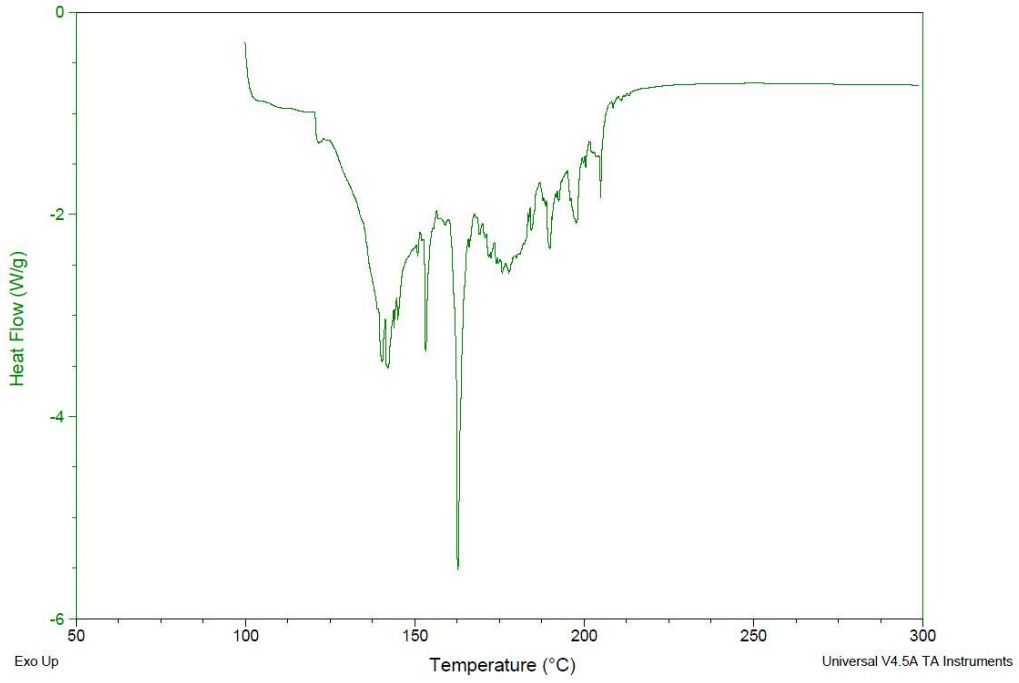

Figure 89. DSC scan from 100-300°C of pure LiCl-KCl left into contact with air for 10 minutes.

5.2.2 $CeCl_3$ Concentration Study

Differential scanning calorimetry was performed on LiCl-KCl eutectic salt containing $CeCl_3$ concentrations of 0-22 mol%. All DSC scans were performed from 300°C to 500°C at 10°C/min. All sample weights were less than 10 mg. Figure 90 shows DSC heating curves of LiCl-KCl containing 1, 10, 14, and 18 mol% $CeCl_3$. At 1 mol% $CeCl_3$, only one endothermic peak is visible, which occurs at the melting point of the pure salt (~353°C). At 10, 14, and 18 mol% $NdCl_3$ a second endothermic peak is visible at a higher temperature. As the concentration of $CeCl_3$ increases, this second peak becomes more defined and shifts to higher temperatures. At 10 mol%, the second peak is short and broad and the peak temperature occurs at 430.60°C. At 18 mol%, the peak is much taller and has shifted to 453.84°C. In addition, as the $CeCl_3$ concentration is increased, the height of the first endothermic peaks decreases significantly. However, this peak does not shift temperature or change shape significantly. At 20 mol%, the first endothermic peak shifts dramatically up to approximately 418°C. A comparison of the 18 and 20 mol% samples are shown in Figure 91.

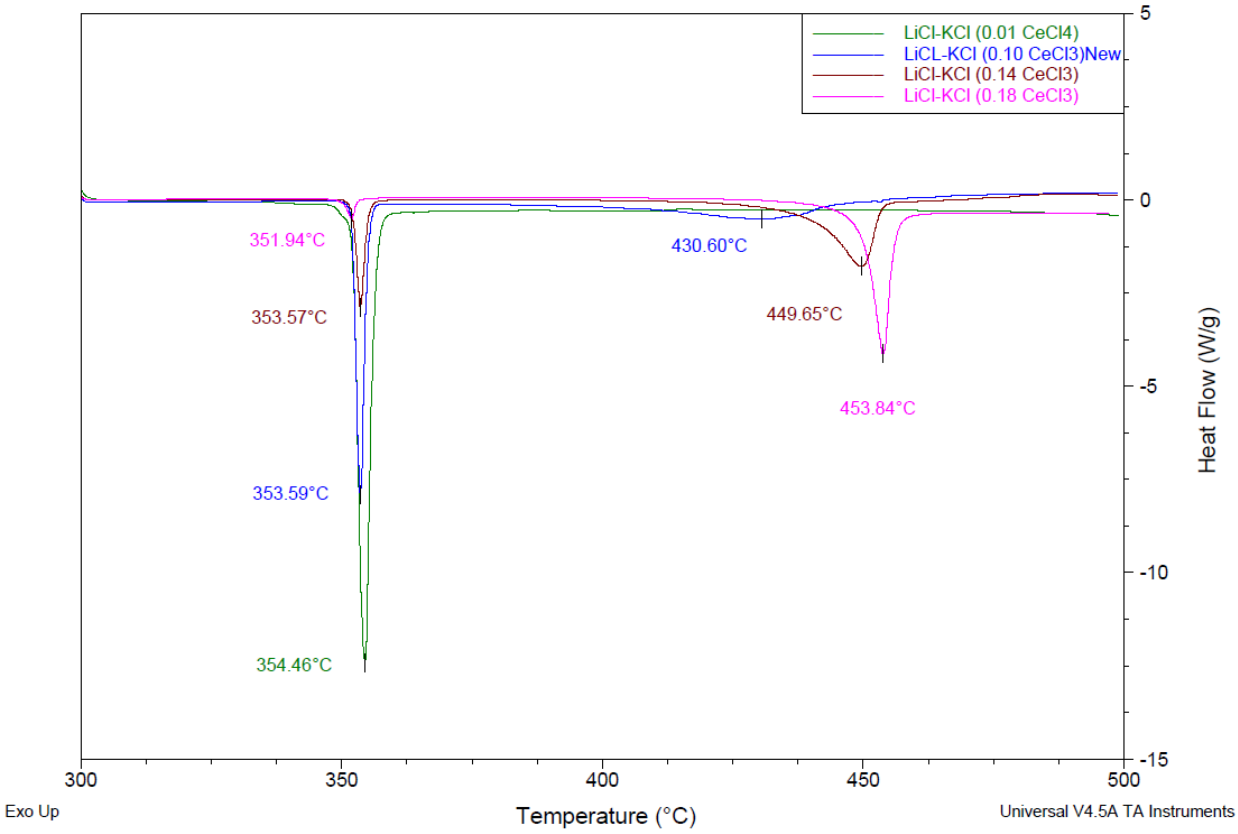

Figure 90. DSC scans of LiCl-KCl containing 1, 10, 14, and 18 mol% $CeCl_3$.

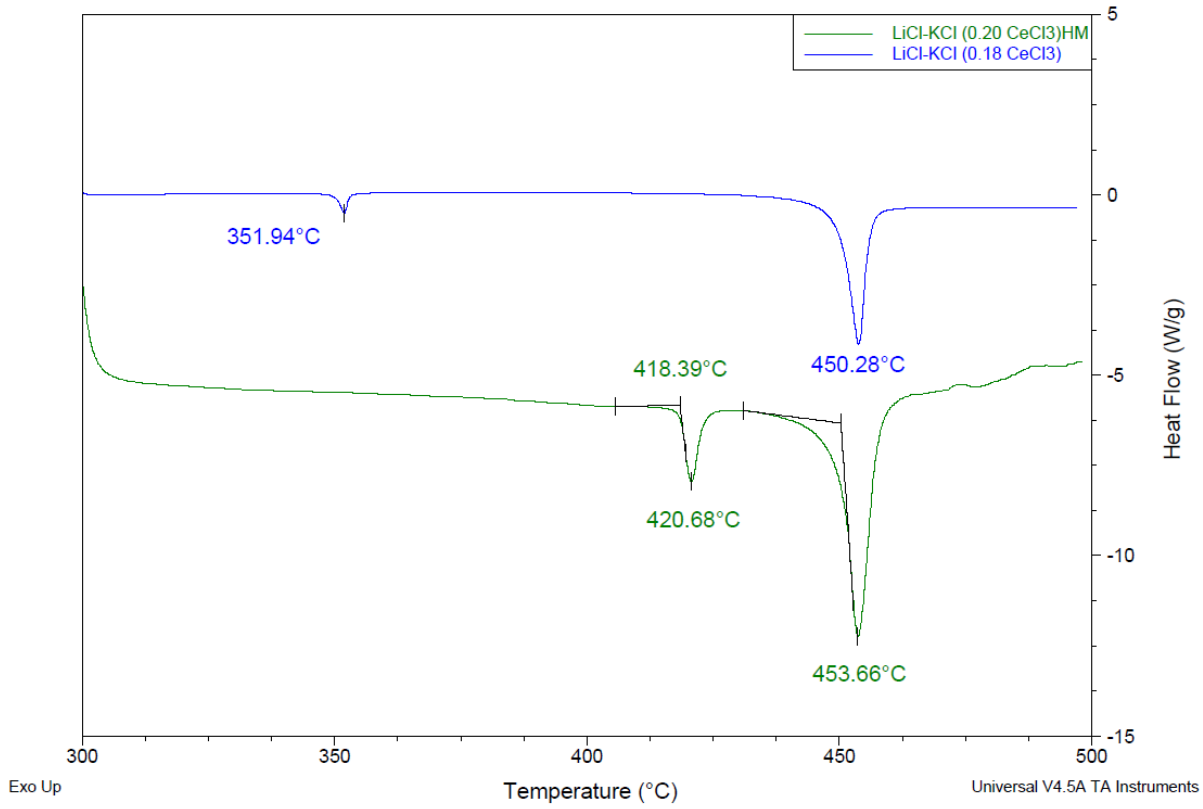

Figure 91. DSC scans of LiCl-KCl containing 18 and 20 mol% $CeCl_3$.

The DSC heating curves at various $CeCl_3$ concentrations can be used to construct a pseudo-binary phase diagram of LiCl-KCl eutectic and $CeCl_3$ system. Since the DSC heating curves only contain two endothermic peaks, the extrapolated onset temperature of the lower temperature peak is used as the solidus temperature and the peak temperature of the higher temperature peak is used as the liquidus temperature as shown in Figure 92.

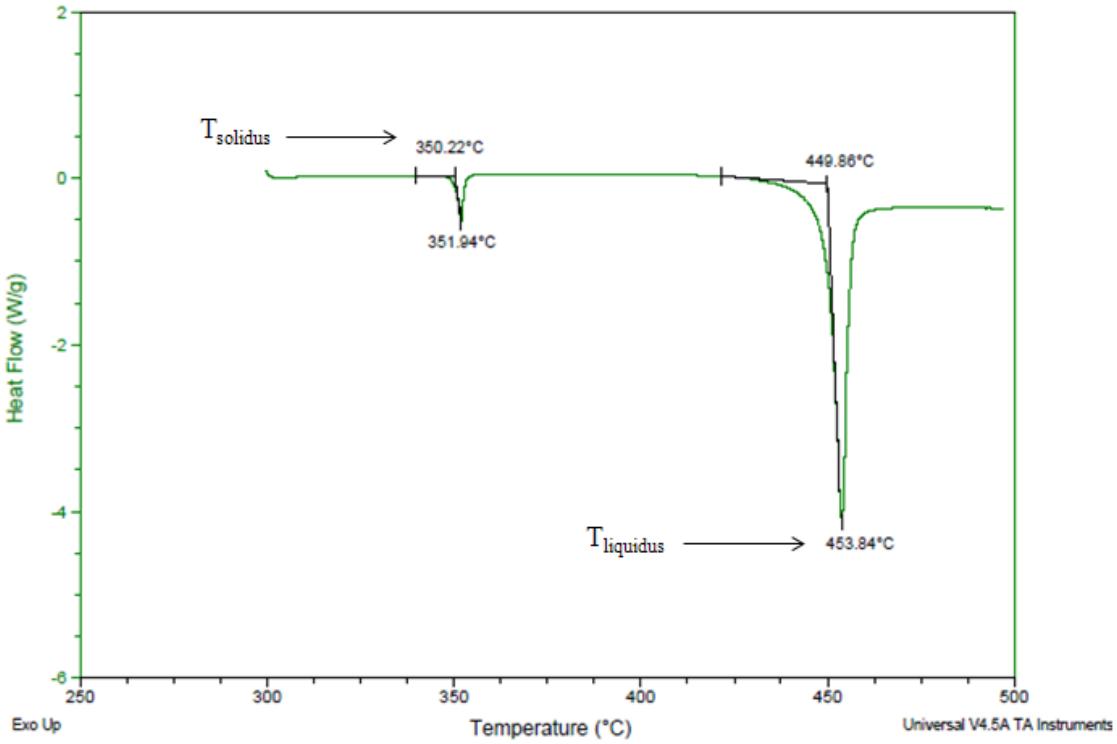

Figure 92. DSC scan of LiCl-KCl-$CeCl_3$ salt containing 18 mol% $CeCl_3$. The onset temperature of the first endothermic peak (350.22°C) defines the solidus temperature and the peak temperature of the second peak (453.84°C) defines the liquidus temperature.

Figure 93 shows the pseudo-binary phase diagram of LiCl-KCl eutectic and $CeCl_3$ constructed from DSC heating curves. The liquidus line increases with $CeCl_3$ concentration up to maximum of approximately 727 K between 18 and 20 mol %. Below 6 mol%, no second endothermic peak representing the liquidus temperature was distinguishable on the DSC heating curves. The solidus line shifts upward from 625 K to 692 K between 18 and 20 mol%. The measured data compares reasonably well to data obtained by Nakumura and Kurata [50] shown on the right in Figure 93. They observed a similar increase in the solidus temperature to 691 K at 17 mol%. To investigate this shift of the solidus line, Nakamura and Kurata performed XRD analysis of LiCl-KCl-$NdCl_3$ samples and determined that below 17 mol%, LiCl, KCl, and K_2NdCl_5 were present. However, above 17 mol%, only LiCl and K_2NdCl_5 were detected. They attribute this shift in composition to be the cause of the increase in the temperature of the solidus line.

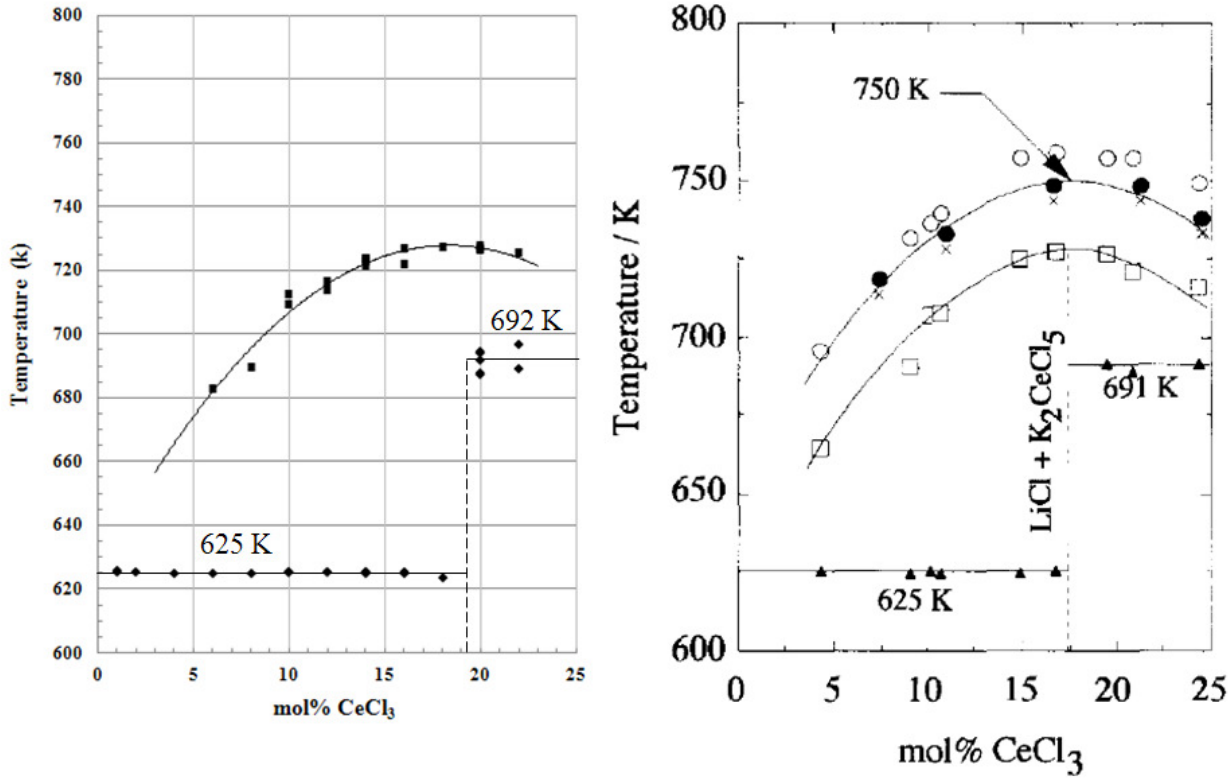

Figure 93. Partial pseudo-binary phase diagram of the LiCl-KCl-$CeCl_3$ system constructed from DSC scans (left) and from literature [50] (right).

In addition, Nakamura and Kurata observed a slightly higher peak temperature of the liquids line due to the existence of a third, very small endothermic peak. This third peak was not initially apparent on DSC scans conducted for this research, so either Nakamura and Kurata observed a spurious peak or a difference in experimental conditions was responsible for the different results. In attempt to find this third endothermic peak, addition DSC analysis was performed utilizing cooling curves knowing that they can be more sensitive to certain transitions [40]. Samples were allowed to cool from 500°C to 300°C at 10°C/min. Figure 94 shows heating and cooling curves for an 8 mol% $CeCl_3$ sample. The heating curve shows two peaks with the second being very short and broad. On the other hand, the cooling curve exhibits three peaks. It is important to note that the peaks on the cooling curves are shifted to lower temperatures due to super cooling effects. Therefore, cooling curves should not be used to define the true thermal transitions temperatures, but rather should be used to support the existence of peaks on the heating curve. The existence of three peaks on the cooling curve was not found for all concentrations. Due to this, and the fact that the true temperature of the transition was not known because no evidence of a third peak was found on the heating curves, the "third-peak" thermal transitions will be omitted from the phase diagrams. Nakamura and Kurata used a slower heating rate of 1°C/min for their DSC analysis. It is possible that the increased resolution caused by the lower scan rate allowed them to discern two separate peaks from what appears to be a single peak at a scan rate of 10°C/min. However, further analysis at slower scan rates would be needed to confirm this theory. For the three-peak case, Nakamura and Kurata defined the transitions for the three peaks (see Figure 94) as shown below. For the case of the two-peak melting process observing for the majority of this research, the melting of LiCl and K_2CeCl_5 appear as a single peak.

A: $K_2CeCl_5 + LiCl + KCl \leftrightarrow K_2CeCl_5 + LiCl + L$

B: $K_2CeCl_5 + LiCl + L \leftrightarrow K_2CeCl_5 + L$

C: $K_2CeCl_5 + L \leftrightarrow L$

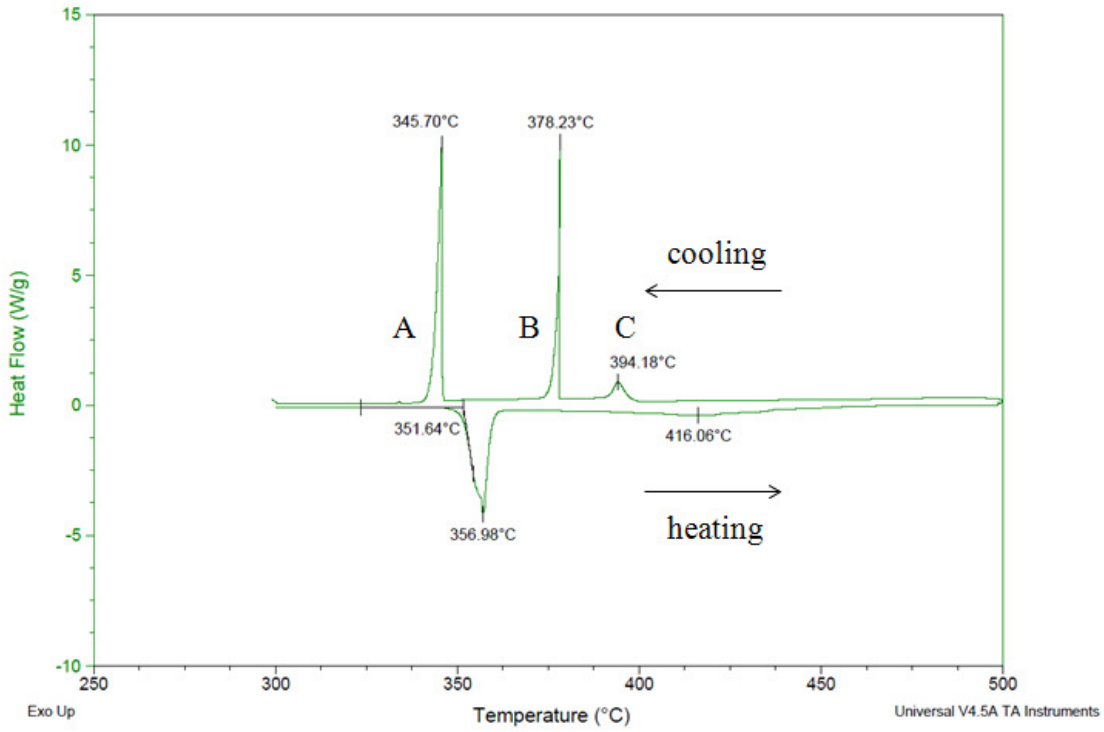

Figure 94. DSC heating and cooling curves obtained from LiCl-KCl eutectic containing 8 mol% $CeCl_3$. Heating and cooling rates were both 10°C/min.

5.2.3 $NdCl_3$ Concentration Study

Similar to the $CeCl_3$ study, DSC analysis was performed on LiCl-KCl eutectic salt containing $NdCl_3$ concentrations of 0-22 mol%. Once again, all DSC scans were performed from 300°C to 500°C at 10°C/min. All sample weights were between 5 and 10 mg. Figure 95 shows a DSC scans of LiCl-KCl containing 1, 10, 14, and 18 mol% $NdCl_3$. Similar to $CeCl_3$, the second endothermic peak shifts to higher temperature and becomes more defined as the concentration of $NdCl_3$ is increased. In addition, the peak height of the first endothermic peak decreases with increasing $NdCl_3$ concentration, but the temperature or shape of the peak does not change to any significant degree.

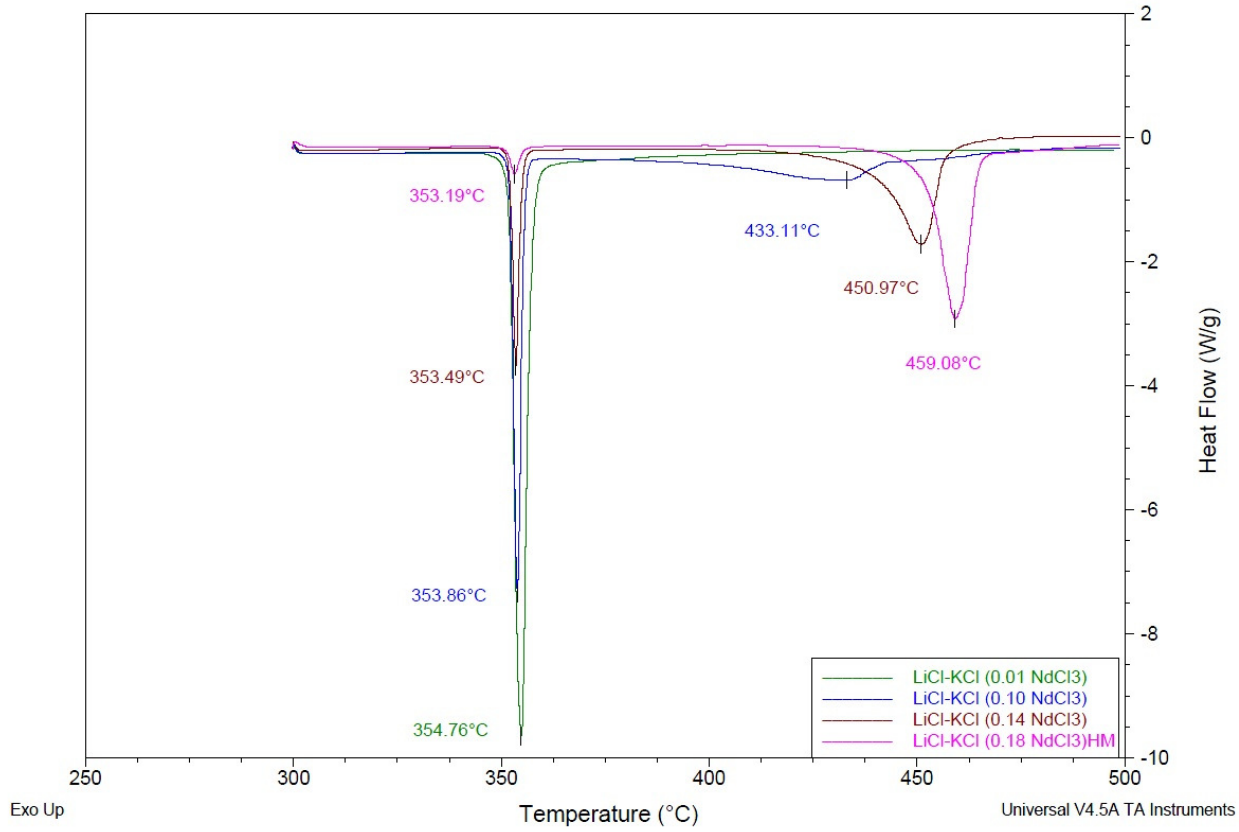

Figure 95. DSC scans of LiCl-KCl containing 1, 10, 14, and 18 mol% $NdCl_3$.

A pseudo-binary phase diagram of the LiCl-KCl-$NdCl_3$ system was constructed from the $NdCl_3$ DSC scans utilizing the same methods used for the $CeCl_3$ samples. Figure 96 compares the measured LiCl-KCl eutectic and $NdCl_3$ phase diagram with a similar diagram from literature [50]. The liquidus line increases with $NdCl_3$ concentration up to maximum of approximately 733 K near 20 mol %. Below 8 mol%, only one endothermic peak existed on the DSC heating curves. The solidus line shifts upward from 625 K to 670 K between 20 and 22 mol%. Nakamura and Kurata observed a smaller increase in the solidus temperature to 656 K at 17 mol%.

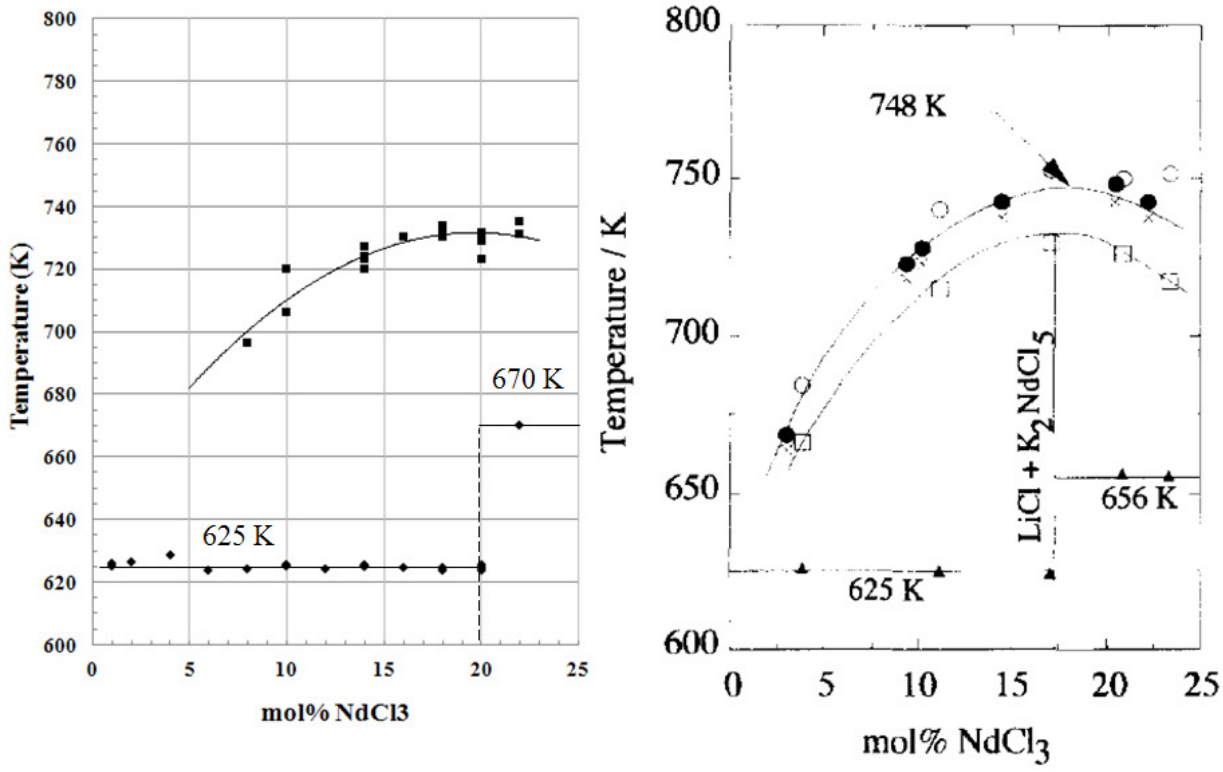

Figure 96. Partial pseudo-binary phase diagram of the LiCl-KCl-$NdCl_3$ system constructed from DSC scans (left) and from literature [50] (right).

5.2.4 $LaCl_3$ Concentration Study

LiCl-KCl samples containing $LaCl_3$ (0-22 mol%) were also investigated with DSC. Once again, all DSC scans were performed from 300°C to 500°C at 10°C/min. All sample weights were between 5 and 10 mg. Figure 97 shows DSC scans of LiCl-KCl containing 1, 10, 14, and 18 mol% $LaCl_3$. As with previous studies, the second endothermic peak shifts to higher temperature and becomes more defined as the concentration of $LaCl_3$ is increased. At 10 mol%, the peak occurs at 426.39°C and at 18 mol% the peak has shifted to 453.49°C. In addition, the peak height of the first endothermic peak decreases with increasing $LaCl_3$ concentration. The shape of the peaks remained sharp and the temperature of the peak only decreased 3.5°C from 1 to 18 mol%.

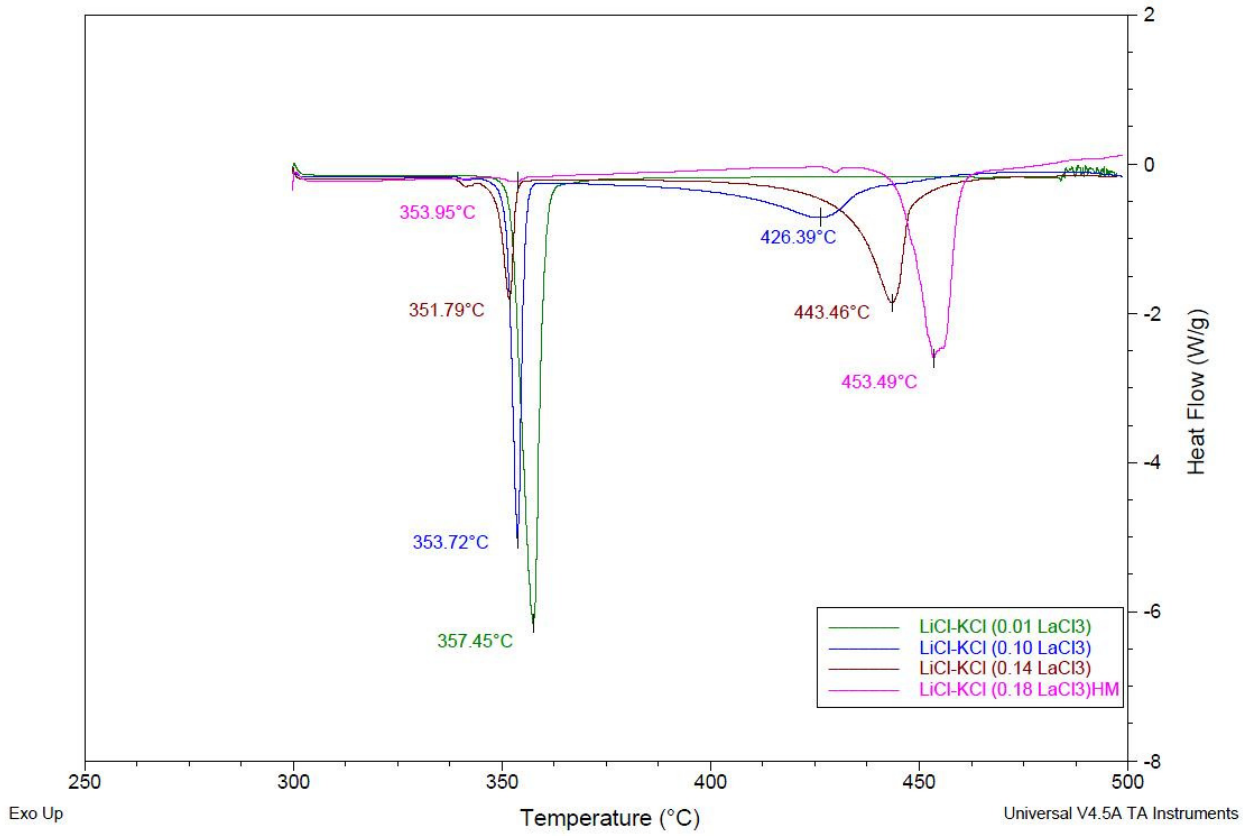

Figure 97. DSC scans of LiCl-KCl containing 1, 10, 14, and 18 mol% $LaCl_3$.

The pseudo-binary phase diagram of the LiCl-KCl-$LaCl_3$ is shown in Figure 98 along with literature data from Nakamura and Kurata [50]. $LaCl_3$ samples were found to exhibit similar behavior to $CeCl_3$ and $NdCl_3$. The liquidus line increases with $LaCl_3$ concentration up to maximum of approximately 726 K between 18 and 20 mol %. Below 6 mol%, only one endothermic peak existed on the DSC heating curves. The solidus line shifts upward from 625 K to 700 K between 20 and 22 mol%. Nakamura and Kurata observed a similar increase in the solidus temperature to 701 K at 17 mol%.

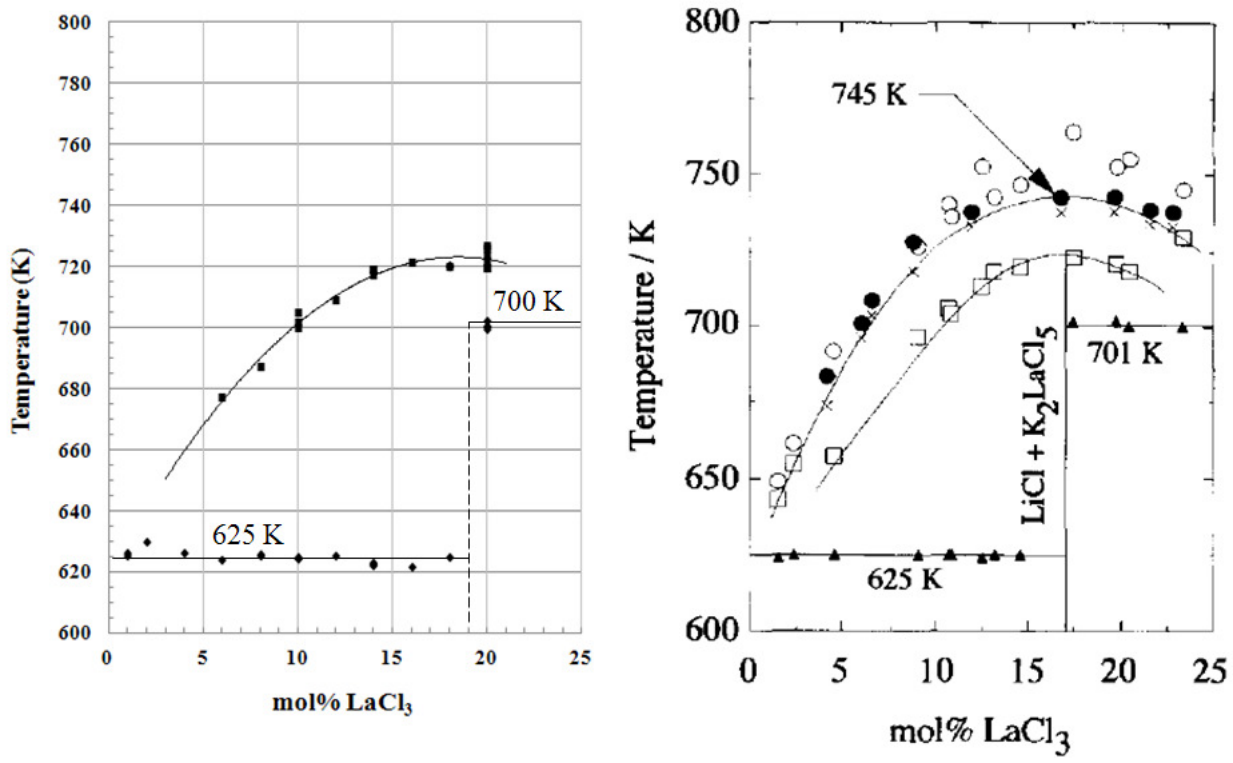

Figure 98. Partial pseudo-binary phase diagram of the LiCl-KCl-$LaCl_3$ system constructed from DSC scans (left) and from literature [50] (right).

5.2.5 NaCl Concentration Study

The last element investigated with differential scanning calorimetry was sodium chloride. Sodium accumulates in the salt since it was used as a thermal bond material in EBR-II fuel. Therefore, it is important to study the effect that NaCl concentration has on the melting point of the pyroprocessing salt. In accordance with previous studies, all DSC heating and cooling rates were 10°C/min and sample masses were all less than 10 mg. Figure 99 shows a DSC scan of LiCl-KCl containing 12 mol% NaCl. Both the heating and cooling curves exhibit one clear thermal transition peak. The onset temperature of the melting peak is at 352.27°C. NaCl concentrations from 1-30 mol% have been investigated and all scans exhibit only one clear endothermic peak. Figure 100 shows a plot of the onset temperature of this endothermic peak as a function of the NaCl concentration.

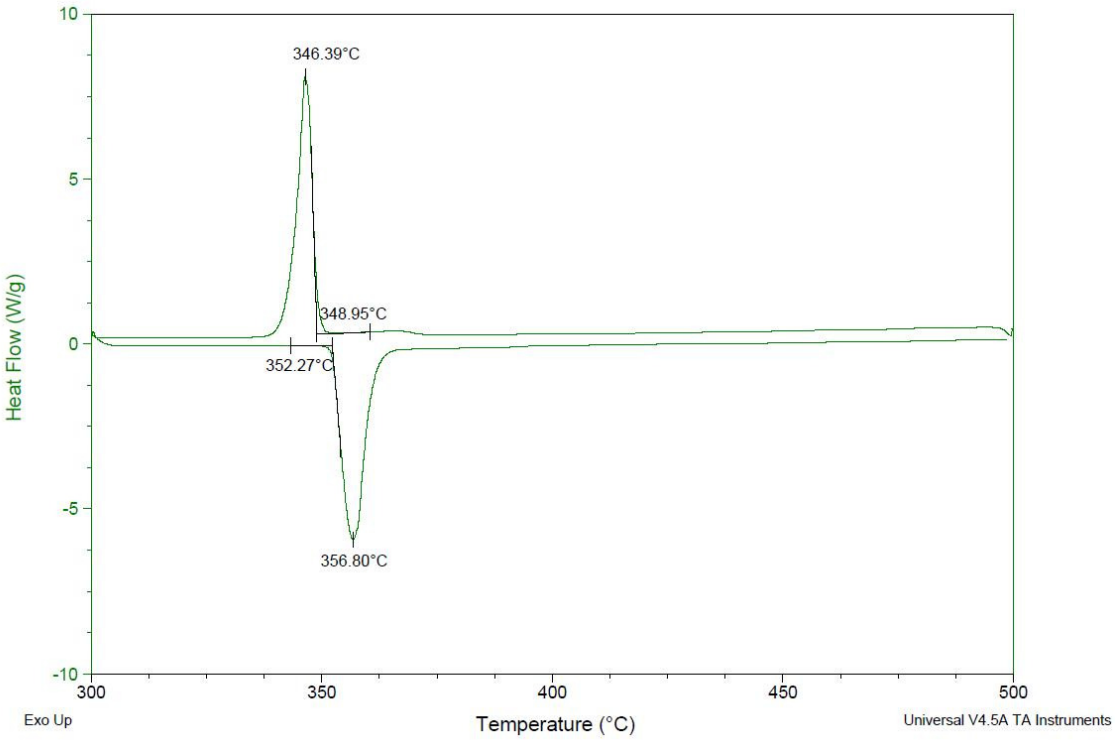

Figure 99. DSC scan of LiCl-KCl containing 12 mol% NaCl.

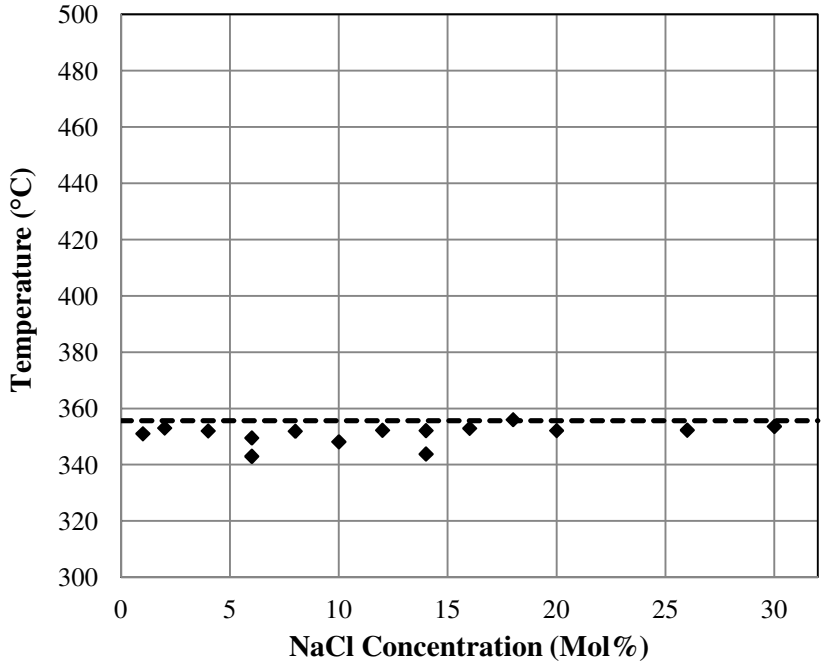

Figure 100. Onset temperature of the endothermic peak from LiCl-KCl-NaCl salt samples as a function of NaCl concentration. Data was compiled from DSC scans. The dotted line represents the melting point of pure LiCl-KCl.

The results in Figure 99 and Figure 100 and suggest that concentrations of NaCl up to 30 mol% do not affect the melting point of LiCl-KCl. However, this finding contradicts a study by Gutknecht [40] who observed significant increases in the liquidus temperature of the salt as a function of NaCl concentration. The liquidus temperature was reported to increase from 383.44°C at 10 mol% to 498°C at 30 mol%. However, in addition to LiCl, KCl, and NaCl, the salt samples used in Gutknecht's study contained other elements ($SrCl_2$, CsCl, $BaCl_2$, $LaCl_3$, $CeCl_3$, $PrCl_3$, $NdCl_3$, $SmCl_3$, and $GdCl_3$) whose effects were not considered. However, Gutknecht's measured data was compared to a model by Sangster and Pelton [51] who calculated the LiCl-KCl-NaCl ternary diagram based on the binary systems. Their data also predicted an increase the LiCl-KCl-NaCl liquidus temperature as a function of NaCl concentration from 379.66°C at 10 mol% to 520.98°C at 30 mol%. These results prompted further inspection of our results to determine whether or not the samples in this study were completely melted after the first endothermic peak observed on the DSC scans. In order to test this, a sample containing 30 mol% NaCl was placed in a quartz crucible and heated in the furnace inside the electrochemistry glovebox. Once the sample temperature reached 400°C, the sample was quickly removed from the heater and observed visually. The sample was mostly clear with a small amount of white solid visible at the bottom of the crucible, indicating that it was in the two-phase region. The sample was then heated to 500°C and observed again. At this temperature, there was still a very small amount of white solid visible at the bottom of the crucible indicating that the sample had not completely melted. Therefore, it can be concluded that the endothermic peak observed on the DSC scans represents the onset temperature of melting. This suggests that there is an additional endothermic transition which defines the liquidus temperature of the LiCl-KCl-NaCl system. Clear evidence of this transition has yet to found on the DSC scans. Recent contamination issues with the DSC have caused poor baseline heat flow measurements for several samples, which could be hiding small endothermic peaks which define the liquidus temperature.

In addition, it is possible that LiCl-KCl-NaCl samples are not being completely mixed and the small amount of salt being analyzed in the DSC only consists of LiCl-KCl eutectic. Further analysis should be performed to confirm the homogeneity of the LiCl-KCl salt samples. In addition, further DSC analysis is warranted in attempt to define the liquidus temperature. Varying scan rates and sample sizes may help to resolve the additional thermal transition peaks.

5.3 Molten Salt Density

The density of LiCl-KCl eutectic salt was studied as a function of $LnCl_3$ (Ln = La, Ce, Nd) concentration up to 13 wt%. Lanthanide chlorides accumulate in the electrorefiner salt as more fuel is processed and it is important to know how they affect the density of the salt which is used to calculate the salt mass. An accurate record of salt mass is necessary to reduce proliferation concerns.

Density measurements were made at lanthanide chloride concentrations of 5, 9, and 13 wt%. The bob was cleaned thoroughly with acetone and water before each measurement. Measurement of the bob volume was also performed before each measurement. Multiple density measurements were made at each concentration to ensure proper mixing of the salt and good agreement of the density values. The density of pure LiCl-KCl was measured and found to be 1.6130 g/cm^3 which was in good agreement to a literature value of 1.6213 g/cm^3 [34].

Figure 101 shows the measured and calculated salt density of LiCl-KCl-$LnCl_3$ (Ln=La, Nd) salt at 500°C as a function of $LnCl_3$ concentration. The calculated salt data is based on a model proposed by Mariani and Vaden [34]. The model uses the standard calculation for the density of a multi-component fluid which is shown below where the overall fluid density, $\rho_{salt,\ calc}$, can be determined from the sum of the ratio of the weight fraction of each component, w_i, to its pure density, ρ_i.

$$\frac{1}{\rho_{salt,\ calc}} = \frac{w_{LiCl}}{\rho_{LiCl,500°C}} + \frac{w_{KCl}}{\rho_{KCl,\ 500°C}} + \frac{w_{LnCl_3}}{\rho_{LnCl_3,\ 500°C}}$$

In addition, Mariani and Vaden applied a correction factor, k, to the densities of the metal chlorides to account for non-ideal behavior. The densities of metal chlorides at 500°C were calculated using the equation below Where A, B, and C are the parameters from Table VIII and t is the temperature in Celsius.

$$\rho = kA + B(C + t)$$

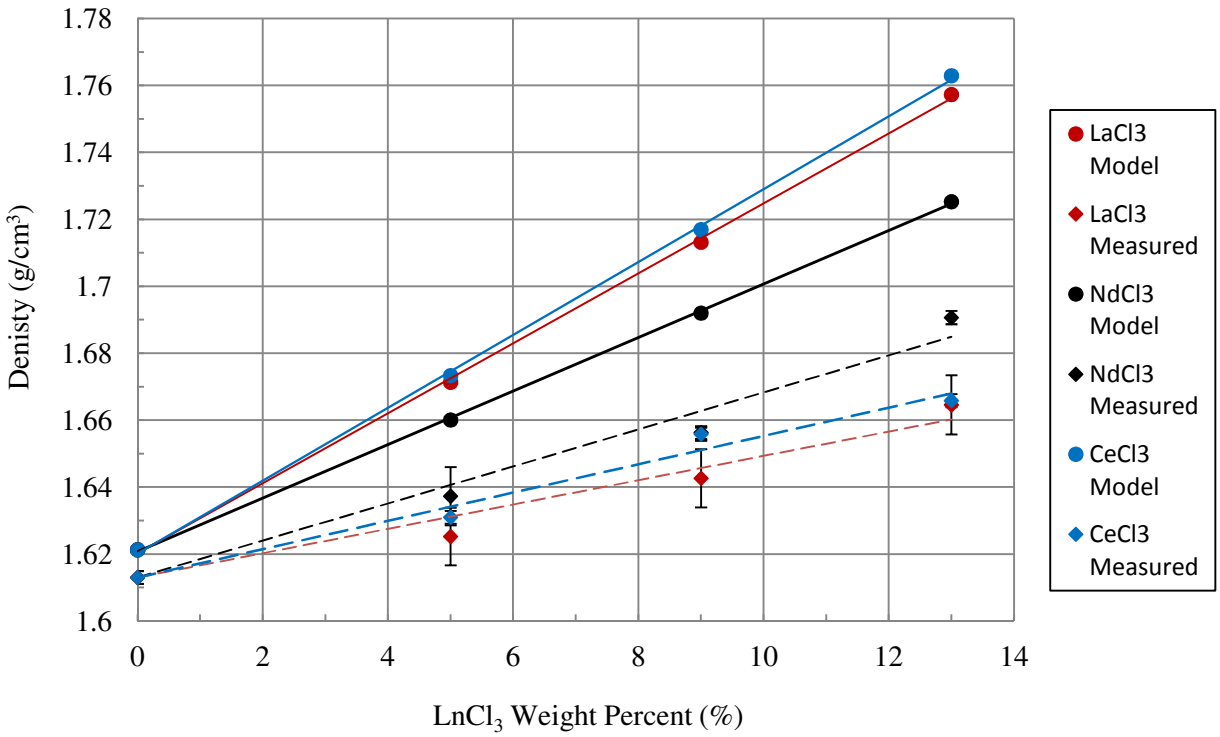

Figure 101. Measured and calculated LiCl-KCl-$LnCl_3$ molten salt density as a function of $LnCl_3$ (Ln=La, Nd) concentration at 500°C.

The linear fits of the measured data are listed below where ρ is the density of the LiCl-KCl-$LnCl_3$ salts in g/cm^3 and C_{LnCl3} is the concentration of the lanthanide chloride species in weight percent. The linear fits were forced to have a y- intercept of 1.6130 g/cm^3, the measured density of pure LiCl-KCl and the correlation coefficients were 0.9731, 0.9785, and 0.9580 for $NdCl_3$, $CeCl_3$, and $LaCl_3$ respectively.

$$\rho_{LiCl-KCl-NdCl3} = 0.0055 \cdot C_{NdCl3} + 1.6130$$

$$\rho_{LiCl-KCl-LaCl3} = 0.0036 \cdot C_{LaCl3} + 1.6130$$

$$\rho_{LiCl-KCl-CeCl3} = 0.0042 \cdot C_{CeCl3} + 1.6130$$

The density data presented in Figure 101 is also shown in Table XVII. Percent differences between the measured and modeled data are listed for each concentration. The standard deviation of the measured density was determined by propagating the uncertainty in the bob weights and bob volume.

Table XVII. Measured and calculated density values. Percent differences between measured and calculated values are listed as well as the error of the measured values.

Concentration (wt %)	Density (g/cm^3) model	Density (g/cm^3) measured	Percent Difference	Measured Error (g/cm^3)

				(%)	
$LaCl_3$	0	1.6213	1.6130	0.51	0.0019
	5	1.6521	1.6253	1.63	0.0086
	9	1.6939	1.6427	3.02	0.0087
	13	1.7379	1.6646	4.22	0.0089
$NdCl_3$	0	1.6213	1.6130	0.51	0.0019
	5	1.6411	1.6373	0.23	0.0087
	9	1.6732	1.6563	1.01	0.0019
	13	1.7066	1.6907	0.93	0.0020
$CeCl_3$	0	1.6213	1.6130	0.51	0.0019
	5	1.6541	1.6310	1.40	0.0019
	9	1.6976	1.6558	2.46	0.0019
	13	1.7434	1.6659	4.45	0.0019

The measured data density data is less than the calculated density at all concentrations. So, it appears that $NdCl_3$, $LaCl_3$, and $CeCl_3$ exhibit more non-ideal behavior than UCl_3 which was used to determine the k value used in the model. In addition, the model predicts the $NdCl_3$ density to be the lowest of the three elements while the measured data shows it to be the highest. The reason for this difference is not clear, but it should be noted that the $NdCl_3$ density used in the model was calculated and not measured, so there could be come error associated with that value.

6. Programmatic Discussion

Over the last three years, Mehran Mohammadian and Sean Martin completed their Master's Theses on this work. Jacob Sager has helped with the project over the last year and a half and has now completed his undergraduate degree. He has now begun his graduate studies performing other molten salt research at UW-Madison. Presentations of this research were made at the Fuel Cycle Research and Development (FCRD) conference in Gaithersburg, MD on October 27, 2010 (invited talk) and at the 2012 International Pyroprocessing Research Conference in Fontana, WI on August 28th, 2012. Most recently, Jacob Sager presented this research at the 2012 Materials Science and Technology (MS&T) Conference in Pittsburgh, PA on October 10th, 2012. In addition, poster presentations of this research were made at the 2012 American Nuclear Society Student Conference in Las Vegas, NV and the Nuclear Fuel and Structural Materials Topical Meeting at the 2012 American Nuclear Society Annual Conference in Chicago, IL. A paper detailing this work has been published in the Transactions of the American Nuclear Society and another has been submitted to the Ceramic Transactions Series to accompany the presentation at the MS&T conference. Preparation of four additional papers for submission to relevant journals is underway and should be completed by February 2013. During the course of this project, Dr Michael Simpson and Dr. Supathorn Phongikaroon visited the University of Wisconsin and provided valuable advice and a seminar on related work. Graduate student Sean Martin made two 1-week visits to perform uranium electrochemistry work at the Center for Advanced Energy Studies (CAES) Radiochemistry Laboratory. He worked closely with Prof. Phongikaroon's students from the University of Idaho. The help provided

by CAES and the University of Idaho personnel is gratefully acknowledged. A joint publication between the two institutions on the topic of this project is planned and discussions are underway.

7. Summary

7.1 Electrochemistry

The electrochemistry of LiCl-KCl salt with $LaCl_3$, $CeCl_3$, $NdCl_3$, and $DyCl_3$ additions from 0.1 wt% to 10 wt% were investigated with cyclic voltammetry, chronopotentiometry, and anodic stripping voltammetry. UCl_3 was investigated at 1 wt% only. The electrochemical and thermodynamic parameters of interest were the reaction mechanism, apparent standard potential, the diffusion coefficient, and the activity coefficient; all were extracted through combined use of CV, CP. The peak current density in ASV and CV were plotted against the lanthanide concentration to arrive at a plot that may serve as a basis for the development of an on-line probe for the determination of analyte concentration in the molten salt.

All four lanthanide cations exhibited reversible behavior at the scan rates tested (20, 50, 100, 150, and 200 mV/s), which was important to confirm due to the heavy reliance on reversibility in analytical electrochemical equations. The determination of reaction mechanism was primarily investigated with CV and was confirmed using Nernst plots. Table XVIII lists the reaction mechanisms determined in this work. These reaction mechanisms were confirmed at each concentration investigated, and are in good agreement with literature.

Table XVIII. Reaction mechanisms of the Ln^{n+} half-cell in molten LiCl-KCl eutectic salt.

Cation	Stages	Half-cell reaction
La	Single-step	$La^{3+} + 3e^- \leftrightarrow La$
Ce	Single-step	$Ce^{3+} + 3e^- \leftrightarrow Ce$
Nd	Two-step	$Nd^{3+} + e^- \leftrightarrow Nd^{2+}$ $Nd^{2+} + 2e^- \leftrightarrow Nd$
Dy	Single-step	$Dy^{3+} + 3e^- \leftrightarrow Dy$
U	Two-Step	$U^{4+} + e^- \leftrightarrow U^{3+}$ $U^{3+} + 3e^- \leftrightarrow U$

Diffusion coefficients were determined by the chronopotentiometry technique for each concentration of the four lanthanides studied. Uranium was only studied at one concentration. Table XIX lists the range of diffusion coefficients determined experimentally in this work and compares them to some of the limited values reported in the literature.

Table XIX. Diffusion coefficients of Ln (Ln = La, Ce, Nd) in molten LiCl-KCl eutectic salt at 500°C.

Cation	Diffusion Coefficient Range (cm^2/s)	Literature Values (cm^2/s) ** = 450°C
La	$1.88x10^{-5}$ - $3.93x10^{-6}$ 0.1 wt% - 9.1 wt%	$8.0x10^{-6}$ [11] **
Ce	$2.53x10^{-5}$ - $8.24x10^{-6}$ 0.1 wt% - 7.5 wt%	$1.96x10^{-5}$ [54]
Nd	$2.46x10^{-5}$ - $1.17x10^{-5}$ 0.1 wt% - 5.7 wt%	$1.1x10^{-5}$ [11] **
Dy	$1.33x10^{-5}$ - $4.43x10^{-6}$ 0.2 wt% - 8 wt%	$1.47\ x10^{-5}$ [42]
U	$7.79x10^{-6}$ 1 wt%	$3.17x10^{-5}$ to $8.70x10^{-6}$ [44], [45]

Apparent standard potential was determined through plotting the equilibrium potential, determined via CV, of each concentration measurement against the natural logarithm of the concentration. The intercept of this Nernst plot was defined as the apparent standard potential. The activity coefficient can then be found based on the experimentally determined apparent standard potential. Table XX and Table XXI report this work's calculated apparent standard potentials and activity coefficients, respectively. The apparent standard potentials match very closely with literature values. However, there is a modest difference between the activity coefficient calculated in this work and what is found in the literature. Further investigation of this difference reveals the significant spread in the activity coefficient data for MCl_x in LiCl-KCl in the literature.

Table XX. Apparent standard potentials of Ln (Ln = La, Ce, Nd, Dy) in LiCl-KCl eutectic at 500°C.

Redox Couple	$E^{0'}_{Ln^{n+}}$ vs. $Ag^+|Ag$ (V)	$E^{0'}_{Ln^{n+}}$ vs. $Cl^-|Cl_2$ (V)	Lit. vs. $Cl^-|Cl_2$ (V) ** = 450°C
$La^{3+}|La$	-1.959	-3.106	-3.146 [11]**
$Ce^{3+}|Ce$	-1.920	-3.066	-3.085 [54]
$Nd^{2+}|Nd$	-1.187	-2.964	-3.073 [11]**
$Nd^{3+}|Nd$	-1.935	-3.081	-3.113 [11]**
$Dy^{3+}|Dy$	-1.958	-3.104	-3.150 [43]**

Table XXI. Activity coefficients of Ln (Ln = La, Ce, Nd) in molten LiCl-KCl eutectic salt at 500°C.

Cation	Activity Coefficient	Literature Value ** = 450°C

La	$1.05x10^{-3}$	$5.7x10^{-3}$ [9] **
Ce	$3.03x10^{-3}$	$1.18x10^{-2}$ [10]
Nd	$3.55x10^{-4}$	$8.0x10^{-5}$ [9]**

Another goal of this work was to develop a method in which the concentration of a given lanthanide could be determined through the use of quick, electrochemical techniques, which would help lead to the development of an *in situ* electrochemical probe for on-line monitoring of the electrorefiner. Both ASV and CV were used for this task and both exhibited some regime of a linear relationship in plotting the peak current density as a function of lanthanide concentration. High concentrations (> 1 wt% $LnCl_3$) yielded diminished peak current density responses due to surface saturation effects. This effect was most pronounced with ASV. The anodic CV curve exhibited some surface saturation behavior, but the effect was less severe due to the lack of a plating, or pre-concentration, step. The cathodic CV curve was the most linear and probably the best suited for concentration detection above 1 wt%. On the other hand, ASV would be particularly well-suited for trace concentration studies (perhaps lower than studied here) due to its pre-concentration step. It is common for the electrorefiner salt to accumulate concentrations of lanthanides in concentrations approaching 10 wt%. The CV cathodic curve appears to be well-suited to the task of on-line measurement of lanthanides and fission products. Other, more dilute elements may require ASV for detection.

7.2 Differential Scanning Calorimetry and Density

Differential scanning calorimetry was used to investigate the melting processes of LiCl-KCl containing various concentrations of lanthanide (La, Ce, Nd) and sodium chlorides. $LaCl_3$, $CeCl_3$, and $NdCl_3$ were investigated up to a concentration of 22 mol%. Sodium chloride was investigated up to 30 mol%. DSC data was used to construct pseudo-binary phase diagrams of LiCl-KCl eutectic and lanthanide chlorides. At lanthanide chloride concentrations as low as 6-8 mol%, increases in the melting point of the salt were detectable with DSC analysis. The liquidus temperature of the LiCl-KCl-$LnCl_3$ systems increased with $LnCl_3$ concentration and were all found to reach a maximum near 20 mol%. The maximum liquidus temperatures for the La, Ce, and Nd phase diagrams were found to be 453, 454, and 462°C respectively. DSC analysis of LiCl-KCl-NaCl samples revealed one clear endothermic peak which occurred near the melting point of the pure salt for all NaCl concentrations up to 30 mol%. Visual inspection of the melting process of these samples indicated that the thermal transitions detected with the DSC were the onset temperature of melting. Further DSC analysis is required to determine the liquidus temperature of the LiCl-KCl-NaCl salts.

The densities of LiCl-KCl-$LnCl_3$ (Ln = La, Ce, Nd) salts at 500°C were measured as a function of $LnCl_3$ concentration. $LnCl_3$ concentrations of 5, 9, and 13 wt% were investigated. Measured density values were compared to predicted data from a model by Mariani and Vaden [34]. Percent differences between measured and modeled densities were less than 4.5% at all concentrations. These differences can be resolved by concluding that $LaCl_3$, $CeCl_3$, and $NdCl_3$ exhibit more non-ideal behavior than UCl_3 which was used to create the model. In addition, experimental error and incomplete mixing of the salt could contribute to the difference between the measured and calculated density values.

8. References

[1] SOLOMON, BARRY D. “High-level radioactive waste management in the USA.” Journal of Risk Research. 12:7-8. October 2009. pp. 1009-1024

[2] BENEDICT, R.W., et. al. "Pyroprocessing Progress at Idaho National Laboratory." Global 2007, Boise, Idaho, September 9-13, 2007.

[3] LI, SHELLY X., et. al. "Actinide Recovery Experiments with Bench-scale Liquid Cadmium Cathode in Real Fission Product-laden Molten Salt."Journal of Nuclear Technology.Vol. 165. February 2009.

[4] M. F. Simpson, T. Yoo, R. W. Benedict, S. Phongikaroon, S. Frank, P. Sachdev and K. Hartman, "Strategic minimization of high level waste from pyroprocessing of spent nuclear fuel," Idaho National Laboratory, Idaho Falls, ID, Tech. Rep. INL/CON-07-12123, 2007.

[5] J. P. Ackerman, T. R. Johnson, L. S. H. Chow, E. L. Carls, W. H. Hannum and J. J. Laidler, "Treatment of wastes in the IFR fuel cycle," *Prog. Nuclear Energy,* vol. 31, pp. 141-154, 1997.

[6] G. Janz, "Physical properties data compilations relevant to energy storage II. molten salts: Data on single and multi-component salt systems," Tech. Rep. NSRDS-NBS61-II, .

[7] C. Bale, Facility for the Analysis of Chemical Thermodynamics. 2012 (2012).

[8] P.A. Bingham, R.J. Hand, M.C. Stennett, N.C. Hyatt, M.T. Harrison, The Use of Surrogates in Waste Immobilization Studies: A Case Study of Plutonium. 1107 (2008).

[9] H.C. Aspinall, Chemistry of the f-Block Elements, CRC, 2001.

[10] L.R. Morss, N.M. Edelstein, J. Fuger, The chemistry of the actinide and transactinide elements, The Chemistry of the Actinide and Transactinide Elements:, ISBN 978-94-007-0210-3.Springer Science Business Media BV, 2011. 1 (2011).

[11] P. Masset, R.J.M. Konings, R. Malmbeck, J. Serp, J.P. Glatz, Thermochemical properties of lanthanides (Ln= La, Nd) and actinides (An= U, Np, Pu, Am) in the molten LiCl–KCl eutectic, J. Nucl. Mater. 344 (2005) 173-179.

[12] H. Okamoto and ASM International, Alloy Phase Diagram Section, Materials Park, Ohio, U.S.A., "La-Pt (Lanthanum-Platinum)," *Binary Alloy Phase Diagrams, 2nd Ed. ,Ed. T. B. Massalski,* 1990.

[13] H. Okamoto. (2001, La-W (lanthanum-tungsten). *J. Phase Equilib.* Available: http://www1.asminternational.org/asmenterprise/APD/ViewAPD.aspx?id=1600295.

[14] C.H. Schramm, U-W Phase Diagram. 2012 (2012).

[15] O. Shirai, T. Nagai, A. Uehara, H. Yamana, Electrochemical properties of the Ag< sup> </sup>| Ag and other reference electrodes in the LiCl–KCl eutectic melts, J. Alloys Compounds. 456 (2008) 498-502.

[16] TA Instruments, DSC Q2000, Q200, and Q20 Manual (2008).

[17] D. R. Crow, *Principles & Applications of Electrochemistry.* Bishopbriggs, Glasglow, U.K.: Blackie Academic and Professional, 1994.

[18] J. Wang, *Analytical Electrochemistry.* Hoboken, NJ: John Wiley & Sons, Inc., 2006.

[19] D. Ludwig, "Development of an *in situ* high temperature corrosion probe in molten FLiNaK using anodic stripping voltammetry and neutron activation analysis," University of Wisconsin - Madison, Master's Thesis, 2008.

[20] M. Christopher and A. M. Oliveira, *Electrochemistry Principles, Methods, and Applications.* New York, New York: Oxford Science Publications, 1993.

[21] P. Masset, R. J. M. Konings, R. Malmbeck, J. Serp and J. Glatz, "Thermochemical properties of lanthanides (Ln = La, Nd) and actinides (An = U, Np, Pu, Am) in the molten LiCl–KCl eutectic," *J. Nucl. Mater.,* vol. 344, pp. 173-179, 2005.

[22] M. Blander, *Molten Salt Chemistry.* New York, New York: Interscience Publishers, 1964.

[23] I. Bioanalytical Systems. (2009, 2000-2009). Instruction manual for BASi epsilon for electrochemistry: Chronopotentiometry, *1973.*

[24] J. Serp, R. J. M. Konings, R. Malmbeck, J. Rebizant, C. Scheppler and J. P. Glatz, "Electrochemical behaviour of plutonium ion in LiCl–KCl eutectic melts," *J Electroanal Chem,* vol. 561, pp. 143-148, 2004.

[25] M. Blander, *Molten Salt Chemistry.* New York, New York: Interscience Publishers, 1964.

[26] S. P. Fusselman, J. J. Roy, D. L. Grimmett, L. F. Grantham, C. L. Krueger, C. R. Nabelek, T. S. Storvick, T. Inoue, T. Hijikata, K. Kinoshita, Y. Sakamura, K. Uozumi, T. Kawai and N. Takahashi, "Thermodynamic Properties for Rare Earths and Americium in Pyropartitioning Process Solvents," *J. Electrochem. Soc.,* vol. 146, pp. 2573-2580, 1999.

[27] C. Caravaca, A. Laplace, J. Vermeulen and J. Lacquement, "Determination of the E-pO^{2-} stability diagram of plutonium in the molten LiCl–KCl eutectic at 450°C," *J. Nucl. Mater.,* vol. 377, pp. 340-347, 2008.

[28] L. Massot, P. Chamelot and P. Taxil, "Cathodic behaviour of samarium(III) in LiF–CaF_2 media on molybdenum and nickel electrodes," *Electrochim. Acta,* vol. 50, pp. 5510-5517, 2005.

[29] Y. Castrillejo, M. R. Bermejo, E. Barrado, A. M. Martínez and P. Díaz Arocas, "Solubilization of rare earth oxides in the eutectic LiCl–KCl mixture at 450°C and in the equimolar $CaCl_2$–NaCl melt at 550°C," *J Electroanal Chem,* vol. 545, pp. 141-157, 2003.

[30] R.W. Bradshaw, EFFECT OF COMPOSITION ON THE DENSITY OF MULTI-COMPONENT MOLTEN NITRATE SALTS, Sandia National Laboratory Report (2009).

[31] C.M. Kinart, W.J. Kinart, A. Cwiklinska, Density and viscosity at various temperatures for 2-methoxyethanol acetone mixtures, Journal of Chemical & Engineering Data. 47 (2002) 76-78.

[32] P. Bigg, Density of water in SI units over the range 0-40 C, British Journal of Applied Physics. 18 (1967) 521.

[33] N.Q. Hien, A.B. Ponter, W. Peier, Density and viscosity of carbon tetrachloride solutions containing chlorine, J. Chem. Eng. Data. 23 (1978) 54-55.

[34] R.D. Mariani, D.E. Vaden, Modeled salt density for nuclear material estimation in the treatment of spent nuclear fuel, J. Nucl. Mater. 404 (2010) 25-32.

[35] Thermal Analysis Tests. 2012 (2004). http://www.materialssolutions.info/thermal.html

[36] R. Nicula, Introduction to Differential Scanning Calorimetry (2002).

[37] R.L. Danley, P.A. Caulfield, DSC Baseline Improvements Obtained by a New Heat Flow Measurement (2001) 667-672.

[38] TA Instruments, DSC Q2000, Q200, and Q20 Manual (2008).

[39] Interpreting DSC curves Part 1: Dynamic measurements (2000).

[40] T. Gutknecht, Thermal Analysis of Surrogate Simulated Molten Salts with Metal Chloride Impurities for Electrorefining Used Nuclear Fuel (2012).

[41] C. Rawlinson, Differential Scaning Calorimetry, "Cooking with Chemicals" (2006).

[42] Y. Castrillejo, M. Bermejo, A. Barrado, R. Pardo, E. Barrado, A. Martínez, Electrochemical behaviour of dysprosium in the eutectic LiCl-KCl at W and Al electrodes, Electrochim. Acta. 50 (2005) 2047-2057.

[43] K.G. Chang, X.P. Lu, F.Y. Du, M.S. Zhao, Determination of the apparent standard potential of the Dy/Dy (III) system in the LiCl-KCl eutectic, Chinese Journal of Chemistry. 12 (1994) 509-515.

[44] B. Prabhakara Reddy, S. Vandarkuzhali, T. Subramanian, P. Venkatesh, Electrochemical studies on the redox mechanism of uranium chloride in molten LiCl-KCl eutectic, Electrochim. Acta. 49 (2004) 2471-2478.

[45] P. Masset, D. Bottomley, R. Konings, R. Malmbeck, A. Rodrigues, J. Serp, J.P. Glatz, Electrochemistry of uranium in molten licl-kcl eutectic, J. Electrochem. Soc. 152 (2005) A1109.

[46] F. Gao, C. Wang, L. Liu, J. Guo, S. Chang, L. Chang, R. Li, Y. Ouyang, Electrode processes of uranium ions and electrodeposition of uranium in molten LiCl-KCl, J. Radioanal. Nucl. 280 (2009) 207-218.

[47] O. Shirai, T. Iwai, Y. Suzuki, Y. Sakamura, H. Tanaka, Electrochemical behavior of actinide ions in LiCl-KCl eutectic melts, J. Alloys Compounds. 271 (1998) 685-688.

[48] K. Serrano, P. Taxil, Electrochemical reduction of trivalent uranium ions in molten chlorides, J. Appl. Electrochem. 29 (1999) 497-503.

[49] T.J. Kim, Y. Jung, J.B. Shim, S.H. Kim, S. Paek, K.R. Kim, D.H. Ahn, H. Lee, Study on physicochemical properties of U 3 in LiCl–KCl eutectic media at 773 K, J. Radioanal. Nucl. 287 (2011) 347-350.

[50] K. Nakamura, M. Kurata, Thermal analysis of pseudo-binary system: LiCl□KCI eutectic and lanthanide trichloride, J. Nucl. Mater. 247 (1997) 309-314.

[51] J. Sangster, A.D. Pelton, Thermodynamic Calculation of Phase Diagrams of the 60 Common-Ion Ternary Systems containing Cations Li, Na, K, Rb, Cs and Anions F, Cl, Br, I, Journal of Phase Equilibria. 12 (1991) 511.

[52] M.F. Simpson, J.D. Law, Nuclear Fuel Reprocessing (2010).

[53] D. Yamada, T. Murai, K. Moritani, T. Sasaki, I. Takagi, H. Moriyama, K. Kinoshita, H. Yamana, Diffusion behavior of actinide and lanthanide elements in molten salt for reductive extraction, J. Alloys Compounds. 444 (2007) 557-560.

[54] K. Marsden, B. Pesic, Evaluation of the Electrochemical Behavior of CeCl3 in Molten LiCl-KCl Eutectic Utilizing Metallic Ce as an Anode, J. Electrochem. Soc. 158 (2011) F111.